2022

Optimization-Based Approaches to Low-Coherence Optical Diffraction Tomography

Seth Smith-Dryden
University of Central Florida

OPTIMIZATION-BASED APPROACHES TO LOW-COHERENCE OPTICAL DIFFRACTION TOMOGRAPHY

by

SETH SMITH-DRYDEN
B.S. The Ohio State University, 2014
M.S. University of Central Florida, 2020

A dissertation submitted in partial fulfillment of the requirements
for the degree of Doctor of Philosophy
in the College of Optics and Photonics
at the University of Central Florida
Orlando, Florida

Summer Term
2022

Major Professor: Bahaa Saleh

ABSTRACT

Quantitative optical phase imaging techniques, such as optical diffraction tomography (ODT), are useful tools for refractive-index profiling. Many of them, however, rely on the weak-scattering assumptions, thus cannot be applied to multiple-scattering objects, or turbid media. In this thesis, I report several approaches for expanding the efficacy of ODT techniques and adapting them to new applications by use of low-coherence broadband illumination.

First, I developed a method for ODT reconstruction using regularized convex optimization with a new phase-based fidelity criterion. The new criterion is necessary because objects with very different refractive-index distributions may produce similar diffracted fields (magnitude and principal-phase) on the detection planes. This surjective, but non-injective relation, attributed to the cyclical nature of the phase, makes optimization algorithms using a field-based cost function prone to local minima, particularly for objects introducing large optical pathlength difference. I developed a phase-based optimization algorithm that avoids this and successfully tested it using simulations on phantoms and experimental data measured from samples of optical fibers.

I have developed a method that applies total-variation regularization at each iteration of an iterative framework for ODT, which was developed with co-workers. I performed numerical and experimental tests using various highly scattering objects and demonstrated significant improvement in reconstruction SNR.

I have also designed and constructed a new experimental setup for ODT measurement and expanded the new ODT algorithms from 2D to 3D. These algorithms have been numerically and experimentally validated using simulated data and data collected from the new experimental setup.

Additionally, I have investigated the use of temporally incoherent illumination in ODT and showed that it enables time-gating of artifacts caused by multiple-scattering. I have further demonstrated that ODT combined with Fourier-transform spectroscopy can be used for spectral tomographic imaging of the wavelength-dependent complex-valued refractive index volumetric distributions.

To my loving family.

ACKNOWLEDGMENTS

I would like to express my deepest gratitude to my advisor and chair, Dr. Bahaa Saleh, and to my co-advisor, Dr. Guifang Li for their continued support and guidance through my journey at CREOL. Their willingness to help and provide insight has been instrumental to my understanding of optics and allowed me to grow as an expert in my field, and as a person. I would also like to thank them, Dr. Kyu Young Han and Dr. George Atia for their gracious willingness to serve as my committee members.

I am also deeply indebted to Dr. Axel Schulzgen, Dr. Han, Stefan Gausmann, Ben Croop, and Jian Zhao for allowing me to use their equipment and providing samples for us to image. I would also like to express my gratitude to many other CREOL students and faculty, whom many I consider friends and mentors, for making my time at CREOL an experience that I will always cherish. A special thanks to Shengli Fan, and Ning Wang for making our office lively and enjoyable for much of my time at CREOL.

I would like to acknowledge the National Science Foundation Grant No. 1509294 for making much of my research possible through funding.

TABLE OF CONTENTS

LIST OF FIGURES ix

CHAPTER 1: INTRODUCTION 1

CHAPTER 2: THEORY OF OPTICAL DIFFRACTION TOMOGRAPHY 3

2.1 Overview 3

2.1 The First-Born Approximation 4

2.2 The First Rytov Approximation 6

2.3 The Fourier Diffraction Theorem 8

2.4 Reconstruction Techniques 10

CHAPTER 3: OPTICAL DIFFRACTION TOMOGRAPHY BY USE OF OPTIMIZATION AND PHASE-BASED FIDELITY CRITERION 13

3.1 Introduction 13

3.2 Optimization with Phase-Based Fidelity Criterion 15

3.3 Simulation and Experimental Results 19

CHAPTER 4: ITERATIVE OPTICAL DIFFRACTION TOMOGRAPHY WITH EMBEDDED REGULARIZATION 33

4.1 Introduction 33

4.2 R-iODT Validation 35

4.3 R-iODT Validation 39

CHAPTER 5: EXPERIMENTAL AND NUMERICAL 3D RECONSTRUCTIONS 46

5.1 ODT Experimental Setup 46

5.2 Numerical Validation of 3D ODT 50

5.3 ISC to ORC conversion 59

5.4 Experimental Results 64

CHAPTER 6: SPATIOTEMPORAL ODT 68

6.1. Mathematical Formulation of ST-ODT 69

6.2. Equivalence to CW ODT 70

6.3. Numerical Validation of ST-ODT 71

6.4. Proposed Method: Time-Resolved Phase Unwrapping in Optical Tomography 74

6.5. Proposed Method: Fourier-Transform ODT 76

CHAPTER 6: CONCLUSION 87

LIST OF REFERENCES 90

LIST OF FIGURES

Figure 2.1: Schematic of traditional ODT. Adapted from [16]. 3

Figure 3.1: Two-disk phantom. (a) True object. The dashed box indicates the ROI used to calculate the RMSE in (c). (b) Reconstruction after 300 iterations using the field-based fidelity criterion. (c) RMSE. (d) Cost. (e) Amplitude and (f) phase of the true (blue) and reconstructed (red) fields for $\theta = 0°$. 22

Figure 3.2: Two-disk phantom. (a) True object. The dashed box indicates the ROI used to calculate the RMSE in (c). (b) Reconstruction after 300 iterations using Algorithm 3.1. (c) RMSE. (d) Phase-based cost (blue) and field-based cost (red) as functions of iteration number. (e) Amplitude and (f) phase of true (blue) and reconstructed (red) fields for $\theta = 0°$. 24

Figure 3.3: Shepp-Logan phantom. (a) True object. The dashed box indicates the ROI used to calculate the RMSE in (c). (b) Reconstruction after 300 iterations using the field-based fidelity criterion. (c) RMSE. (d) Cost. (e) Amplitude and (f) phase of true (blue) and reconstructed (red) fields for $\theta = 0°$. 25

Figure 3.4: Shepp-Logan phantom. (a) True object. The dashed box indicates the ROI used to calculate the RMSE in (c). (b) Reconstruction after 300 iterations using Algorithm 3.1. (c) RMSE. (d) Phase-based (blue) and field-based (red) cost as functions of iteration number. (e) Amplitude and (f) phase of true (blue) and reconstructed (red) fields for $\theta = 0°$. 26

Figure 3.5: (a) Reconstructed RI distribution of a Panda fiber after 300 iterations, using the field-based fidelity criterion for experimentally measured diffracted fields. (b) Cost as a function of iteration number. (c) Amplitude and (d) phase of the true (blue) and reconstructed (red) fields for $\theta = 0°$. 28

Figure 3.6: (a) Reconstructed RI distribution of a Panda fiber after 300 iterations, using Algorithm 3.1 for experimentally measured diffracted fields. (b) Phase-based cost (blue) and field-based cost (red) as functions of iteration number. (c) Amplitude and (d) phase of the true (blue) and reconstructed (red) fields for θ = 0°. 29

Figure 3.7: (a) Reconstruction of the RI distribution of a hollow-core fiber filled with DMSO using experimentally measured diffracted fields and optimizing on a field-based fidelity criterion for 300 iterations. (b) Cost as a function of iteration number. (c) Amplitude and (d) phase of the true (blue) and reconstructed (red) fields for θ = 0°. 30

Figure 3.8: (a) Reconstruction of the RI distribution, after 300 iterations of Algorithm 3.1, of a hollow-core fiber filled with DMSO using experimentally measured diffracted fields. (b) Phase-based cost (blue) and field-based cost (red). (c) Amplitude and (d) phase of the true (blue) and reconstructed (red) fields for θ = 0°. 31

Figure 3.9: Convergence study for Shepp-Logan phantom. (a) Phantom RI distribution. (b) RMSD as a function of iteration number, for cost function based on field (red) and phase (blue). 32

Figure 4.1: Schematic of an ODT experiment. Plane wave kb illuminates the sample at θ and travels along ξ direction. The scattered field is measured on the screen at $\xi = d$ along the η direction. The illumination angle is changed and the process is repeated. 36

Figure 4.2: (a) Phantom 1 RI distribution, (b) SNR of the iODT and R-iODT reconstructions over the first 50 iterations. (c and d) Respective iODT and R-iODT reconstructions at the m= 50 iteration. 41

Figure 4.3: (a) Phantom 2 RI distribution, (b) SNR of the iODT and R-iODT reconstructions over the first 50 iterations. (c and d) nRMS errors in amplitude and phase of the sinogram ϵA and $\epsilon \phi$ for iODT and R-iODT, over the first 50 iterations. Blue and red arrows are used to mark the iteration where the stopping criterion is satisfied. (e) iODT reconstruction after stopping criterion satisfied (m=43). (f) R-iODT reconstruction after stopping criterion satisfied (m=49). (g and h) Respective iODT and R-iODT reconstructions after m= 50 iterations. 42

Figure 4.4: (a) Phantom 3 RI distribution, (b) SNR of the iODT and R-iODT reconstructions over the first 50 iterations. (c) and (d) Respective iODT and R-iODT reconstructions after $m = 50$ iterations. 44

Figure 4.5: Phantom 3 reconstructions (a) iODT, (b) R-iODT using TV at each iteration, and (c) iODT with TV regularization applied to final ($m = 50$) reconstruction. 44

Figure 4.6: Reconstructions based on experimental measurements of a multicore optical fiber (a) SEM of fiber, (b) iODT, (c) iODT with TV regularization applied to final iteration ($m = 50$), and (d) R-iODT using TV at each iteration. 45

Figure 5.1: Intrafiber IFA-100 profilometer. 47

Figure 5.2: Field measurement schematic for (a) object rotated configuration and (b) illumination scanning configuration. 48

Figure 5.3: (Left) Experimental setup with beam path illustrated. (Right) Conceptual schematic of setup. 49

Figure 5.4: Angular representation of illumination angles θ and ϕ, with respect to object assumed to be centered at the origin. 51

Figure 5.5: LES frequency coverage for each respective test, assuming DFI mapping in the $k_z = 0$, $k_x = 0$, and $k_y = 0$ planes. A bar is added for scale showing the size of k_b..... 53

Figure 5.6: Row (a): RI distribution of the true object. Rows (b-d): Respective R-iODT reconstructions after 100 iterations using full angular span, $\theta_{max} = 53°$, and $\theta_{max} = 35°$..... 55

Figure 5.7: RMSE of the RI distribution for each R-iODT test..... 56

Figure 5.8: Row (a): RI distribution of the true object. Rows (b-d): Respective phase-based optimization reconstructions after 100 iterations using full angular span, $\theta_{max} = 53°$, and $\theta_{max} = 35°$..... 58

Figure 5.9: RMSE of the RI distribution for each phase-based optimization test. 59

Figure 5.10: Propagation using (a) an ISC framework and (b) ORC framework. A dashed border indicates the approximate necessary boundaries of the simulation volume..... 60

Figure 5.11: Schematic showing propagation steps for converting ISC field measured at $z = d$ plane to ORC field "measured" at $z' = d$ plane. 61

Figure 5.12: (a) and (b): Amplitude and phase, respectively, of a measured ISC field at the plane $z = 0$ μm in global coordinates. (c) and (d): Amplitude and phase, respectively, of the field after being converted to an ORC "measurement" at the plane $z' = 0$ μm in local coordinates. A bar is added in (a) to show scale. 64

Figure 5.13: Experimental reconstruction of polystyrene bead. 65

Figure 5.14: RMSE of the simulated output sinogram, using the best guess of the object's RI and the measured sinogram from the experiment. 67

Figure 6.1: Schematic of OPDs for various forms of scattering. 68

Figure 6.2: Clockwise from top left: Simulation layout, long TG reconstruction (CW), short TG reconstruction, and diffracted pulse envelope, measured vs. time on 1D detector. 72

Figure 6.3: Clockwise from top left: Simulation layout, long TG reconstruction (CW), short TG reconstruction, and diffracted pulse envelope, measured vs. time on 1D detector. 73

Figure 6.4: Clockwise from top left: Simulation layout, long TG reconstruction (CW), short TG reconstruction, and diffracted pulse envelope, measured vs. time on 1D detector. 74

Figure 6.5: Raw interferogram of row of spatial pixels on a CCD detector, at the output of the IFA-100, using an optical fiber sample. Vertical pixels correspond to a row of spatial pixels on the camera, while horizontal pixels correspond to readings at varying differential delays..... 75

Figure 6.6: Estimated RI cross-section through center of fiber, which directly corresponds to the time-of-flight measurements observed in the temporal distribution shown in Figure 5.5. Pixels in the output temporal response, associated with light that has passed through regions of the fiber of negative RI, with respect to the background (in this case, the cladding) arrive before the "leading edge" of the background signal, while areas of positive RI, and positive OPD trail the background signal. 76

Figure 6.7: Diagram of ST-ODT experimental setup. 79

Figure 6.8: Interfiber Analysis IFA-100 fiber index profiler..... 79

Figure 6.9: SEM of PCF cross-section. During the experiment, PCF cores were filled with DMSO liquid..... 80

Figure 6.10: (Left) CW reconstruction of PCF at 633 nm. (right) Representative RI plots showing the spectral behavior of three ROI regions: fiber cores (filled with DMSO), glass fiber cladding, and background medium (RI matching oil). 81

Figure 6.11: SEM image of HCF cross-section. 81

Figure 6.12: Measured absorption spectrum of DMSO/dye solution at 200 μM concentration, as well as for a pure DMSO (no dye present). 82

Figure 6.13: (Top and bottom left) Spatial reconstructions of n and κ, respectively, at 615 nm. (Top and bottom right) Respective plots of the core region for n and κ, for 200 and 700 μM concentrations of dye, as well as for pure DMSO. 83

Figure 6.14: Michelson interferometer for FTS measurements preceding ODT setup in Figure 5.3. 84

Figure 6.15: Holographic measurements and respective spectra using different illumination sources..... 86

CHAPTER 1: INTRODUCTION

Optical imaging is a method of using non-ionizing illumination for studying objects, using absorption or refractive-index (RI) as a contrast agent. In biological applications, optical imaging is both safe (non-ionizing), and highly-effective for imaging soft-tissue, when compared to x-ray imaging [1]. The choice of optical wavelengths is also highly-desirable for characterizing optical properties of ultraviolet (UV) sensitive materials. Key challenges in optical imaging include diffraction/scattering effects, since inhomogeneities in samples can be on a similar scale to the illumination wavelength.

In the case of transparent objects (e.g., biological samples, or optical fibers) absorption-based methods are either difficult, or may require the use of contrast agents to observe the sample clearly [2, 3, 4]. In biological optical imaging applications, contrast agents or fluorescent tags are frequently used to provide high-resolution detail about cellular processes [5, 6]. Unfortunately, these same labelling tools may affect cellular behavior or even be phototoxic to the cells being imaged. For such a class of samples, imaging the refractive-index, or the phase introduced by the objects is especially useful, since the sample's RI can behave as its own contrast agent [7].

Optical phase imaging [8, 9, 10, 11] is particularly useful in tomographic reconstruction. For biological samples, optical tomographic methods offer inexpensive, non-invasive ways to study cells, or tissue in-vivo, up to sub-wavelength resolutions. Popular methods of optical phase tomography include tomographic phase microscopy (TPM) [12, 13, 14], which is a direct analogue to computed tomography (CT) [15], in addition to methods such as optical coherence tomography and diffuse optical tomography [16, 17, 18], which allow 3D imaging of phase objects in turbid

media. Optical diffraction tomography (ODT) [19], a mature technique of growing interest, accounts for the wave nature of light, unlike TPM, when reconstructing objects.

Under weak-scattering conditions, optical diffraction tomography provides quantitative 3D refractive-index (and absorption) imaging of samples, at sub-wavelength resolution by linearly relating the scattered optical field to the permittivity distribution of a sample. Since its inception, ODT has been applied in RI profiling of live cells [20, 21] and other phase objects (e.g., optical fibers) [22]. Because ODT inversions typically employ linearizing assumptions, these inversions are hindered primarily by the presence of multiple scattering, which quickly breaks down the linear relationship between the sample and the scattered field. To address these challenges, new approaches have been proposed and developed to extend the efficacy of ODT inversions to highly scattering samples, or turbid media. This thesis begins with an overview of the theory of ODT and describes new approaches that extend the utility of ODT and address its various challenges.

CHAPTER 2: THEORY OF OPTICAL DIFFRACTION TOMOGRAPHY

2.1 Overview

For optical imaging, many classes of phase objects contain inhomogeneities of a similar size to the illuminating wavelength, causing the illuminating light to diffract, instead of following linear trajectories through a sample (e.g., for x-rays in CT). For tomographic methods to accurately reconstruct objects where the effects of diffraction are non-trivial, the inverse scattering problem must be solved.

For traditional ODT, schematically shown in Figure 2.1, an object to be imaged is illuminated by an impinging plane-wave, and the resulting scattered field is measured on the plane of a detector. In the case of weakly-scattering objects, the scattered field is linearly related to a slice of the Fourier transform of the object, through what is known as the Fourier Slice Theorem [16], a relationship that will be derived in this section. By illuminating the object for all angles, and collecting the respective scattered fields, information of the object's Fourier transform, or Limiting Ewald's Sphere, can be filled in, allowing the object to be reconstructed.

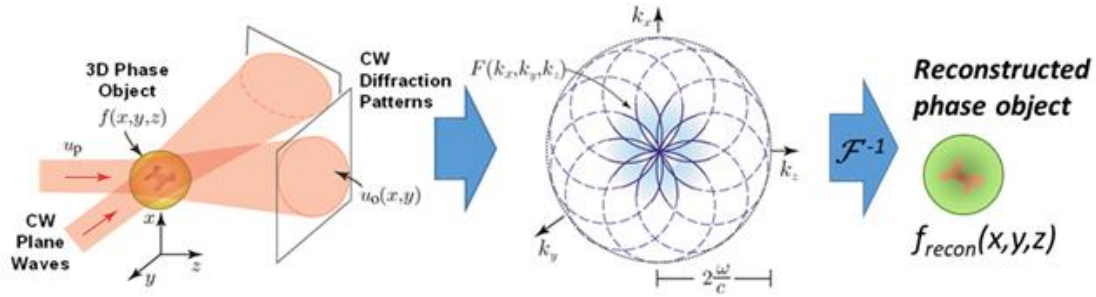

Figure 2.1: Schematic of traditional ODT. Adapted from [16].

To demonstrate this relationship, we take an object, described by f(r), that is contained inside a linear, isotropic, and homogeneous medium of background RI n_b. For an objected illuminated by some field U_o, the throughout the object volume satisfies the inhomogeneous wave equation:

$$(\nabla^2 + k_b^2)U(\vec{r}) = -f(\vec{r})U(\vec{r}), \tag{2.1}$$

where $k_b \equiv \omega \cdot n_b/c$, and 'object function' f(r) relates to the relative permittivity (or RI) by:

$$f(\vec{r}) \equiv \left(\frac{\omega}{c}\right)^2 (n(\vec{r})^2 - n_b^2). \tag{2.2}$$

The homogeneous solution to Equation (2.1), known as the Helmholtz Equation, describes the non-scattered background illumination, U_o (e.g., plane-wave), described by:

$$(\nabla^2 + k_b^2)U_o(\vec{r}) = 0. \tag{2.3}$$

To reconstruct the object function, Equation (2.1) is typically linearly inverted, through either the 1st Born or Rytov approximation [19], which both assume weak scattering.

2.1 The First-Born Approximation

Developed by Born in 1926 as a means to invert the Lippmann-Schwinger equation [23], the 1st Born Approximation, as performed in Born and Wolf [19], first separates the 'total field' U into the illuminating 'background field,' U_o, and a respective 'scattered field,' U_s, as follows:

$$U(\vec{r}) \equiv U_o(\vec{r}) + U_s(\vec{r}). \tag{2.4}$$

Substituting Equation (2.4) into the left-hand side of Equation (2.1):

$$(\nabla^2 + k_b^2)U_o(\vec{r}) + (\nabla^2 + k_b^2)U_s(\vec{r}) = -f(\vec{r})U(\vec{r}), \tag{2.5}$$

which simplifies to:

$$(\nabla^2 + k_b^2)U_s(\vec{r}) = -f(\vec{r})U(\vec{r}). \tag{2.6}$$

We next note the Green's function, which is a solution of Equation (2.1) for which f(r) is a delta function:

$$(\nabla^2 + k_b^2)G(\vec{r}) = -\delta(\vec{r}). \tag{2.7}$$

Decomposing the right-hand side of Equation (2.6) into delta functions, we see:

$$(\nabla^2 + k_b^2)U_s(\vec{r}) = -\int d\overrightarrow{r'}\delta(\vec{r} - \overrightarrow{r'})f(\overrightarrow{r'})U(\overrightarrow{r'}). \tag{2.8}$$

Substituting Equation (2.7):

$$(\nabla^2 + k_b^2)U_s(\vec{r}) = (\nabla^2 + k_b^2)\int d\overrightarrow{r'}G(\vec{r} - \overrightarrow{r'})f(\overrightarrow{r'})U(\overrightarrow{r'}), \tag{2.9}$$

and so:

$$U_s(\vec{r}) = \int d\overrightarrow{r'}G(\vec{r} - \overrightarrow{r'})f(\overrightarrow{r'})U(\overrightarrow{r'}). \tag{2.10}$$

Assuming U_s to be a small perturbation compared to U_o ($U_s \ll U_o$), the 1st Born approximation linearly relates the scattered field to the object function by:

$$U_s(\vec{r}) \approx U_B(\vec{r}) \equiv \int d\overrightarrow{r'}G(\vec{r} - \overrightarrow{r'})f(\overrightarrow{r'})U_o(\overrightarrow{r'}). \tag{2.11}$$

The validity of the 1st Born approximation is typically interpreted to be that the accumulated phase of the scattered field must be much smaller than 2π. In other words, for a phase object of diameter D, and RI difference Δn, $|k_o \Delta n D| \ll 2\pi$, or $|D\Delta n| \ll \lambda$ [24]. For this reason, the Born approximation is known to fail in the case of objects of large size, or high index contrast.

2.2 The First Rytov Approximation

An alternative approach to obtain U_B from Equation (2.11), known as the 1st Rytov approximation [25], is done by expressing the total field's complex phase a perturbation. The total and background fields are now instead defined as:

$$U(\vec{r}) \equiv e^{\phi_o(\vec{r})+\phi_s(\vec{r})}, \qquad U_o(\vec{r}) \equiv e^{\phi_o(\vec{r})}, \tag{2.12}$$

where ϕ_o and ϕ_s are respectively known as the 'background' and 'scattered' phases. Substituting $U_o(r)$ from Equation (2.12) into Equation (2.3):

$$(\nabla^2 + k_b^2)e^{\phi_o(\vec{r})} = \left[\nabla^2\phi_o(\vec{r}) + \left(\nabla\phi_o(\vec{r})\right)^2 + k_b^2\right]U_o(\vec{r}) = 0. \tag{2.13}$$

The background phase satisfies the Riccati equation:

$$\nabla^2\phi_o(\vec{r}) + \left(\nabla\phi_o(\vec{r})\right)^2 + k_b^2 = 0. \tag{2.14}$$

Likewise, the total field, from Equation (2.12) can be substituted into Equation (2.1) to obtain:

$$\nabla^2 e^{\phi_o+\phi_s} + k_b^2 e^{\phi_o+\phi_s} = \nabla\cdot\left[\left(\nabla\phi_o(\vec{r})\right)U(\vec{r}) + \left(\nabla\phi_s(\vec{r})\right)U(\vec{r})\right] + k_b^2 U(\vec{r}), \tag{2.15}$$

$$(\nabla^2\phi_o + (\nabla\phi_o)^2 + k_b^2)U + (\nabla^2\phi_s + (\nabla\phi_s)^2 + 2\nabla\phi_o\cdot\nabla\phi_s)U = -fU. \tag{2.16}$$

Substituting Equation (2.14) into Equation (2.16), and dividing both sides by U, we obtain the Riccati equation governing ϕ_s:

$$\nabla^2\phi_s + (\nabla\phi_s)^2 + 2\nabla\phi_o\cdot\nabla\phi_s = -f. \tag{2.17}$$

To relate the scattered phase, ϕ_s, to U_B from Equation (2.11), we study the following equations:

$$(\nabla^2 + k_b^2)U_o\phi_s = \nabla\cdot[(\nabla\phi_o)U_o\phi_s + (\nabla\phi_s)U_o] + k_b^2(U_o\phi_s) \tag{2.18}$$

$$= \left(\boldsymbol{\nabla^2\phi_o + (\nabla\phi_o)^2 + k_b^2}\right)U_o\phi_s + (\nabla^2\phi_s + 2\nabla\phi_o\cdot\nabla\phi_s)U_o \tag{2.19}$$

Substituting Equation (2.14) into bolded portion:

$$(\nabla^2 + k_b^2)U_o\phi_s = (\nabla^2\phi_s + 2\nabla\phi_o \cdot \nabla\phi_s)U_o, \tag{2.20}$$

$$= (\nabla^2\phi_s + 2\nabla\phi_o \cdot \nabla\phi_s + (\nabla\phi_s)^2 - (\nabla\phi_s)^2)U_o. \tag{2.21}$$

Substituting in Equation (2.17):

$$(\nabla^2 + k_b^2)U_o\phi_s = -(f + (\nabla\phi_s)^2)U_o. \tag{2.22}$$

Green's decomposition, as followed by Equations (2.6) through (2.10), gives:

$$U_o(\vec{r})\phi_s(\vec{r}) = \int d^3\overrightarrow{r'}G(\vec{r} - \overrightarrow{r'})\left[f(\overrightarrow{r'}) + \left(\nabla\phi_s(\overrightarrow{r'})\right)^2\right]U_o(\overrightarrow{r'}), \tag{2.23}$$

which relates to Equation (2.11) by:

$$U_o(\vec{r})\phi_s(\vec{r}) = U_B(\vec{r}) + \int d^3\overrightarrow{r'}G(\vec{r} - \overrightarrow{r'})\left(\nabla\phi_s(\overrightarrow{r'})\right)^2 U_o(\overrightarrow{r'}). \tag{2.24}$$

The 1st Rytov Approximation assumes $(\nabla\varphi_s)^2 \ll f$, such that:

$$\phi_s(\vec{r}) \equiv \log\left(\frac{U(\vec{r})}{U_o(\vec{r})}\right) \approx \phi_R(\vec{r}) \equiv \frac{U_B(\vec{r})}{U_o(\vec{r})}. \tag{2.25}$$

The log function in Equation (2.25) leaves the imaginary part of ϕ_s wrapped between -π and π, and so an unwrapping algorithm must be used to correctly obtain ϕ_s. The validity condition of the Rytov approximation requires that the scattered phase vary slowly on the scale of a wavelength, or more exactly $(\nabla\varphi_s)^2 \ll f$. While this is true, the requirement that the Rytov phase be unwrapped correctly is often underappreciated – especially in the case of higher contrast samples. The presence of phase vortices makes unwrapping extremely difficult and causes the phase gradient to be locally large near the vortex (even with correct phase unwrapping). Although the Rytov approximation is often considered more versatile than the Born approximation [24], the latter does not require phase-unwrapping.

2.3 The Fourier Diffraction Theorem

To show how the quantity U_B relates to a curved slice of the object function's Fourier transform (i.e., the Fourier Slice Theorem), we first derive an expression for the Green's function in the frequency domain [26]. This is done by Fourier transforming both sides of Equation (2.7):

$$\int d^3\overrightarrow{r'} e^{j2\pi\vec{v}\cdot\overrightarrow{r'}}(\nabla^2 + k_b^2)G(\overrightarrow{r'}) = -1. \tag{2.26}$$

Expressing $G(r)$ as the inverse Fourier transform of the transfer function H:

$$\begin{aligned}&\int d^3\overrightarrow{r'} e^{j2\pi\vec{v}\cdot\overrightarrow{r'}}(\nabla^2 + k_b^2)\int d^3\vec{k}\, H(\vec{v})\, e^{-j2\pi\vec{v}\cdot\overrightarrow{r'}}\\ &= \int d^3\overrightarrow{r'} e^{j2\pi\vec{v}\cdot\overrightarrow{r'}}\int d^3\vec{k} e^{-j2\pi\vec{v}\cdot\overrightarrow{r'}}(k_b^2 - |2\pi\vec{v}|^2)H(\vec{v}) = -1,\end{aligned} \tag{2.27}$$

and so the Fourier transform of the Green's function is

$$H(\vec{k}) = \frac{-1}{k_b^2 - |\vec{k}|^2}, \tag{2.28}$$

where $\vec{k} \equiv 2\pi\vec{v}$. The form of Equation (2.28) is the same for 2D and 3D Green's functions. The Fourier slice theorem can be readily shown by expressing the 3D convolution integral, defining U_B, in frequency domain:

$$\widehat{U_B}(\vec{k}) \equiv H(\vec{k}) \cdot S(\vec{k}), \tag{2.29}$$

where S(k) is defined as the Fourier transform of $f(r)\cdot U_o(r)$. In the case of U_o being a plane-wave along the vector $\mathbf{k_o}$, S(K) is simply the Fourier transform of the object function, shifted by $\mathbf{k_o}$. In this case, U_B is given as:

$$\widehat{U_B}(\vec{k}) \equiv H(\vec{k}) \cdot F(\vec{k} - \overrightarrow{k_b}). \tag{2.30}$$

Examining Equation (2.28), $H(k)$ becomes infinitely large at $k_b^2 = |k|^2$, and so the Fourier transform of U_B is dominated by the portion of $H(k)\cdot F(k\text{-}k_b)$ which falls on this slice. An alternative way to exactly show this relationship is by inverse Fourier transforming H(k) [26]:

$$g(\vec{r}) = \iint dv_x dv_y e^{-j2\pi(v_x x + v_y y)} \int dv_z e^{-j2\pi v_z \cdot z} H(\vec{v}) \,. \tag{2.31}$$

The inner integral may be evaluated using in the following form:

$$\int_{-\infty}^{+\infty} dv_z e^{-j2\pi v_z \cdot z} H(\vec{v}) = \frac{2}{(2\pi)^2} \int_0^{+\infty} dv_z \frac{\cos(2\pi v_z z)}{(ja)^2 + v_z^2}, \tag{2.32}$$

where $a \equiv \sqrt{\left(\frac{n_b}{\lambda}\right)^2 - v_x^2 - v_y^2}$.

I now use the relation from Erdelyi [27]:

$$\int_0^{+\infty} dx \, \frac{\cos(xy)}{a^2 + x^2} = \frac{\pi}{2a} e^{-ja|y|} \tag{2.33}$$

to show that:

$$\frac{1}{(2\pi)^2} \int_{-\infty}^{+\infty} dv_z e^{-j2\pi v_z \cdot z} \frac{1}{(ja)^2 + v_z^2} = \frac{2}{(2\pi)^2} \int_0^{+\infty} dv_z \frac{\cos(2\pi v_z z)}{(ja)^2 + v_z^2} = \frac{1}{j4\pi a} e^{-j2\pi a|z|}, \tag{2.34}$$

and so Equation (2.31) may now be re-expressed as:

$$G\left(\vec{r} - \overrightarrow{r'}\right) = \iint dv_x dv_y \frac{1}{j4\pi a} e^{-j2\pi(v_x (x-x') + v_y (y-y') + a|z-z'|)} \,. \tag{2.35}$$

Assuming the measured field is the transmitted field, the |z - z'| in Equation (2.35) is z - z' (the reflected field requires z'- z, respectively). $U_B(r)$ is now written, using Equations (2.35) and (2.11), as:

$$U_B(\vec{r}) = \int d\overrightarrow{r'} \iint dv_x dv_y \frac{1}{j4\pi a} e^{-j2\pi\left(v_x (x-x') + v_y (y-y') + a(z-z')\right)} f\left(\overrightarrow{r'}\right) U_o\left(\overrightarrow{r'}\right), \tag{2.36}$$

Assuming U_o is a plane-wave directed along z:

$$U_B(\vec{r}) = \iint d\nu_x d\nu_y \frac{1}{j4\pi a} e^{-j2\pi(\nu_x x + \nu_y y + a\cdot z)} \hat{F}\left(\nu_x, \nu_y, a - \frac{n_b}{\lambda}\right). \quad (2.36)$$

As shown above, the 2D Fourier transform of U_B, at a given propagation distance *z*, is directly proportional to a slice of the object function's Fourier transform, along the surface of a sphere of radius n_b/λ. The form Equation (2.36) is a 1D inverse Fourier transform along the transverse frequency coordinate, in the case of 2D objects.

2.4 Reconstruction Techniques

Two well-known, traditional reconstruction methods that employ the 1st Born or Rytov approximations are filtered back-propagation (FBPP) [28] and direct Fourier interpolation (DFI). Beginning with the simplest method, DFI works by calculating U_B, for a given distance 'z,' and then using Equation (2.36) to solve for a slice of the object function's Fourier transform. After information of the slice is known, the values are interpolated to fill the 3D Fourier transform of the object, known as the Limiting Ewald Sphere (LES). After calculating slices for all illumination angles, the LES becomes filled in, and a 3D inverse Fourier transform yields the reconstructed object function. The reconstruction quality depends then on (1) the total number of illumination angles (i.e., how much of the LES volume is filled in) [16], (2) the accuracy of calculating U_B for each illumination angle (the validity of the Born and Rytov assumptions), and (3) the quality of the interpolation method.

The second, more popular method is FBPP, which is directly analogous to filtered back-projection (FBPJ), used in CT reconstructions. The FBPP algorithm works by propagating the complex field (and by extension its phase) through the object volume, and then applying a spectral ramp filter on the back-propagated image. In 2D, FBPP is performed, using the following equation:

$$f(\vec{r}) = \frac{1}{2}\int_0^{2\pi} d\theta\ \Pi_\theta(x', z')\,, \tag{2.37}$$

where *x', z'* are local (rotated) coordinates of *x*, *z*:

$$\begin{bmatrix} x \\ z \end{bmatrix} = \begin{bmatrix} \cos(\theta) & -\sin(\theta) \\ \sin(\theta) & \cos(\theta) \end{bmatrix} \begin{bmatrix} x' \\ z' \end{bmatrix}, \tag{2.38}$$

and $\Pi(x', z')$ relates to U_B, from Equation (2.36) by:

$$\Pi_\theta(x', z') \equiv \int_{-\nu_b}^{\nu_b} d\nu' |\nu_x'| \frac{\widehat{U_B}(\nu_x'; z' = l)}{U_o(z = l)} e^{-j2\pi\sqrt{\nu_b^2 - \nu_x'^2}(z'-l)} e^{-j2\pi\nu_x' x'}\,. \tag{2.39}$$

To remove the quadratic phase associated with the product $a \cdot z$, in Equation (2.36), it is convenient to re-focus the field on the detector to the center of the object, where $z = 0$, allowing the Fourier slice to be determined without problems of aliasing, for large distances as well as aid in noise suppression [29]. Additionally, the FBP algorithm was improved further by Juliana et al. (2014) [30] by propagating the measured field through the volume of the object, before calculating the Rytov phase. Since the Rytov phase propagates according to the Riccati equation in (2.17) and not as a field, a more accurate determination of U_B is given, for each axial position in the back-propagated image, used in Equation (2.37). By doing so, FBPP's depth of focus is extended (EDOF-FBPP) [30].

More recently, iterative approaches for ODT have become popular, such as iODT [22], which I co-developed, and inversions which attempt to use regularized optimization frameworks, such as the fast iterative shrinkage thresholding algorithm (FISTA), and conjugate gradient descent (CGD) [31, 32], to minimize a cost function that seeks to satisfy a data fidelity criterion in which the measured fields are compared to counterparts that are simulated using an estimate of the sample's RI. In the following section, a new method is proposed to extend the advantageous

capability of Rytov reconstructions, to use phase unwrapping to correctly link the unwrapped phase (e.g., optical phase delay) of the output fields, to the objects RI distribution. We also show the potential weaknesses of minimizing a field-based fidelity criterion, if the sample's true RI contains a phase delay that is considerably different to the one from an estimated distribution.

CHAPTER 3: OPTICAL DIFFRACTION TOMOGRAPHY BY USE OF OPTIMIZATION AND PHASE-BASED FIDELITY CRITERION

In this chapter, I introduce a new method for reconstructing phase objects in optical diffraction tomography (ODT) based on regularized convex optimization with a new phase-based fidelity criterion. This work was published in an article in the IEEE Journal of Selected Topics in Quantum Electronics [33] of which I was principal author, and this chapter contains material therefrom.

The new criterion is necessary because objects with very different refractive-index distributions may produce similar diffracted fields (magnitude and principal-phase) on the detection planes. This surjective, but non-injective relation, attributed to the cyclical nature of the phase, makes optimization algorithms using a field-based cost function prone to local minima, particularly for objects introducing large optical pathlength difference. A phase-based optimization algorithm that avoids this problem has been developed and tested successfully using simulation results on phantoms as well as experimental data measured from optical fibers.

3.1 Introduction

Optical diffraction tomography (ODT) is a mature phase imaging technique for quantitative measurement of the 3D refractive index (RI) distribution in order to study biological processes or characterize optical materials [20, 34, 35, 36]. ODT measurements are performed by illuminating the phase object with monochromatic waves over multiple directions, holographically recording the resultant diffracted fields, and subsequently solving the inverse scattering problem to reconstruct the object. In the case of weak scattering, conventional ODT inversions linearize the

relationship between the diffracted output signal and the object's distribution by using either the first Born or the Rytov approximation [19, 37]. Between the two, the Rytov approximation is considered more versatile [24] since the Born approximation restricts the phase introduced by the sample to be less than π, whereas the Rytov approximation may use phase unwrapping to reconstruct objects introducing larger phase delays. Linear ODT reconstructions are often performed by either mapping the measured signal onto an interpolated slice of the object's Fourier-transform, or by using the Filtered Backpropagation (FBPP) framework [28]. Recently, the FBPP framework was expanded to improve the reconstruction accuracy of off-axis features, using the Rytov approximation [30].

Although linear reconstruction algorithms are computationally fast, the relationship between the index distribution and the diffracted field is generally nonlinear, due to the presence of multiple scattering. In order to model the effects of multiple scattering to obtain accurate reconstructions of highly-scattering objects, iterative methods have been devised [22, 38, 39, 40]. Recently, new methods based on regularized optimization have also been developed for obtaining highly-accurate ODT reconstructions, even in the presence of multiple scattering [31, 32, 41, 42, 43]. Typically, optimization methods seek to satisfy a fidelity criterion by minimizing a cost function for which the measured complex-valued field (or intensity) is compared with a simulated version thereof, calculated using an estimate of the object. Since these algorithms employ accurate (nonlinear) simulation solvers, and may also include sparsity-promoting regularization, they typically outperform conventional ODT reconstructions – especially in the case of missing, or incomplete datasets (e.g., in the missing cone problem) [44].

In the case of objects with large optical pathlength difference (OPD), however, the standard field-based fidelity criterion may not be adequate since satisfying it only provides a good match between the measured and simulated fields but does not guarantee that the true (unwrapped) phases are themselves matched. Furthermore, as will be shown, using the standard field-based fidelity criterion tends to trap the optimization process in local minima, if the OPD of the initial estimate of the sample is not sufficiently close to the true distribution. Current optimization techniques for ODT have not included measures to address the use of phase unwrapping in the optimization paradigm, for large OPD samples. In this paper, we aim to fill this gap by proposing a new fidelity criterion aiming at matching the optical phase delay, obtained using phase unwrapping, to allow convex optimization methods to avoid the non-bijective (i.e., one-to-one) correspondence between the output diffracted fields and the RI, thereby allowing accurate reconstructions without the use of warm initialization, or more aggressively tuned regularization.

3.2 Optimization with Phase-Based Fidelity Criterion

In this section, we introduce a new fidelity criterion that matches the complex-valued phases of the measured and simulated fields and compare it to the standard fidelity criterion based on fields. Image formation in ODT is modeled by the vector equation

$$\boldsymbol{y}^{(\ell)} = \mathbf{S}^{(\ell)}(\boldsymbol{n}), \tag{3.1}$$

where $\boldsymbol{n} \in \mathbb{R}^{\mathrm{M}}$ is a vector representing the RI distribution $n(x, y, z)$, discretized into M pixels (or voxels), $\boldsymbol{y}^{(\ell)} \in \mathbb{C}^N$ are N-dimensional complex vectors representing the measured diffracted fields that are holographically recorded at the plane of an N-pixel detector for the views $\ell = 1, 2, \cdots L$. The mapping $\mathbf{S}$ represents a discretized version of the scattering model (e.g., the

Lippmann-Schwinger equation), which is generally nonlinear. To solve the inverse scattering problem, we seek an estimate of the RI distribution $\widehat{\boldsymbol{n}}$ that minimizes a cost function:

$$\widehat{\boldsymbol{n}} \in \arg\min_{\widehat{\boldsymbol{n}} \in \mathbb{R}^{\mathrm{M}}} \{\mathcal{D}(\widehat{\boldsymbol{n}}, \boldsymbol{y}) + \tau \mathcal{R}(\widehat{\boldsymbol{n}})\}, \tag{3.2}$$

where $\mathcal{D}(\widehat{\boldsymbol{n}}, \boldsymbol{y})$ is a measure of fidelity with $\mathbf{y} = \{\boldsymbol{y}^{(\boldsymbol{\ell})}\}$, $\mathcal{R}(\widehat{\boldsymbol{n}})$ is a regularization parameter, and τ is a weight that controls the strength of regularization. The standard fidelity criterion for the minimization problem is

$$\mathcal{D}(\widehat{\boldsymbol{n}}) \equiv \frac{1}{2L} \sum_{\ell=1}^{L} \left\| \widehat{\mathbf{S}}^{\ell}(\widehat{\boldsymbol{n}}) - \boldsymbol{y}^{\ell} \right\|_2^2, \tag{3.3}$$

where, for a given angle ℓ, $\widehat{\mathbf{S}}^{\ell}(\widehat{\boldsymbol{n}})$ maps the estimated RI, $\widehat{\boldsymbol{n}}$, to the simulated field on the detector.

For certain samples – especially those that produce large OPDs – a potential disadvantage of comparing complex-valued fields in the data fidelity is that certain $\widehat{\boldsymbol{n}}$ may map to fields, $\widehat{\mathbf{S}}^{\ell}(\widehat{\boldsymbol{n}})$ that are highly similar to the measured ones, $\boldsymbol{y}^{\ell}$, yet contain the incorrect OPD, due to the cyclical nature of the phase of the complex fields. For data fidelity criteria that compare intensities, the ambiguity is even greater, since all phase information is removed in the fidelity criterion. As we will demonstrate later, this ambiguity may lead to local minima, which prevent convergence to the correct RI distribution, even for weakly-scattering samples. To remove this ambiguity, we seek a fidelity criterion that, for every angle, uniquely compares the OPD from the estimated RI, $\widehat{\boldsymbol{n}}$, to one from the true distribution, $\boldsymbol{n}$, using the complex-valued phases of the fields, $\widehat{\mathbf{S}}(\widehat{\boldsymbol{n}})$ and $\boldsymbol{y}$, now defined as

$$\widehat{\mathbf{S}}(\widehat{\boldsymbol{n}}) \equiv e^{\widehat{\boldsymbol{\Phi}}_{\mathbf{s}}(\widehat{\boldsymbol{n}})}, \tag{3.4}$$

$$\boldsymbol{y} \equiv \mathrm{e}^{\boldsymbol{\Phi}_{\boldsymbol{y}}}. \tag{3.5}$$

These phases, assumed to be continuous, are obtained by taking a log of the respective fields, and then performing phase-unwrapping on the imaginary part of the phase, otherwise bounded on the interval $[-\pi, \pi)$. We re-define the data fidelity term from Equation (3.3) as:

$$\mathcal{D}(\widehat{\boldsymbol{n}}) \equiv \frac{1}{2L}\sum_{\ell=1}^{L}\left\|\widehat{\boldsymbol{\phi}}_{\mathbf{s}}^{\boldsymbol{\ell}}(\widehat{\boldsymbol{n}}) - \boldsymbol{\phi}_{\boldsymbol{y}}^{\ell}\right\|_2^2. \tag{3.6}$$

To perform the minimization problem in Equation (3.2) with the fidelity measure in Equation (3.6), we use a regularized gradient descent approach. The gradient of $\mathcal{D}(\boldsymbol{n})$ is

$$\begin{aligned}\nabla\mathcal{D}(\boldsymbol{n}) &= \left[\frac{\partial}{\partial \boldsymbol{n_1}}\mathcal{D}(\boldsymbol{n}) \quad \cdots \quad \frac{\partial}{\partial \boldsymbol{n_M}}\mathcal{D}(\boldsymbol{n})\right] \\ &= \frac{1}{L}\sum_{\ell=1}^{L}\mathrm{Re}\left\{\left(\boldsymbol{\phi}_{\mathbf{s}}^{\ell}(\boldsymbol{n}) - \boldsymbol{\phi}_{\boldsymbol{y}}^{\ell}\right)^{\mathrm{H}}\left[\frac{\partial \boldsymbol{\phi}_{\mathbf{s}}(\boldsymbol{n})}{\partial \boldsymbol{n}}\right]\right\}.\end{aligned} \tag{3.7}$$

Assuming the gradient of the simulated complex phase defined by Equation (3.4) can be determined via the chain rule,

$$\left[\frac{\partial \mathbf{S}(\boldsymbol{n})}{\partial \boldsymbol{n}}\right] = \mathrm{diag}\{\mathbf{S}(\boldsymbol{n})\}\left[\frac{\partial \boldsymbol{\phi}_{\mathbf{s}}(\boldsymbol{n})}{\partial \boldsymbol{n}}\right], \tag{3.8}$$

and if the values of $\widehat{\mathbf{S}}(\boldsymbol{n})$ are non-zero (i.e., diagonal term is non-singular), the gradient of $\boldsymbol{\phi}_{\mathbf{s}}(\boldsymbol{n})$ is:

$$\left[\frac{\partial \boldsymbol{\phi}_{\mathbf{s}}(\boldsymbol{n})}{\partial \boldsymbol{n}}\right] = \mathrm{diag}\{1/\mathbf{S}(\boldsymbol{n})\}\left[\frac{\partial \mathbf{S}(\boldsymbol{n})}{\partial \boldsymbol{n}}\right], \tag{3.9}$$

where the division denotes an elementwise (Hadamard) division of $\mathbf{S}(\boldsymbol{n})$. If the gradient of $\boldsymbol{S}(\boldsymbol{n})$ is known, the gradient of its phase can be determined, with minimal computational cost – provided the simulated phase is well-defined (i.e., $|\boldsymbol{S}(\boldsymbol{n})|$ not close to zero). It follows that the new fidelity criterion – and its gradient – can be readily integrated into state-of-the-art optimization frameworks for solving the inverse problem associated with ODT and other similar problems.

In the presence of strong scattering, the magnitude of the output fields may become small, and so the value of the associated phase(s) may become undetermined and introduce numerical instability when calculating the gradient in Equation (3.9). To improve numerical stability, we developed an algorithm (Algorithm 3.1) that first minimizes a cost function whose fidelity criterion compares the complex phase shown in Equation (3.6), while the difference between the imaginary part of the residue term is greater than π (i.e., iterations where phase unwrapping is necessary), and then switches to minimizing a cost function whose fidelity term is given by Equation (3.3). The switching criteria is described in Algorithm 3.1.

To perform the minimization problem described by Equation (3.1), we use the gradient-descent algorithm described in [31], which is similar to the fast-iterative shrinkage/thresholding algorithm (FISTA), and uses the Wide-Angle Beam Propagation Method (WA-BPM) [45] to evaluate $\hat{\mathbf{S}}(\hat{\boldsymbol{n}})$. Rather than using all views, at each iteration, to compute the fidelity term in Equation (3.3) or Equation (3.6), this algorithm randomly selects, with equal probability, a subset of $\tilde{L} \leq L$ angles to approximately compute the fidelity term and its gradient. By doing so, computational efficiency is improved. For regularization, we elect to use the total-variation (TV) regularization algorithm, described in [31].

Algorithm 3.1

Input: input field $\mathbf{y_0}$, measured fields $\{y^{\ell}\}_{\ell\in[1\ldots L]}$, current RI estimate $\widehat{\boldsymbol{n}}_{\boldsymbol{g}}$, UW_{max}

Set: $t \leftarrow 1, \widehat{\boldsymbol{n}}^0 \leftarrow \widehat{\boldsymbol{n}}_{\boldsymbol{g}}$

Repeat:

1. Compute simulated fields $\widehat{\boldsymbol{y}}^{\ell} = \mathbf{S}^{(\boldsymbol{\ell})}(\widehat{\boldsymbol{n}}^{\boldsymbol{t-1}})$ for each view.
2. Compute $\boldsymbol{\phi}_{\boldsymbol{y}}^{\ell}, \widehat{\boldsymbol{\phi}}_{\boldsymbol{s}}^{\ell}$, using phase unwrapping on the imaginary parts.
3. **If** $\left(\pi < \frac{1}{L}\sum_{\ell=1}^{L} \max\left\{\left|Im\left\{\boldsymbol{\phi}_{\boldsymbol{y}}^{\ell} - \widehat{\boldsymbol{\phi}}_{\boldsymbol{s}}^{\ell}\right\}\right|\right\}\right)$ **or** (t $< UW_{max}$)

   Minimize Equation 3.2 for one iteration, using convex optimization framework (e.g., FISTA) with Equation 3.6 as fidelity criterion. Obtain new RI estimate, $\widehat{\boldsymbol{n}}^{t}$.

   Else

   Minimize Equation 3.2 for one iteration, using convex optimization framework (e.g., FISTA) with Equation 3.3 as fidelity criterion. Obtain new RI estimate, $\widehat{\boldsymbol{n}}^{t}$.
4. $\widehat{\boldsymbol{n}}_{\boldsymbol{g}} \leftarrow \widehat{\boldsymbol{n}}^{\boldsymbol{t}}$
5. $t \leftarrow t + 1$

Until stopping criterion

Return RI estimate $\widehat{\boldsymbol{n}}_{\boldsymbol{g}}$.

3.3 Simulation and Experimental Results

In this section, we report reconstruction using both simulation data and experimental measurements to validate the value and limitations of the phase-based fidelity criterion for ODT of phase objects introducing large OPD. During optimization, we follow Algorithm 3.1 over 300 iterations. Typically, optimization using a phase-based fidelity criterion converges to an estimate that is sufficiently close to the true distribution within 10 iterations, so that subsequently optimizing on a field-based cost function will converge to the correct answer. In the case of highly-scattering samples (e.g., the Shepp-Logann sample shown later), phase residues may be present in the sinogram that cannot be exactly subtracted out, using the first condition shown in step 3 of Algorithm 3.1. To ensure that Algorithm 3.1 swaps to the field-based fidelity criterion (which is not affected by the presence of residues), the swap condition also includes a maximum number of iterations, UW_{max}=15, before swapping to a field-based fidelity criterion. In the following results, hyperparameters for τ, and γ (as used in [31]) range from 10^{-4} to 10^{-2}. In order to unwrap the imaginary portion of the complex phases, we elect to use the L2-norm phase-unwrapping method

[46]. The mapping $\hat{\mathbf{S}}(\hat{\boldsymbol{n}})$ models the complex optical fields on the detector, corresponding to plane-wave probes that are diffracted by an object with refractive index $\boldsymbol{n}$, which are then refocused to the center of the scattering volume by means of an imaging system, placed between the sample and the detector. To improve consistency between simulated and experimental measurements, we model this imaging system, which exists in the physical setup for obtaining experimental data, as an ideal system that refocuses fields from the output boundary of the simulation volume to the sample's center, using the angular spectrum method [47]. For simplicity, we assume an ideal lens system with infinite numerical aperture; however, the optical transfer function of a lens system can be accurately modelled, if the lens system(s) used in the experiment is known.

For each sample, we compare the reconstruction qualities using the field-based and phase-based criteria. To allow direct comparisons between the cost functions of each reconstruction, after convergence, we do not modify hyperparameters between reconstructions using a purely field-based cost function, and ones performed using Algorithm 3.1 (e.g., τ, and γ that are used in Algorithms 1,2 of [31]). For reconstruction using the phase-based fidelity, we also plot, for visualization purposes only, the field-based cost function to demonstrate whether the initial guess of the sample (assumed to be the background) is within the locally convex well of the global minimum. If the initial estimate of the sample lies outside of the well, the cost function would need to first rise, reach a local maximum before being able to converge towards the correct solution using convex optimization. For each reconstruction, a "cold initialization" is used, where the sample's distribution is assumed to be an empty, uniform distribution of the background RI, n_b. Although in the case of simple objects, one may obtain a sufficiently accurate initialization using linear reconstruction methods (e.g., filtered back-propagation, or inverse Radon transform) for

minimizing the field-based cost function, these initializations are prone to failure in the presence of multiple scattering. In this case, the initial linear reconstruction may be further away from the global minimum than the cold initialization, and so minimizing a field-based cost on an inaccurate initialization is highly susceptible to converge to an incorrect minimum. For this reason, it may be advantageous to begin with a cold initialization, and then use an iterative method that uses regularization and constraints to obtain a sufficiently accurate estimate before minimizing a field-based cost function. We use Algorithm 3.1 to implement this strategy. For each sample, 36 output diffracted fields are recorded for varying illumination angles that span from 0° to 175°, in 5° increments. We apply no constraints on the maximum or minimum RI during reconstructions.

3.3.1 Numerical Validation

For numerical validations, the "true" scattered fields are calculated using WA-BPM. For each phantom, the background RI is taken to be n_b = 1.518, and the probe wavelength λ_o = 561 nm. The reconstruction area used in numerical validation is 243×243 pixels, each of dimension dx = 0.072 μm (~λ_0/8). Each iteration on average took about 2.7 seconds to complete. To directly measure the accuracy of reconstructions of known simulated objects, the root-mean-square deviation (RMSD) error in the real part of the reconstructed RI distribution is plotted, within a region of interest (ROI) of the samples' features. This is done to prevent the RMSD from being biased by the large number of background pixels which may contain small deviations from n_b.

For the first sample, two disks of radius 4.5 μm, and n= 1.5863 are placed in the background medium, separated by 12 μm. The reconstruction, shown in Figure 3.1, using the field-based

fidelity criterion, shows an incorrect RI distribution; however, the diffracted fields, on the detector, match well in both amplitude and phase.

The possibility of the diffracted field from an incorrect reconstruction to closely match the output field from the true object suggests that because the principal phase is surjective, but not injective, samples that produce OPD distributions that differ by integer multiples of 2π tend to create highly-similar diffracted fields. In such situations, the minimization problem is susceptible to being trapped in "deep" local minima, in which the data-fidelity criterion appears to be satisfied but, the RI distribution is significantly different from that of the true sample. At the local minimum shown in Figure 3.1, the cost function, after 300 iterations, converges to a value of 0.76, while the root-mean-square error, RMSE (or root-mean-square-deviation error, RMSD) of the RI reconstruction rose to 6.06, a level greater than the initial guess of background (no sample).

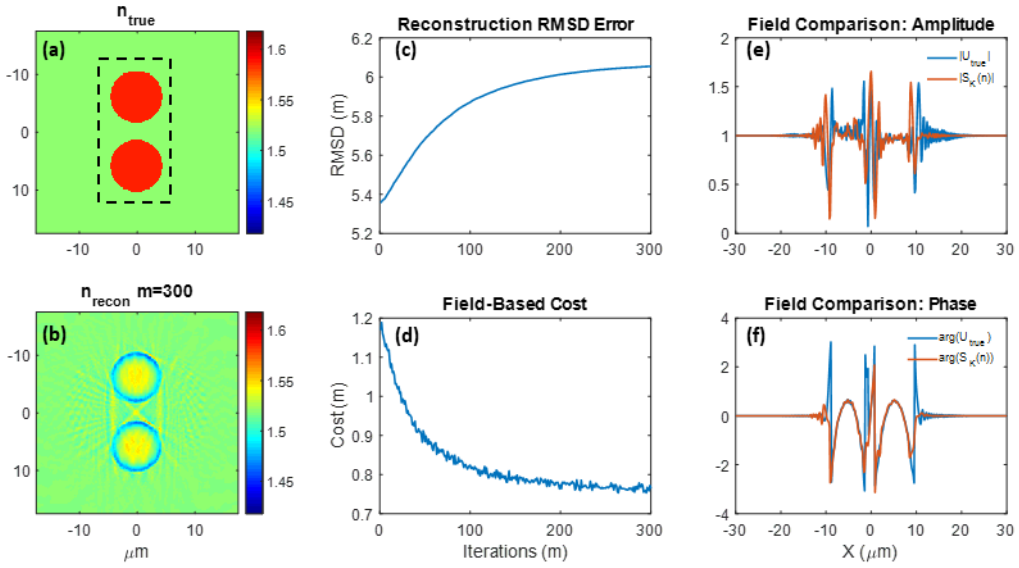

Figure 3.1: Two-disk phantom. (a) True object. The dashed box indicates the ROI used to calculate the RMSE in (c). (b) Reconstruction after 300 iterations using the field-based fidelity criterion. (c) RMSE. (d) Cost. (e) Amplitude and (f) phase of the true (blue) and reconstructed (red) fields for $\theta = 0°$.

Reconstruction results of the same two-disk phantom by use of the phase-based fidelity are depicted in Figure 3.2. Here, optimization does converge to the correct RI distribution. As shown in the first 10 iterations of Figure 3.2 (d), the phase-based cost function decreases rapidly between iterations, while the field-based cost function shows a local maximum at iteration 3. After iteration 10, the fidelity criterion is changed to one based on field hence the red and blue lines in Figure 3.2 (d) become identical. After 300 iterations, the cost function converges to a value of 0.37, while the RMSD reconstruction error converges to 0.92 – much lower than corresponding values in Figure 3.1. We note that the cost function in Figure 3.2 should not be expected to fully converge to zero, since the regularization term of Equation (3.2) does not vanish, even if the data fidelity term is zero. The local maximum observed in the field-based cost function shown in Figure 3.2 (d) suggests that the global minimum lies outside of the convex well of field-based optimization with the cold initialization. In other words, a convex-optimization approach to minimizing the field-based cost would lead to an incorrect local minimum, as observed in Figure 3.1 (b).

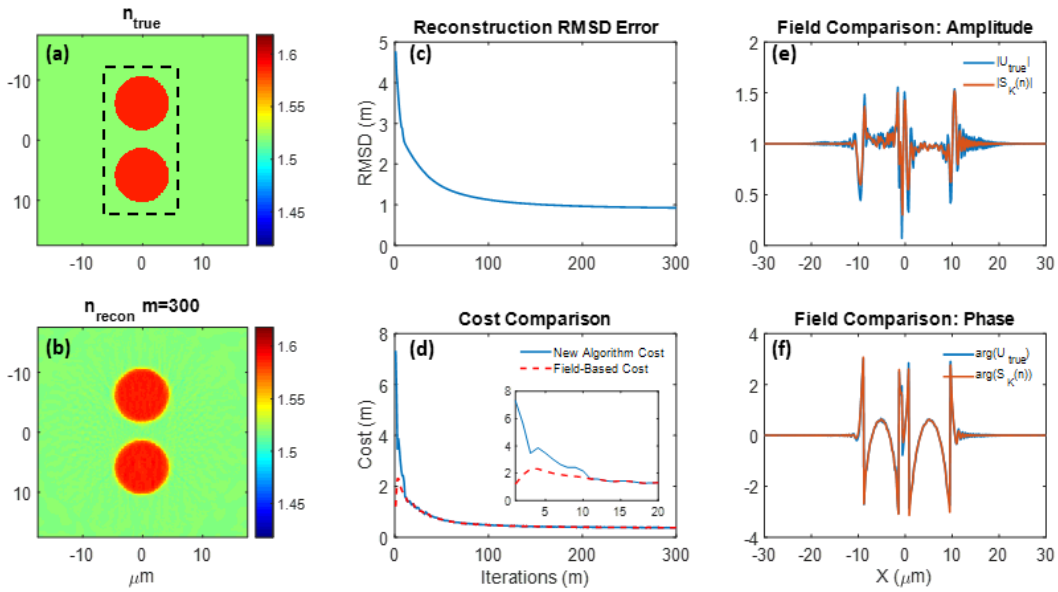

Figure 3.2: Two-disk phantom. (a) True object. The dashed box indicates the ROI used to calculate the RMSE in (c). (b) Reconstruction after 300 iterations using Algorithm 3.1. (c) RMSE. (d) Phase-based cost (blue) and field-based cost (red) as functions of iteration number. (e) Amplitude and (f) phase of true (blue) and reconstructed (red) fields for $\theta = 0°$.

The second example is a Shepp-Logan phantom with the same background RI and probe wavelength as before. The RI distribution of the phantom, shown in Figure 3.3 (a), uses the following parameters for the RI values: nb=1.518, n1=1.606, n2=1.627, n3=1.677, and n4=1.804. The field-based reconstruction results are shown in Fig 3. In this test, the field-based cost function converged to a local minimum of 0.82, corresponding to a reconstruction whose diffracted fields matched the amplitude and principal phase of the "measured" field in simulation. Although the diffracted fields, from the reconstruction and true objects, seemingly match closely, the RMSE of the reconstruction increased from 8.56 to 9.40, suggesting that the final reconstruction is farther from the true RI distribution than the "cold" initial estimate of the sample. This result further implies that, due to the cyclical nature of phase, multiple RI distributions introducing phase delays differing by integer multiples of 2π may produce similar diffracted fields. In order to use convex

optimization to minimize a fidelity criterion that compares the complex fields, the phase introduced by the initial RI estimate should be sufficiently close to that introduced by the true object, in order to avoid converging to a local minimum.

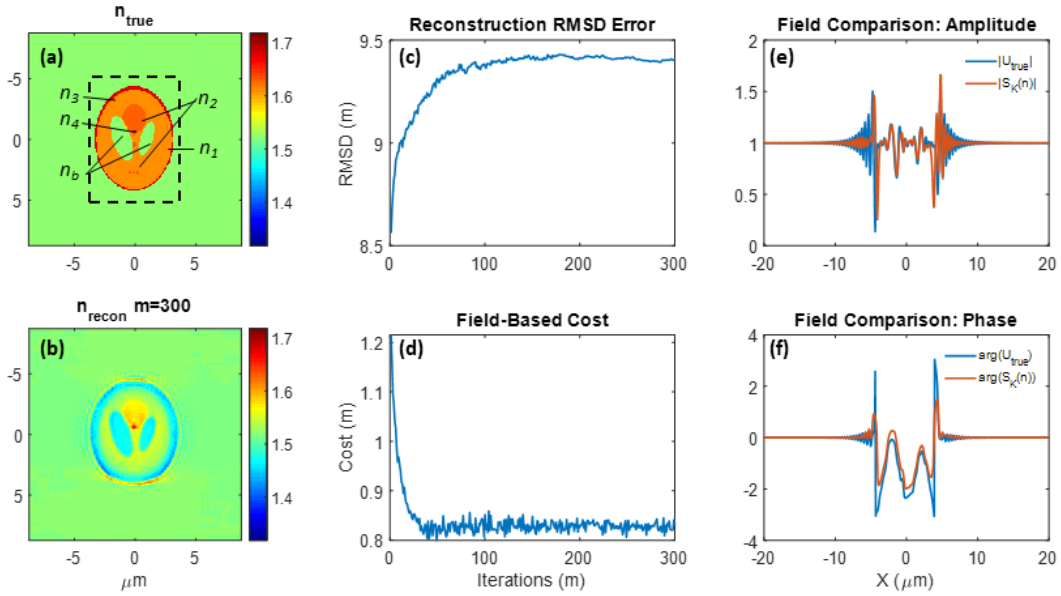

Figure 3.3: Shepp-Logan phantom. (a) True object. The dashed box indicates the ROI used to calculate the RMSE in (c). (b) Reconstruction after 300 iterations using the field-based fidelity criterion. (c) RMSE. (d) Cost. (e) Amplitude and (f) phase of true (blue) and reconstructed (red) fields for $\theta = 0°$.

Figure 3.4 shows results of reconstruction based a phase-based fidelity criterion (Algorithm 3.1) in the first 15 iterations followed by field-based criterion. A peak is observed in the field-based cost function (plotted for comparison purposes only) at iteration 2, while no corresponding peak is observed in the phase-based cost function. This suggests that the non-convex behavior of the field-based fidelity criterion towards the global minimum, which ultimately produced the local minimum shown in Figure 3.3, was not present when minimizing the difference in phase shift between the estimated and true objects. The cost function converged to a value of 0.28, while the

RMSE of the reconstruction dropped to 2.09, suggesting that the algorithm converged to an accurate reconstruction.

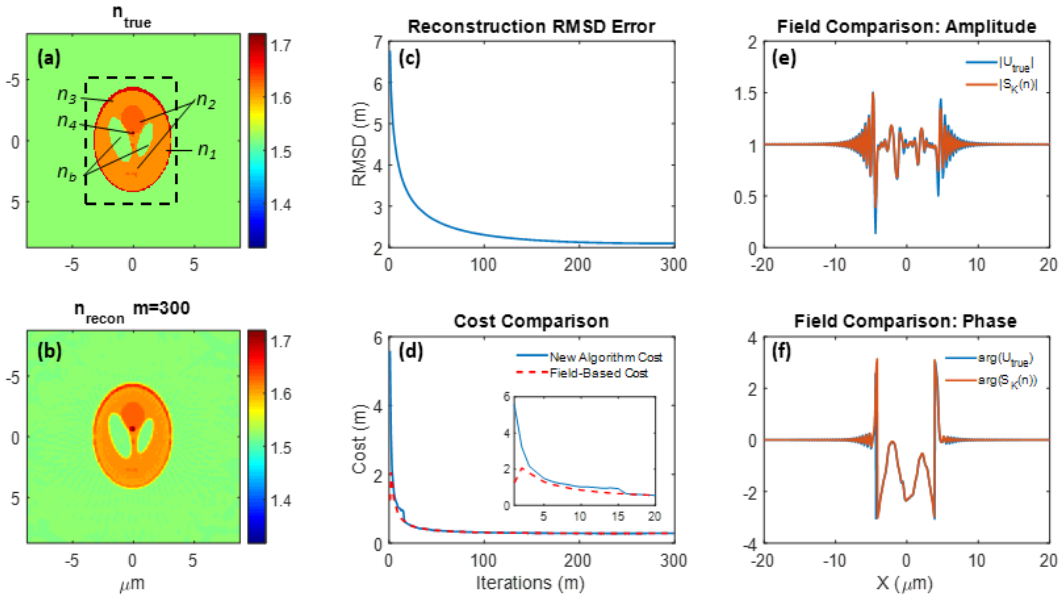

Figure 3.4: Shepp-Logan phantom. (a) True object. The dashed box indicates the ROI used to calculate the RMSE in (c). (b) Reconstruction after 300 iterations using Algorithm 3.1. (c) RMSE. (d) Phase-based (blue) and field-based (red) cost as functions of iteration number. (e) Amplitude and (f) phase of true (blue) and reconstructed (red) fields for $\theta = 0°$.

3.3.2 Experimental Validation

To experimentally validate our method, we perform reconstructions using raw data obtained from a commercial optical fiber profiler, the Intrafiber IFA-100. The experimental setup is an off-axis Mach-Zehnder interferometer, inside which an optical fiber sample is held, transverse to the illumination. The angular orientation of the fiber is controlled via a rotational motor. Diffracted field measurements are holographically obtained, using phase-shifting interferometry, for each orientation of the sample. The sample is illuminated using light from an incandescent source that is passed through a bandpass filter and linear polarizer. Although the small RI contrast of the optical fibers produce weak scattering, the size of the fibers produces large OPD across the

output fields. While accurate initial estimates of the fibers' RI can be obtained using linear reconstructions that are based on the unwrapped phase of the diffracted field (e.g., Rytov ODT inversions), we seek to demonstrate that the challenges posed by minimizing field-based cost functions for samples that contain large OPD still exist – even in the case of weak scattering – and can be overcome by instead optimizing on the unwrapped, complex-valued phase. The reconstruction area used for experimental validation was 183×1383 pixels, each of dimension dx = 0.184 μm. Due to the larger volume of the following reconstructions, each iteration of Algorithm 3.1 took, on average, 24 seconds to complete.

For the first experiment, we choose a "PANDA-type" polarization-maintaining single-mode optical fiber. The fiber is known to contain a stepwise RI distribution that includes two pronounced, circular stress rods on either side of the fiber core. For this experiment, a 650 nm, 10 nm wide bandpass filter was used for illumination. The background RI of the index-matching oil at 650 nm is nb=1.4566. Although the background medium is matched closely to the cladding of the fiber, the resultant OPD from the measured fields still exceed 2π, due to the 125 μm fiber diameter, and so phase-unwrapping must be used to correctly measure the fiber's OPD. Since we do not know the exact values of the fiber's RI distribution, we apply no constraint to the maximum or minimum RI possible in reconstructions.

As shown in Figure 3.5, because of the large OPD of the panda fiber, the reconstruction obtained using a purely field-based fidelity criterion fails to provide a correct RI profile of the fiber. Despite the erroneous, elliptical cladding-like feature around the fiber's center, diffracted fields from the reconstruction are similar to the respective fields obtained in experiment. The final value of the cost function, after convergence to the minimum, is 0.82. Similar to the simulated 2-

disk experiment before, convergence to this local minimum suggests that the success of convex optimization using a field-based fidelity criterion must either rely heavily on the initial estimate of the sample or use a "warm" initialization and/or constraints based on a-priori knowledge of the sample, to obtain correct reconstructions.

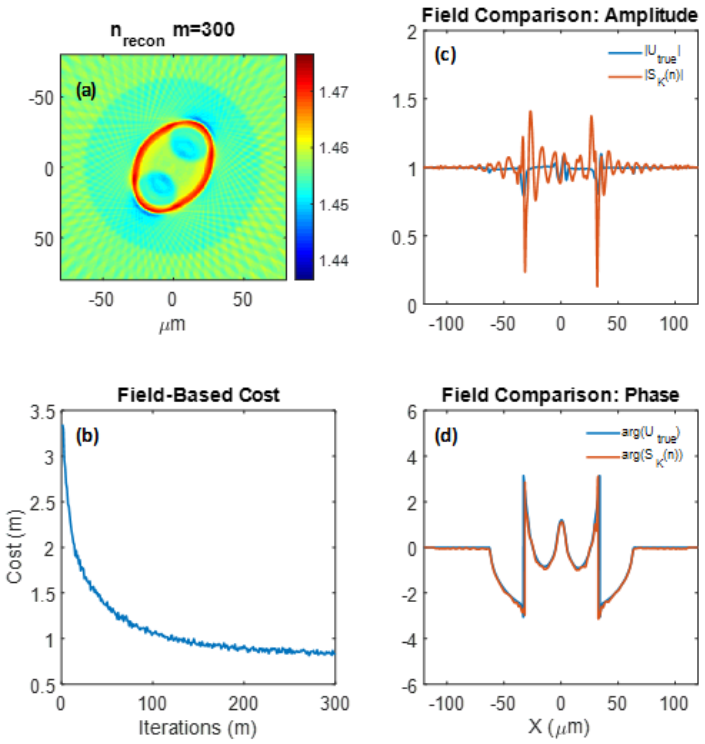

Figure 3.5: (a) Reconstructed RI distribution of a Panda fiber after 300 iterations, using the field-based fidelity criterion for experimentally measured diffracted fields. (b) Cost as a function of iteration number. (c) Amplitude and (d) phase of the true (blue) and reconstructed (red) fields for $\theta = 0°$.

The reconstruction obtained using Algorithm 3.1 (Figure 3.6) shows a RI profile consistent with a typical, commercial panda fiber. Algorithm 3.1 optimized on a phase-based fidelity criterion for the first 7 iterations, and a field-based criterion thereafter. Unlike the reconstruction shown in Figure 3.5, two stress rods are now clearly visible, along with an inner cladding region and core. Additionally, the final value of the cost function of 0.12 suggests Algorithm 3.1 converged to a

more accurate minimum than before. Like earlier reconstructions of simulated objects, the field-based cost in Figure 3.6 shows a peak around iteration 3.

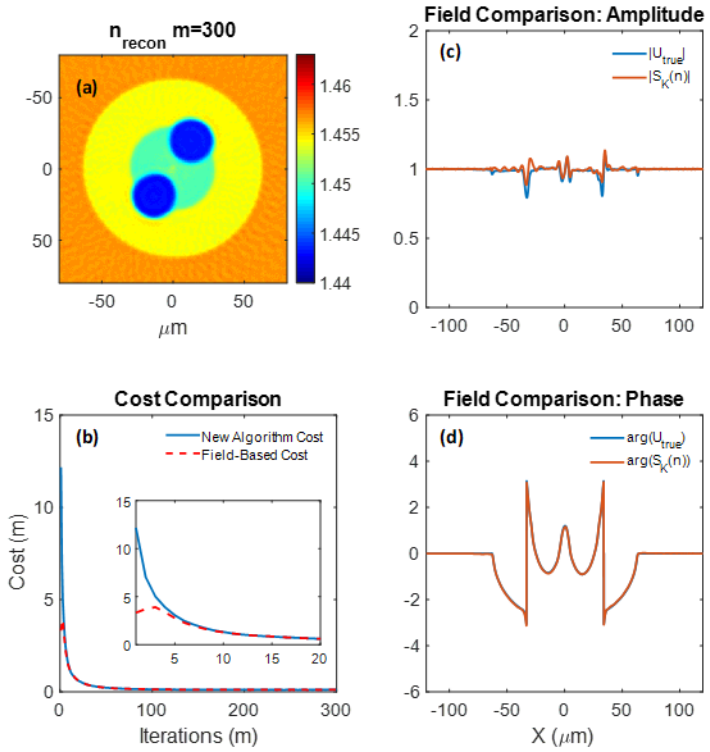

Figure 3.6: (a) Reconstructed RI distribution of a Panda fiber after 300 iterations, using Algorithm 3.1 for experimentally measured diffracted fields. (b) Phase-based cost (blue) and field-based cost (red) as functions of iteration number. (c) Amplitude and (d) phase of the true (blue) and reconstructed (red) fields for $\theta = 0°$.

The object for the second experiment is a hollow-core fiber (HCF), filled with dimethyl sulfoxide (DMSO) by means of capillary action. The fiber is known to have a glass cladding within an outer diameter of 169 μm, and inner diameter of 85 μm. The "hollow" core region itself contains seven 23 μm diameter glass capillaries, each with a thickness of 400 nm. The core region, and the capillaries within it are filled with the DMSO liquid. For this experiment, the fiber is illuminated at $\lambda 0 = 615$ nm. The associated RI of the background medium (matching liquid) at the probe wavelength is nb = 1.4577. The total phase shift induced by the fiber is measured to be larger than

2π. Results of field-based reconstruction are shown in Figure 3.7. For cold initialization, the cost function converged to a minimum of 0.74 corresponding to an RI distribution whose diffracted fields matched the measured fields. The reconstructed RI shown in Figure 3.7 (a) is believed to be incorrect since we know that the index in core region is uniform with value equal to that of DMSO.

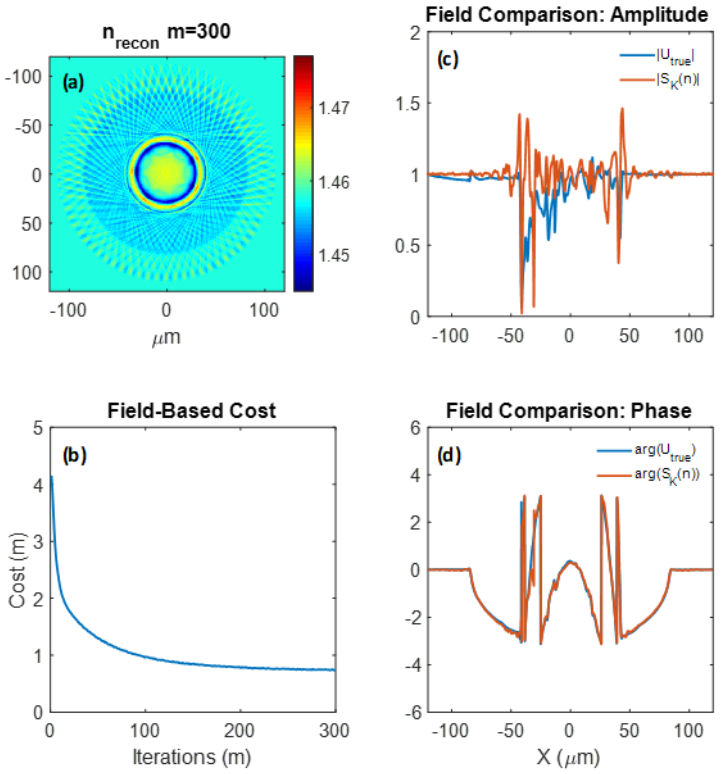

Figure 3.7: (a) Reconstruction of the RI distribution of a hollow-core fiber filled with DMSO using experimentally measured diffracted fields and optimizing on a field-based fidelity criterion for 300 iterations. (b) Cost as a function of iteration number. (c) Amplitude and (d) phase of the true (blue) and reconstructed (red) fields for θ = 0°.

As shown in Figure 3.8, phase-based reconstruction matches more closely with our prior knowledge of the sample's structure. Unlike the field-based reconstruction, the RI values now correspond to three distinct regions: the background oil, glass capillaries of the HCF, and the DMSO liquid which fills the core region. Unlike the reconstruction in Figure 3.7 (a), the structure of the glass capillaries inside the core region are now clearly defined. The cost function converges

quickly to a value of 0.43, indicating that the reconstructed object produces diffracted fields more consistent with the measured fields. The field-based cost in Figure 3.8 (b) exhibits a peak during optimization in which the phase-based fidelity criterion is used, showing the purely field-based fidelity criterion must climb out of the well-of-convergence to the local minimum shown in Figure 3.7 (a), before being able to converge to the minimum shown in Figure 3.8 (a).

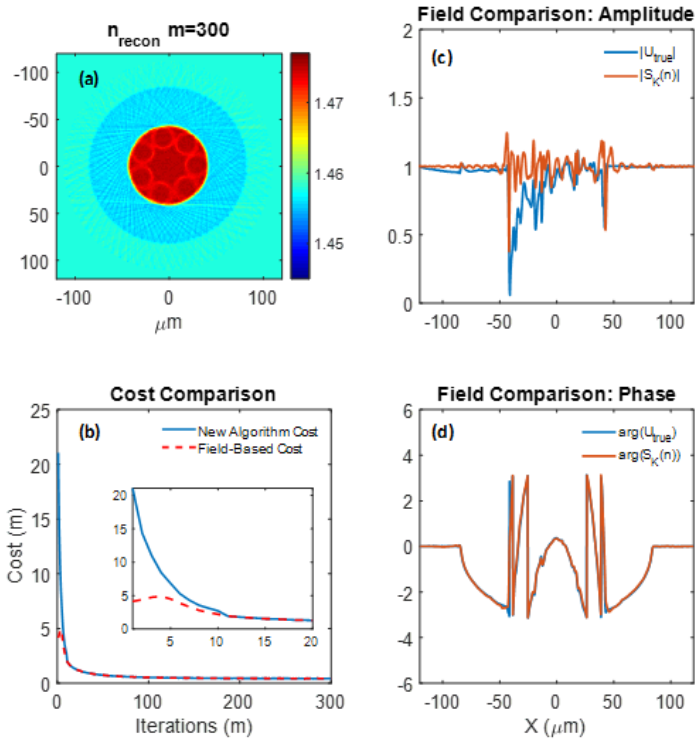

Figure 3.8: (a) Reconstruction of the RI distribution, after 300 iterations of Algorithm 3.1, of a hollow-core fiber filled with DMSO using experimentally measured diffracted fields. (b) Phase-based cost (blue) and field-based cost (red). (c) Amplitude and (d) phase of the true (blue) and reconstructed (red) fields for $\theta = 0°$.

3.3.3 Convergence Study

To reduce computational complexity and avoid unnecessary unwrapping at each iteration, Algorithm 3.1 switches its fidelity criterion from one based on (unwrapped) phase, to one that compares fields. While doing so may improve overall computational speed, since no unwrapping

algorithm is used after the swap condition, the rate of convergence when optimizing with either criterion is not guaranteed to be the same. In the following study, the rates of convergence, over 100 iterations, are compared using the RMSE of reconstructions, as functions of iteration number, obtained using a cost that contains a field-based fidelity criterion, and a phase-based fidelity criterion. For this comparison study, a phantom distribution is chosen with a maximum phase delay near π, but small enough such that optimizing either cost yields an accurate solution. Next, the test is repeated using the same distribution, but with a contrast that produces a phase delay much smaller than π. For each test, we optimize over 100 iterations.

For the first test, shown in Figure 3.9, the Shepp-Logan distribution from Figs 3.3, 3.4 is used, with an RI contrast scaled to produce a phase delay near π, and a second test with a phase delay much smaller than π. In the higher-contrast case, optimizing the phase-based cost initially converges more efficiently than the field-based counterpart. In the lower-contrast case, however, both cost functions converge at a similar rate. This test was repeated for other samples, and similar conclusions were reached. This study demonstrates that the swap condition from Algorithm 3.1, which swaps the fidelity criterion when the phase delay is near π can be further tuned to enhance computational efficiency.

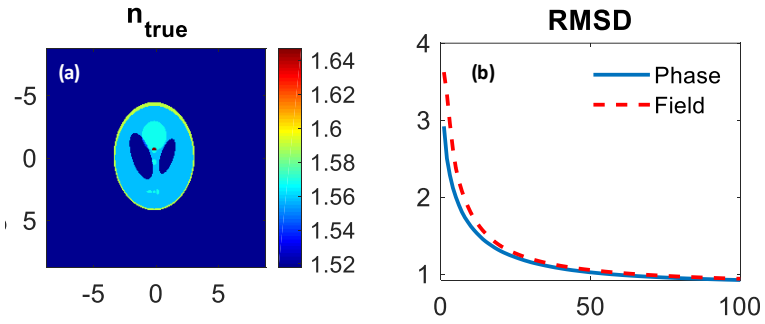

Figure 3.9: Convergence study for Shepp-Logan phantom. (a) Phantom RI distribution. (b) RMSD as a function of iteration number, for cost function based on field (red) and phase (blue).

CHAPTER 4: ITERATIVE OPTICAL DIFFRACTION TOMOGRAPHY WITH EMBEDDED REGULARIZATION

In this chapter, I describe a new method in which total-variation regularization is applied at each iteration of an iterative framework for optical diffraction tomography. The performance of this approach was validated by numerical and experimental tests on various highly scattering objects, which were previously used to demonstrate an iterative ODT reconstruction technique developed by my group [22]. Significant improvement in reconstruction SNR were demonstrated. This work was recently submitted to Optics Express and is currently under review.

4.1 Introduction

An iterative Rytov-based ODT (iODT) algorithm [22] has recently been used for reconstruction of highly scattering objects. This algorithm works by forward propagating the known input field and backward propagating the measured output fields through an estimate of the sample's RI distribution, for each illumination angle. The differential Rytov phase between these two fields is then used in a filtered backpropagation framework to calculate the error in the estimate of the sample. This error is then subtracted from the estimate to obtain a more accurate update of the RI distribution, and the process is repeated recursively.

One of the limitations of the iODT algorithm, under conditions of high-contrast RI distributions, is that the phase of the forward and backward propagated fields may become ill-defined in areas of the scattering volume where the fields contain small amplitudes. When this occurs, the Rytov phases used to reconstruct the RI become contaminated with phase-vortices that introduce challenges to correct phase unwrapping resulting in reconstruction artifacts. We have

found that regularized optimization-based approaches that minimize a cost function based on the complex fields, or their respective complex phases [31, 33, 41, 42], can be particularly effective at achieving accurate reconstructions for such objects because the iterative use of regularization (e.g., total-variation) alleviates challenges associated with poorly behaved signal, or missing information. Unfortunately, optimization algorithms that are based on a field fidelity criterion typically require a sufficiently accurate initial estimate to converge to a correct solution [33, 48]. Furthermore, gradient-descent approaches may take several dozens of iterations before sufficiently converging to a solution. Unlike convex optimization approaches, however, iODT seeks a new "best estimate" of the sample's RI distribution, rather than a gradual "descent" to the correct solution. This perturbative approach gives iODT an advantage in computational efficiency over optimization-based solutions.

Here, we introduce and validate a new strategy that combines iODT's efficient framework with the benefits of regularized optimization techniques. This is achieved by applying total-variation (TV) regularization [31, 49, 50, 51] in each iteration of the standard iODT algorithm. We call this method regularized iODT (R-iODT). We have validated this technique using simulated data and an experimental test and concluded that a substantial improvement in the signal-to-noise ratio (SNR) of reconstructions was obtained. Application of TV regularization at each iteration is significantly better than its application after the termination of the iteration.

4.2 R-iODT Validation

4.2.1 iODT Algorithm

The iODT algorithm [22], summarized in Algorithm. 4.1, uses a Rytov-like approach to iteratively reconstruct the RI distribution by using the complex-valued phase of diffracted fields. The "true," or "measured," diffracted fields are recorded holographically for each illumination angle in experimental tests [20, 52, 53], or numerically simulated by propagating the known input field through phantoms using a numerical solver such as the beam propagation method, or finite-difference time-domain (FDTD) method [45, 54]. The object function, $f(x,y)$, described in Algorithm 4.1 is related to the RI by $f(x,y) \equiv k_o^2[n^2(x,y) - n_b^2]$, where k_o is the wavenumber $2\pi/\lambda_o$, and n_b is the background RI. As shown in Figure 4.1, propagation is performed in local coordinates (ξ,η), which relate to the global coordinates (x,y) by the transformation $x = \xi\cos\theta - \eta\sin\theta$, $y = \xi\sin\theta + \eta\cos\theta$. The true fields are measured along the local coordinate axis η, while propagation for each illumination angle θ is along the ξ axis.

Algorithm 4.1. iODT

input: u_0, u_t, $f^{(0)}$, $m_{\max}$
set: m=0, θ, $\boldsymbol{\mathcal{C}}$, $\boldsymbol{\mathcal{S}}$
repeat:
  $u_{\text{fwd}}^{(m)}(\xi,\eta,\theta) \leftarrow \boldsymbol{\mathcal{S}}\left[u_0, f^{(m)}(x,y), \theta\right]$ ▷ Propagation
  $u_{\text{bwd}}^{(m)}(\xi,\eta,\theta) \leftarrow \boldsymbol{\mathcal{S}}^{-1}\left[u_t, f^{(m)}(x,y), \theta\right]$
  $\Delta\phi_{\text{R}}^{(m)}(\xi,\eta,\theta) \leftarrow \ln\left[u_{\text{fwd}}^{(m)}(\xi,\eta,\theta)/u_{\text{bwd}}^{(m)}(\xi,\eta,\theta)\right]$ ▷ Inversion
  $\Delta\Pi^{(m)}(\xi,\eta,\theta) \leftarrow \Delta\phi_{\text{R}}^{(m)}(\xi,\eta,\theta)\cdot|k_\eta|$
  $\Delta f^{(m)}(x,y) \leftarrow -j2\pi k_b \int_0^{2\pi} \Delta\Pi^{(m)}(\xi,\eta,\theta)\mathrm{d}\theta$
  $f^{(m)}(x,y) \leftarrow f^{(m)}(x,y) - \Delta f^{(m)}(x,y)$ ▷ Update
  $f^{(m)}(x,y) \leftarrow \boldsymbol{\mathcal{C}} f^{(m)}(x,y)$ ▷ Constraint
  $m \leftarrow m+1$
until stopping condition
return $f^{(m)}$

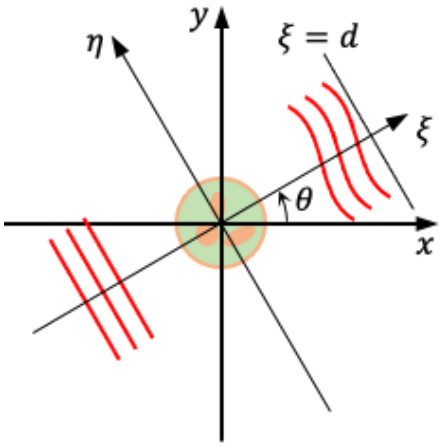

Figure 4.1: Schematic of an ODT experiment. Plane wave k_b illuminates the sample at θ and travels along ξ direction. The scattered field is measured on the screen at $\xi = d$ along the η direction. The illumination angle is changed and the process is repeated.

Using an initial guess of the sample $f^{(0)}$, the iODT algorithm takes a known input field u_0 for each illumination angle θ and forward propagates it through the sample to create $u_{\text{fwd}}^{(m)}(\xi, \eta, \theta)$. Likewise, the respective measured field for each illumination angle is backpropagated through the estimated RI to generate a field $u_{\text{bwd}}^{(m)}(\xi, \eta, \theta)$. The forward and backward propagation is implemented using solvers, denoted by $\mathcal{S}$ and $\mathcal{S}^{-1}$, respectively. In this paper, we elect to use a "cold" initialization ($f^{(0)} = 0$) of the object's distribution. For each iteration m, a differential "Rytov" phase, $\Delta\phi_{\text{R}}$ is calculated and used to reconstruct the estimated *error* in the estimated distribution of the object $\Delta f^{(m)}$, which is subtracted from the current estimate of the object $f^{(m)}$ to form a new estimate for the next iteration. The framework for 3-dimensional objects is straightforward but requires an updated Green's function to perform field propagation and inversion. For computational brevity, we elect to perform reconstructions on two-dimensional objects, or 2-D cross-sections of extended objects (e.g., optical fibers).

Due to the multivalued nature of the algorithm used to calculate the Rytov phase, it is necessary to apply a phase-unwrapper is necessary on the imaginary part of $\Delta\phi_{\mathrm{R}}$. For this study, we elect to use an L-2 norm phase-unwrapper [55] to perform this task. For objects that produce large amounts of scattering, the phase may contain local features *vortices*, where the value of the phase is ill-defined. Such vortices may introduce artifacts and even inhibit the process of unwrapping, thereby leading to reconstructive error.

At the end of each iODT iteration, constraints, denoted by the $\mathcal{C}$ operator, may be applied to the current estimate of the object (e.g., non-negativity). In this paper, we expand the iODT constraint operator to include TV-based regularization (e.g., TV), which is applied to the current estimate of the object at the end of each iteration. By doing so iteratively, the iODT algorithm can suppress artifacts caused by poor data quality, poorly behaved phase features due to phase unwrapping, or the presence of phase vortices.

This process is repeated until a stopping criterion is satisfied. For cross-comparison purposes, we elect to run the iODT (and R-iODT) algorithm(s) for a set number of iterations, $m_{\max}$, which is specified for each experiment. The stopping condition, described in Algorithm 4.1, is based on the convergence of the normalized root-mean-square (nRMS) errors in amplitude and phase of the sinogram:

$$\epsilon_A(m) \equiv \frac{\sqrt{\sum_\theta \left[\left|u_t^\theta\right| - \left|u_{fwd}^\theta\right|\right]^2 / N_\eta}}{\mathrm{range}\left[\left|u_t^\theta\right|\right]}, \tag{4.1}$$

$$\epsilon_\phi(m) \equiv \frac{\sqrt{\sum_\theta \left[\mathrm{Arg}\left[u_t^\theta / u_{fwd}^\theta\right]\right]^2 / N_\eta}}{\mathrm{range}\left[\mathrm{Arg}\left[u_t^\theta / u_{fwd}^\theta\right]\right]}, \tag{4.2}$$

where u_t^{θ} and u_{fwd}^{θ} are the "true" (or measured) and simulated forward-propagated field, for a given illumination angle θ, and N_η denotes the number of pixels on the detector. In the standard iODT algorithm [22], the stopping criteria is satisfied when both Equations (4.1) and (4.2) are smaller than a prescribed value δ_{thresh}, (set to ~10^{-3}) over a number of successive iterations Q, or until the algorithm runs for a maximum number of iterations, $m_{\max}$.

4.2.2 TV Algorithm

TV regularization is a popular regularization choice for convex optimization problems in tomographic phase imaging. One TV regularization approach, developed by Beck and Teboulle [51], and used in [31], employs a "dual approach" method to apply TV regularization on a reconstructed RI distribution. The modular nature of this approach is particularly useful for iODT since it accepts an input of an RI distribution, along with hyperparameters and constraints to return a new RI image with TV enhancement applied. We elect to adopt this modular TV algorithm so that both constraints on the RI distribution and regularization can be included in the $\boldsymbol{\mathcal{C}}$ operator in Algorithm 4.1 at the end of every iteration. This modular dual approach — specifically for isotropic TV in our study — is shown in Algorithm 4.2 (from Appendix B in [31]), in which $\mathbf{D}$ is the discrete gradient operator applied to the input image (or datacube), proj_χ is a projection used to apply constraints, such that the values of the vectorized input RI distribution $\mathbf{x}$ are truncated to lie between $n_{\min}$ and $n_{\max}$, $[\mathbf{g}]_n \in \mathbb{R}^{3\times \boldsymbol{N}}$ is the gradient vector field of the discretized image $\boldsymbol{x} \in \mathbb{R}^{\boldsymbol{N}}$ at the pixel position $n \in [1, \dots, N]$, and $\text{proj}_{\mathcal{G}}$ is the projection used in the case of isotropic TV:

$$\left[\text{proj}_{\mathcal{G}}(\mathbf{g})\right]_n \equiv \frac{[\mathbf{g}]_n}{\max(1, \|[\mathbf{g}]_n\|_{\ell 2})}. \tag{4.3}$$

Algorithm 4.2. $\mathcal{C}$ operator (isotropic TV regularization)

input: $\boldsymbol{z} \in \mathbb{R}^N$, $n_{\min}$, $n_{\max}$, $\tau > 0$
set: $t \leftarrow 1,\ \mathbf{d}^0 \leftarrow \mathbf{g}^0,\ q_0 \leftarrow 1,\ \gamma \leftarrow 1/12\tau$
repeat:
  $\mathbf{g}^{\mathrm{t}} \leftarrow \mathrm{proj}_{\mathcal{G}}\left(\mathbf{d}^{t-1} + \gamma \mathbf{D}\left(\mathrm{proj}_{\chi}(\boldsymbol{z} - \tau\, \mathbf{D}^T \mathbf{d}^{t-1})\right)\right)$
  $\mathbf{x}^{\mathrm{t}} \leftarrow \mathrm{proj}_{\chi}(\boldsymbol{z} - \tau\, \mathbf{D}^T \mathbf{g}^t)$
  $q_t \leftarrow \frac{1}{2}\left(1 + \sqrt{1 + 4q_{t-1}^2}\right)$
  $\mathbf{d}^{\mathbf{t}} \leftarrow \mathbf{g}^t + ((q_{t-1} - 1)/q_t)(\mathbf{g}^t - \mathbf{g}^{t-1})$
  $t \leftarrow t + 1$
until stopping condition
return x^{t}

4.3 R-iODT Validation

In this section, we validate R-iODT through both simulations and experiments. To numerically validate R-iODT, reconstructions are performed on various phantoms that either exhibit complicated structure or large optical path-length difference (OPD). Data for the "true" sinogram fields is obtained using a FDTD solver with a grid spacing of $\lambda_o/20$, over a 360° span of illumination angles θ, in 5° increments. The illumination wavelength is $\lambda_o = 1$ μm. For each simulation, a reconstruction was performed using the standard iODT algorithm, with real-valued constraints on the RI distribution, and another using TV regularization, with the same constraints.

For samples whose RI distribution is known (i.e simulations in Sec. 4.2.1), the signal-to-noise-ratio

$$\mathrm{SNR} \equiv 10 \cdot \log_{10}\left(\frac{\|n_t - n_b\|_2^2}{\|n_t - n_{rec}\|_2^2}\right)\ \mathrm{dB} \tag{4.3}$$

is presented for both standard iODT and R-iODT, where n_t is the true RI distribution, n_b is the background RI distribution, and n_{rec} is the respective reconstructed RI distribution for the current iteration. For these samples, the values for $n_{\min}$ and $n_{\max}$ are set to $-\infty$ and $+\infty$, respectively, to

lift constraints on the real part of the RI distribution. The imaginary RI was forced to be zero (corresponding to no loss or gain constraint).

4.3.1 Validation through Simulation

In the first example, Phantom 1, a simple distribution with high index contrast consisting of three disks, shown in Figure 4.2 (a), was used. Each disk has a 4.5 μm radius, and RI of 1.348. The background RI n_b is 1.518. For this simulation, phase unwrapping was turned off after 10 iterations. As shown in Figure 4.2 (c), while the phase unwrapping allowed iODT to obtain a maximum reconstructed SNR of 16.5 dB upon turning off phase unwrapping at the $m = 11$ iteration, phase vortices introduce artifacts at each subsequent iteration, which result in an overall degradation in SNR to 12.8 dB at iteration 50 (Fig 4.2 (b)). The R-iODT reconstruction, however, shows a better SNR of 17 dB upon turning off phase unwrapping, and finishes with an SNR of 23.2 dB after 50 iterations. A maximum SNR of 23.7 dB is obtained using R-iODT, as shown in Figure 4.2 (b) around the $m = 28$ iteration, suggesting that iterative artifacts caused by phase vortices are suppressed, but not eliminated, by TV regularization.

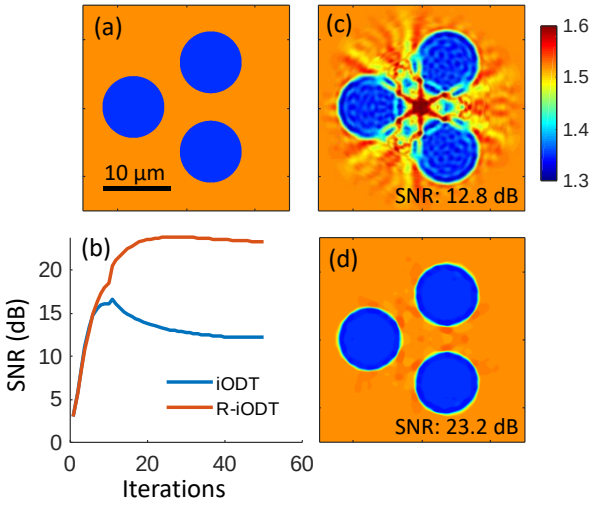

Figure 4.2: (a) Phantom 1 RI distribution, (b) SNR of the iODT and R-iODT reconstructions over the first 50 iterations. (c and d) Respective iODT and R-iODT reconstructions at the m= 50 iteration.

For Phantom 2, a more complex, walled, cell-like structure, shown in Figure 4.3 (a), was used with the background RI n_b = 1.518, n_1 = 1.378, n_2 = 1.358, n_3 = 1.548, and n_4 = 1.568. The SNR of the reconstruction, shown in Figure 4.3 (b), shows that the R-iODT algorithm climbs to a progressively higher SNR reconstruction, while the iODT reconstruction obtains a maximum SNR of 14 dB at iteration 16, after which artifacts cause a steady degradation in reconstructive accuracy.

The nRMS errors of the output fields' amplitude and phase are respectively plotted in Figure 4.3 (c and d), and show that both algorithms yield reconstructions that reduce error in output fields, even though the iODT reconstruction contains a larger SNR error. This suggests that regularization can guide the algorithm away from possible solutions that presumably contain higher total variance than the correct distribution. Using $Q = 10$ for the stopping criterion outlined in 4.2.1, based on the ϵ_A and ϵ_{ph} plots in Figure 4.3 (c) and (d), respectively, the iODT algorithm would have satisfied the stopping criterion in Algorithm 4.1 at the $m = 43$ iteration, and the R-iODT algorithm at the $m = 49$ iteration, with corresponding reconstructions shown in Figure 4.4

(e and f). The iODT and R-iODT reconstructions after the m=50 iteration are shown in Figure 4.3 (g and h).

The plots in Figure 4.3 (b-d) exhibit a non-smooth feature at the m=10 iteration, marking the iteration where phase-unwrapping is turned off. Unlike iODT, however, a noticeable drop in the ϵ_A and ϵ_{ph} nRMS errors for R-iODT near iteration 30, suggesting that the algorithm was able to "lock on" to a solution that better matched both the output fields and the correct RI distribution. The standard iODT algorithm, however, shows a decline in both nRMS error and SNR, suggesting that the algorithm was trapped in a solution whose output fields that match the measured ones, but contains the incorrect RI distribution.

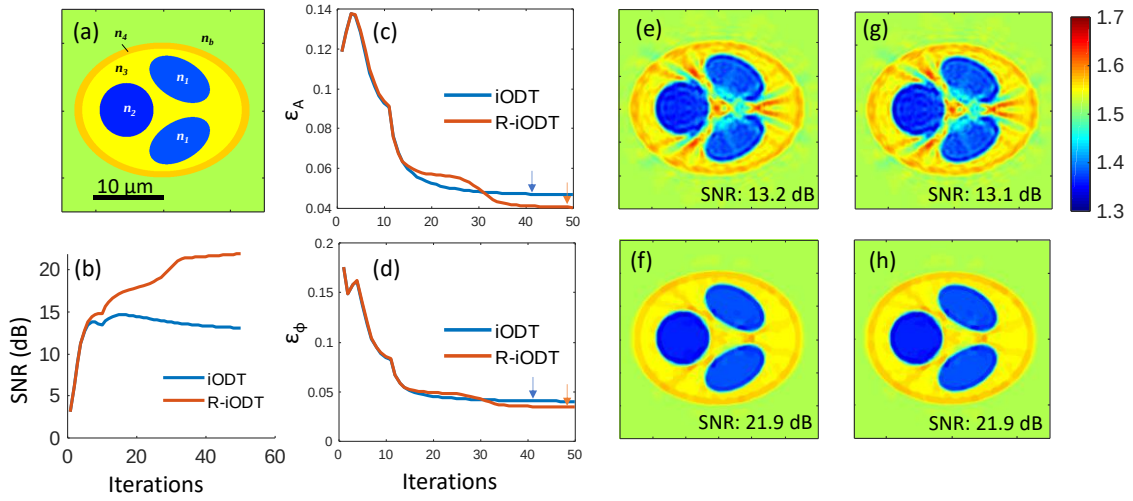

Figure 4.3: (a) Phantom 2 RI distribution, (b) SNR of the iODT and R-iODT reconstructions over the first 50 iterations. (c and d) nRMS errors in amplitude and phase of the sinogram ϵ_A and ϵ_ϕ for iODT and R-iODT, over the first 50 iterations. Blue and red arrows are used to mark the iteration where the stopping criterion is satisfied. (e) iODT reconstruction after stopping criterion satisfied (m=43). (f) R-iODT reconstruction after stopping criterion satisfied (m=49). (g and h) Respective iODT and R-iODT reconstructions after m= 50 iterations.

As demonstrated in Figures 4.2 (c) and 4.3 (e) for Phantoms 1 and 2, the iODT algorithm is sensitive to phase-vortex contamination of the Rytov phase. These vortices can appear in objects with large OPDs, as well as objects of complicated structure, whose features contain large RI

contrast. To demonstrate the effectiveness of R-iODT for such objects, reconstructions are performed on Phantom 3, a 19-disk distribution shown in Figure 4.4 (a), where n_b=1.518, n_1=1.38, and n_2=1.418. Although the overall OPD of the object is less than 2π, the complicated structure of many small, high-contrast features produces phase vortices that contaminate the Rytov phase. Although iODT and R-iODT have similar SNR upon turning off phase unwrapping at iteration 15, phase vortex artifact contamination limits the SNR of the iODT reconstruction to 4.5 dB. Like the previous objects, the contaminated phase introduces error at each iODT iteration, which begin to lower the SNR of the iODT reconstruction after iteration 22. For R-iODT, these artifacts are suppressed at each iteration, allowing the algorithm to reach an SNR of 15.9 dB.

For the three simulations above, each iODT iteration takes on average of 35 seconds to complete. The R-iODT algorithm differs only in the use of a TV-enhancement step at the end of each iteration. The latter method, on average takes 42 seconds to complete. The code for the iODT algorithm, however, has been optimized for the CPU and unparallelized computation, and much shorter iteration times are possible.

To assess the feasibility of reducing the computational burden of R-iODT versus the standard iODT, we compare the SNR of R-iODT (TV regularization at each iteration) to a reconstruction where TV regularization is performed only once, after the final iODT reconstruction. The result, shown in Figure 4.5 (c), has an SNR of 4.7 dB, demonstrating that the R-iODT algorithm that is shown in Figure 4.5 (b) reconstructs more accurately when TV regularization is applied at each iteration (or every few iterations) rather than after the final iODT reconstruction.

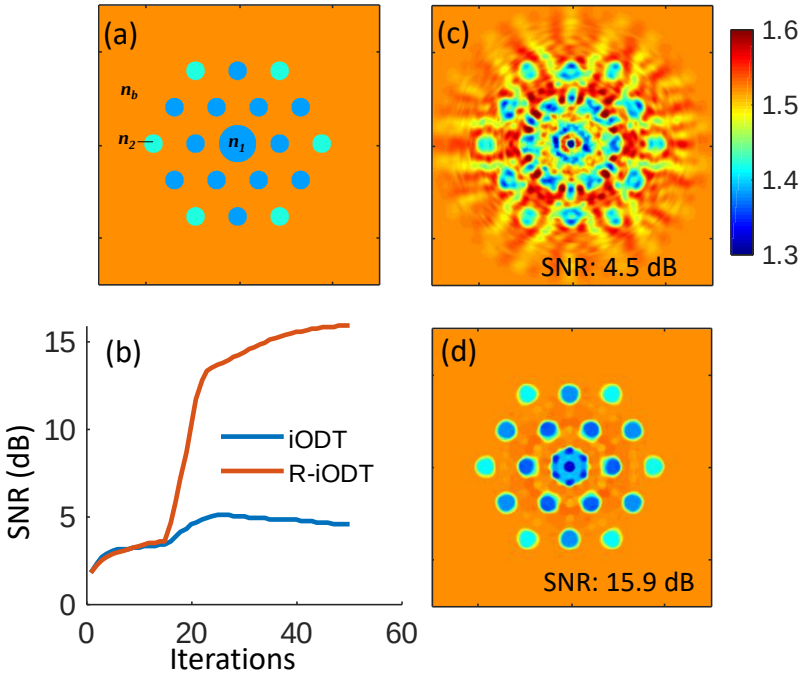

Figure 4.4: (a) Phantom 3 RI distribution, (b) SNR of the iODT and R-iODT reconstructions over the first 50 iterations. (c) and (d) Respective iODT and R-iODT reconstructions after $m = 50$ iterations.

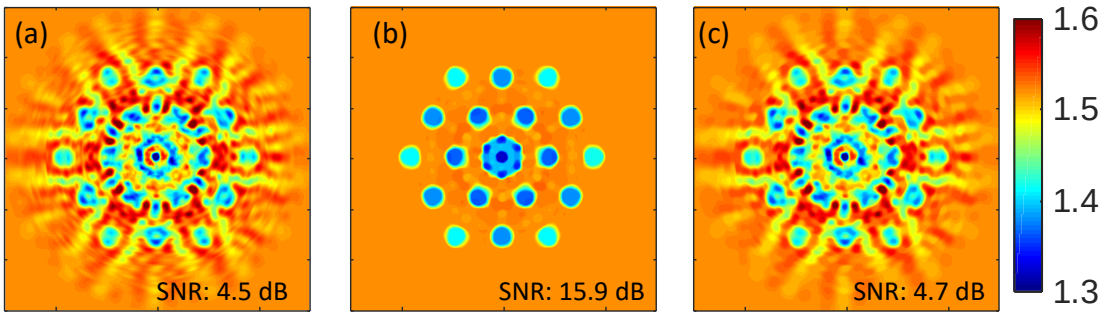

Figure 4.5: Phantom 3 reconstructions (a) iODT, (b) R-iODT using TV at each iteration, and (c) iODT with TV regularization applied to final ($m = 50$) reconstruction.

While the numerical validation of R-iODT, using TV regularization, has shown considerable improvement over the standard iODT algorithm, the choice of the type of regularization used for the type of sample must be carefully made. When reconstructing features that are of similar scale to the resolution limit of ODT (i.e., $\sim\lambda_o/2$), the TV enhancement may

lower the overall SNR of small, reconstructed features if the algorithm is unable to sharpen such features while preserving their correct values. For such samples, a more sophisticated regularization approach may be considered.

4.3.2 Experimental Validation

We have applied the R-iODT algorithm to holographically measured ODT data taken on a 19-core step-index multicore fiber using an Intrafiber IFA-100 optical fiber profiler at λ_0 = 630 nm. The raw dataset used is the same as in [22]. Reconstructions using the standard iODT without TV regularization, applying TV regularization once after the final standard iODT iteration, and using R-iODT are shown in Figure 4.6. A cleaner reconstruction in the central region of the fiber is observed when iteratively applying regularization in the R-iODT algorithm. The pixel size for the reconstruction is Δx = 0.184 μm, and the diffracted fields are measured on the object over 36 angles, ranging from 0° to 175°, in intervals of 5°.

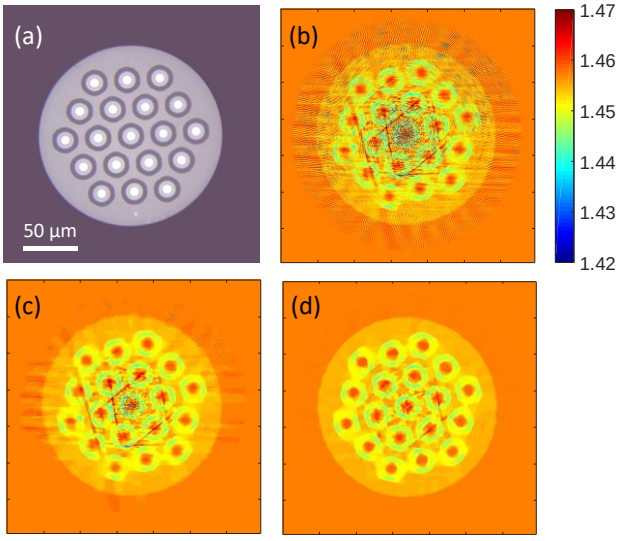

Figure 4.6: Reconstructions based on experimental measurements of a multicore optical fiber (a) SEM of fiber, (b) iODT, (c) iODT with TV regularization applied to final iteration ($m = 50$), and (d) R-iODT using TV at each iteration.

CHAPTER 5: EXPERIMENTAL AND NUMERICAL 3D RECONSTRUCTIONS

The majority of the ODT reconstructions presented in Chapters 2-4, and in [22, 33, 40, 48, 56] have been for either 2-D numerical phantoms, or of 2-D cross-sections of extended 3-D cylindrical objects (e.g., optical fibers). The reason for using such objects was two-fold: (i) 2-D reconstructions provide results that are, in principle, analogous to 3-D counterparts and (ii) 3-D reconstructions are significantly more computationally intensive. To move beyond the 2-D domain, I have expanded the iODT and optimization-based framework from 2-D to 3-D, and updated the field propagation models for this purpose. I have also built an ODT experimental setup capable of more general tomographic phase imaging in order to test the new 3D reconstruction methods.

5.1 ODT Experimental Setup

Our initial experimental data that were used to verify 2D reconstruction were obtained by use of the Intrafiber IFA-100 profilometer shown in Figure 5.1. This setup, which employed a Mach-Zehnder interferometer (MZI), was used exclusively to reconstruct 2D cross-sections of optical fibers' RI profile. The instrument worked by rotating a fiber about its axis to a set of angles, and measuring a hologram for each angle, respectively. Because optical fibers are spatially invariant along one axis, diffracted fields extracted from the profiler's holograms were averaged into representative 1D diffracted fields from a 2D object (i.e., the 2D RI cross-section of the fiber) for each illumination angle. Next, an ODT algorithm (e.g., iODT) was used to reconstruct the cross-section of the fiber's RI.

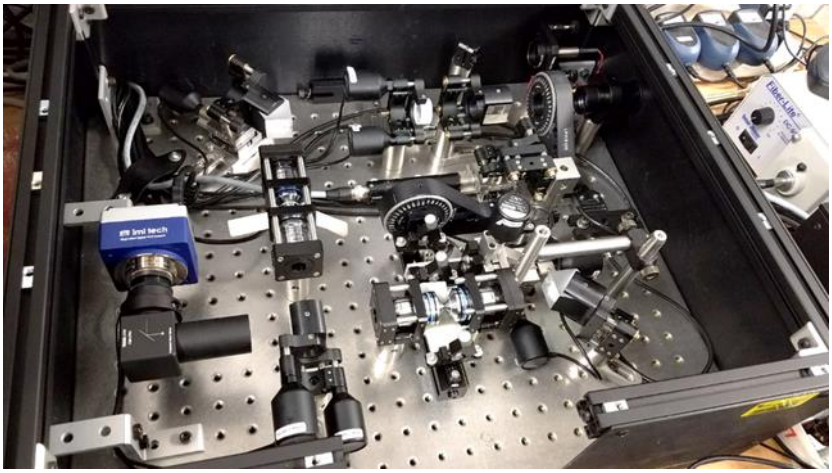

Figure 5.1: Intrafiber IFA-100 profilometer.

One of the major features of the profiler is that the object (i.e. an optical fiber) was rotated directly to record measurements at each illumination angle. This configuration of rotating the sample itself for each perspective, known as the Object Rotation Configuration (ORC) allows the object to be viewed from a full 360° span of angles, as shown in Figure 5.2 (a). Unfortunately, the very act of rotating the object directly naturally perturbs the object and causes it to move between measurements. Since ODT reconstructions assume the object to be stationary over the entire span of angular measurements, additional care had to be taken to correct for the sample's displacement during and between each angular measurement, or else such instability would corrupt reconstructions. For bioimaging applications, the ability to rotate the object directly between measurements may not only become difficult, but the perturbation of the sample may even be deemed unacceptable. Instead, an alternative configuration to ORC is used, called the "Illumination Scanning Configuration" (ISC).

For ISC measurements, the sample is held stationary on a mount (e.g., a microscope slide). Rather than rotating the object for each illumination angle, the illuminating beam is instead

scanned to pass through the sample at a given angle and the diffracted field is holographically recorded on a detector at x=d, as shown in Figure 5.2 (b). By holding the object stationary during the experiment, the stability of the measurement is enhanced. Moreover, the illumination angle is often controlled by a galvanometer mirror, digital micromirror device, or fast scanning mirror, allowing the acquisition time of the ODT dataset to be significantly faster than ORC measurements. A short acquisition time is particularly important for in vivo cellular imaging, where bioprocesses may occur over short timescales [20].

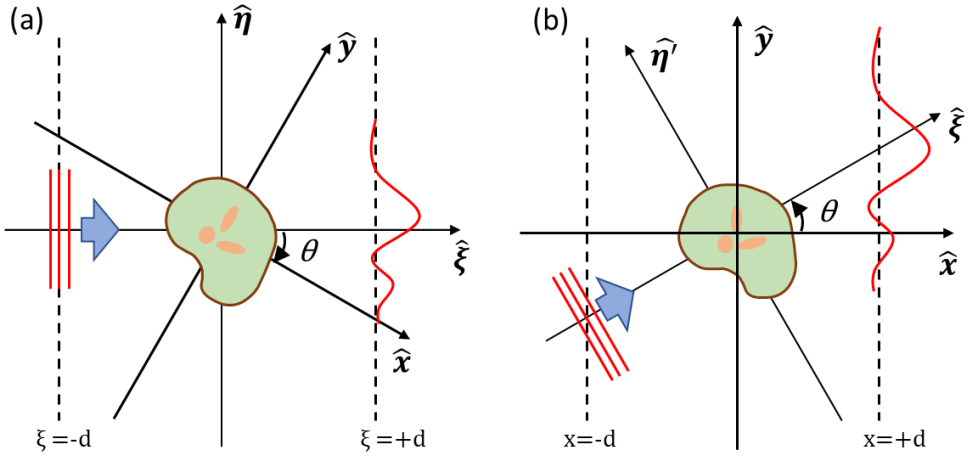

Figure 5.2: Field measurement schematic for (a) object rotated configuration and (b) illumination scanning configuration.

To allow the reconstruction of other classes of objects – in true 3D – I designed and constructed a second experimental setup, shown in Figure 5.3, that acquires data using ISC. The setup consists of a microscope – configured for illumination scanning measurements, followed by a Michelson shearing interferometer used to obtain same-path phase measurements from the microscope. To accommodate white-light holographic measurements (discussed later), we elected to use a same-path measurement approach to generate holograms, as opposed to the MZI design

used in the IFA-100. This decision was primary driven by the difficulty in aligning a MZI setup and balancing the path lengths and dispersion for both arms, which our setup trivializes. This is because the beam is cross-referenced after the microscope's imaging system using an empty Michelson.

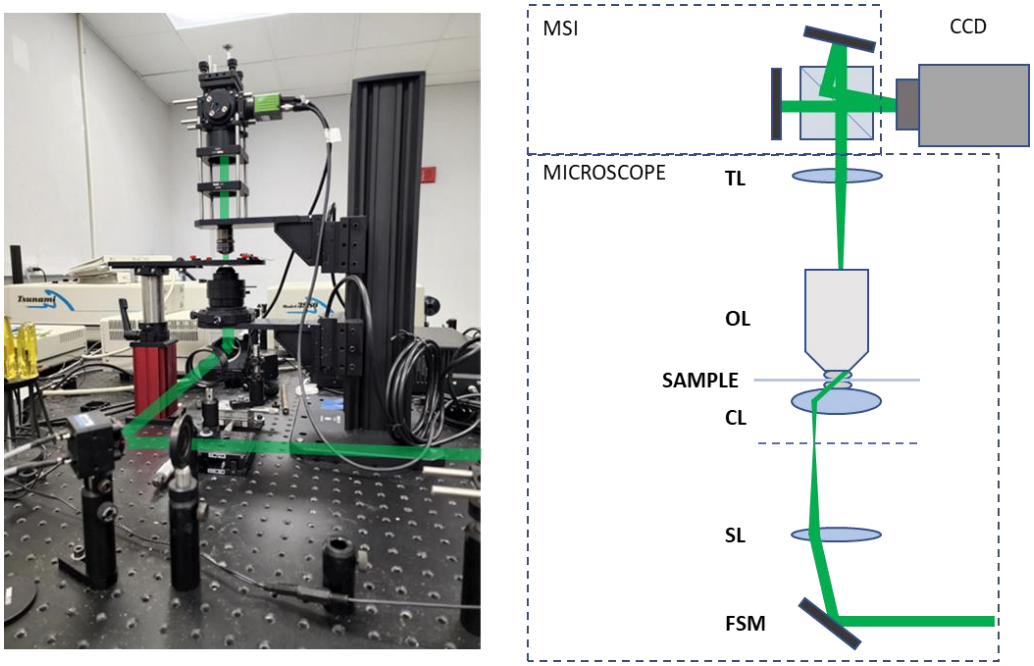

Figure 5.3: (Left) Experimental setup with beam path illustrated. (Right) Conceptual schematic of setup.

To perform ISC measurements, a fast-scanning mirror (FSM) is used to perform beam steering. The angle from the FSM is magnified using a lens system comprised of a scan lens (SL), Thorlabs ACT508-250-A-ML, and a condenser lens (CL), Nikon D-CUO DIC Oil Condenser, 1.4 NA. The resultant diffracted field is then imaged onto a CCD using a U Plan Fluorite 60X Oil Objective lens (OL), NA 1.25-0.65, and a Thorlabs TTL180-A, f=180 mm tube lens (TL).

Between the TL and the detector, a Michelson shearing interferometer (MSI) is positioned to generate a shear hologram, allowing phase measurements of the sample to be acquired using

cross-referenced holographic microscopy (CRHM) [57]. Unlike [57], however, a balanced Michelson (similar to [58]) was chosen used instead of a Sagnac to generate the shear hologram, to ensure the total optical path of the shear interferometer was within the focal length of the TL.

5.2 Numerical Validation of 3D ODT

As alluded to in Section 2.3 and Equation (2.28), the mathematical expansion of ODT framework from 2D to 3D is mostly updating the Green's function from a Hankel function in 2-D to a spherical wave function in 3-D. Unfortunately, numerical considerations are less simple, and numerically efficient propagation algorithms, such as the WA-BPM method [45] are highly desirable. Assuming the use of the WA-BPM algorithm to perform slice-by-slice propagations along "M" slices, the increase in computational complexity for a 2-dimensional $M \times N$ computational area to a 3-dimensional $M \times L \times N$ computational volume is $O(MN\log(N))$ to $O(MLN\log(LN))$, respectively (in addition to significantly larger memory requirements). In the case of the iODT algorithm, efficient propagation is particularly important, because the forward-propagated input field, and the backward-propagated measured field must be calculated throughout the reconstruction volume for every illumination angle. The illumination angles are described by θ and ϕ, as shown in Figure 5.4. The angle θ describes the angle of k_b, measured from the optical axis (denoted as z), while ϕ denotes the azimuthal angle measured in the x-y plane from the x-axis. The θ_{max} in an ISC experiment is limited by the NA of the condenser and objective (whichever is lower), and the RI of the background medium, as given by:

$$\theta_{max} = \sin^{-1}\left(\frac{NA}{n_b}\right). \tag{5.1}$$

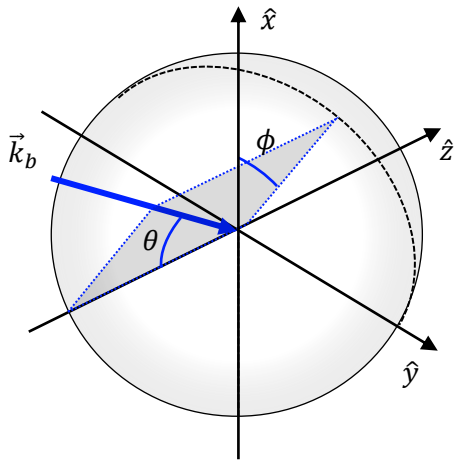

Figure 5.4: Angular representation of illumination angles θ and ϕ, with respect to object assumed to be centered at the origin.

For numerical validation of the 3D R-iODT and phase optimization algorithms, the reconstructive accuracy of each algorithm is quantified using the root-mean-square error (RMSE), for each iteration *m*, between the known object's RI distribution, n_{true}, and the current estimate of the distribution, $n_{est}^{(m)}$. The dummy index j denotes the lexicographically ordered voxel number in the 3D distribution, and N_{vox} is the total number of voxels in the reconstruction volume:

$$RMSD(m) = \sqrt{\frac{1}{N_{vox}} \sum_{n} \left| n_{true,j} - n_{est,j}^{(m)} \right|^2}. \tag{5.2}$$

For experimental validations, the true RI distribution is not known, and so the RMSE error of the measured and simulated sinograms (u_{meas} and u_{est}, respectively) is calculated instead:

$$RMSD(m) = \sqrt{\frac{1}{N_{pix} N_{views}} \sum_{j} \sum_{k} \left| u_{meas,j}^{(k)} - u_{est,j}^{(k)} \right|^2}. \tag{5.3}$$

In the above equation, N_{pix} denotes the number of pixels in each image of the compared sinograms, and N_{views} denotes the number of angular measurements. The dummy indices *j* and *k*

denote the lexicographically ordered pixel number in each image of the sinogram, and the view number, respectively. The simulated sinogram, u_{est}, is the output sinogram generated by the current iteration's estimated distribution, $n_{est}^{(m)}$.

5.2.1 Numerical performance of R-iODT in 3D

To study the reconstructive performance of 3D iODT using different angular coverage, a numerical ORC experiment is devised using noiseless data. The object is illuminated by a plane wave, λ_0 = 0.532 μm. A series of three tests is performed using 'full' angular coverage (i.e., θ_{max}=180°), and two tests of partial angular coverage where θ_{max} is set to 53° and then 35°. For each test, the R-iODT algorithm from Chapter 4 is run for 100 iterations, using a cold initialization (i.e., n_{est} initialized to n_{b}). Figure 5.5 roughly shows the frequency domain coverage of the Limiting Ewald Sphere (LES), if a DFI reconstruction algorithm were to be used, and demonstrates regions of missing information (especially along the k_z axis and $k_z > 0$). As θ_{max} is reduced, the role played by regularization becomes more important as information about the object becomes sparser. Still, the strength of regularization is held constant between the tests, to allow direct comparison between results.

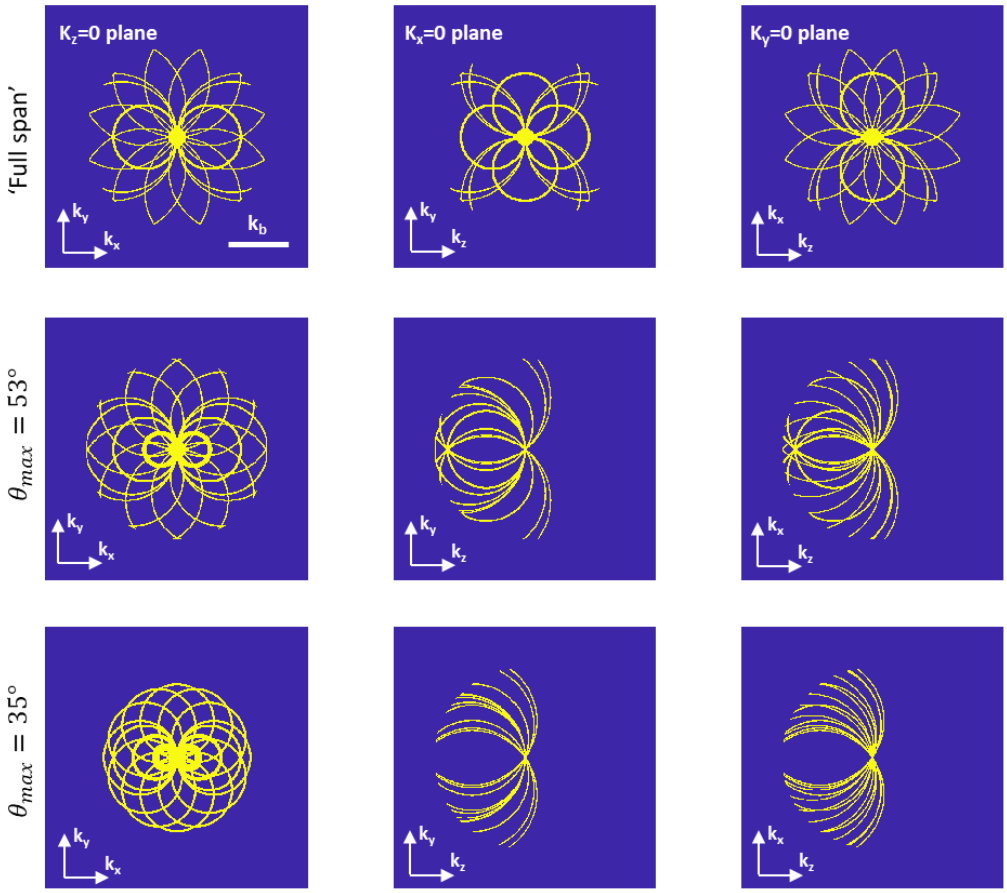

Figure 5.5: LES frequency coverage for each respective test, assuming DFI mapping in the $k_z = 0$, $k_x = 0$, and $k_y = 0$ planes. A bar is added for scale showing the size of k_b.

The phantom in the experiment, shown below in Figure 5.6 (a), consists of 3 spheres of 4 μm diameter, located at (x = 5, y = 0, z = 0 μm), (x = 0, y = 0, z = 0 μm) and (x = 0, y = 0, z = 5 μm). The background RI, n_b, is 1.56, and refractive indices of each sphere is 1.565, 1.57, and 1.58, respectively. For the 'full-angle' test, θ is swept from 0° to 330° in spacing of 30°, with ϕ = 0° (i.e., $\hat{k}_b$ in the y = 0 plane). Another span of angles is measured in the z = 0 plane (i.e., θ = 90°), with ϕ being swept from 30° to 150°, and from 210° to 330° in steps of 15° to provide decently uniform angular coverage. The primary objective of this test is to ensure that each sphere is

reconstructed clearly. The results of this test are shown below in Figure 5.6 (b), and show a clear, accurate reconstruction of each sphere.

For the $\theta_{max} = 53°$ test, the value of θ_{max} represents the best-case angular coverage scenario using the NA from the experimental setup and following Equation (5.1). Unlike data from the experimental setup, ORC numerical data is still used to allow a more comparison to the full coverage reconstruction. For this test, ϕ is swept in a circle ($\theta = 53°$) from 0° to 330° in steps of 30°. An additional line of angles is swept along the x-axis ($\phi = 0°$) from θ = -45° to +45° in steps of 15°. The reconstruction, shown in row (c) of Figure 5.6, is similar to the previous test, though the "missing cone" problem caused by θ_{max} manifests itself as a slight degradation in resolution along the z-axis, which manifests as slight error between objects in the $y = 0$ and $x = 0$ planes.

Although each sphere is resolvable using the previous test's "best case" scenario for θ_{max}, in practice θ_{max} for the experimental setup is limited to ~35° due to a design flaw in the objective lens. For the third test, ϕ is swept along a smaller circle ($\theta = 35°$) from 0° to 330° in steps of 30°. A line of angles is also swept along the x-axis ($\phi = 0°$) from $\theta = -30°$ to +30° in steps of 10°. In this test, the missing angular coverage is substantial, compared to prior tests, as demonstrated in the bottom row of Figure 5.5. The reconstruction shown in Figure 5.6 (d) shows a more substantial drop in resolution along the z-axis, such that the spheres in the $x = 0$ plane are unable to be correctly resolved as separate objects. The third sphere, at $x = 5$ μm is correctly reconstructed because (1) the x and y resolution of the reconstruction is not strongly impacted by the missing angular coverage, and (2), the object is not embedded behind any object that would need to first be reconstructed correctly before the field data at the embedded object can be correctly known. It is

worth noting, however, that for trivially small RI contrasts, assumptions about weakly-scattering objects hold, and issues involving embedded objects become are less significant.

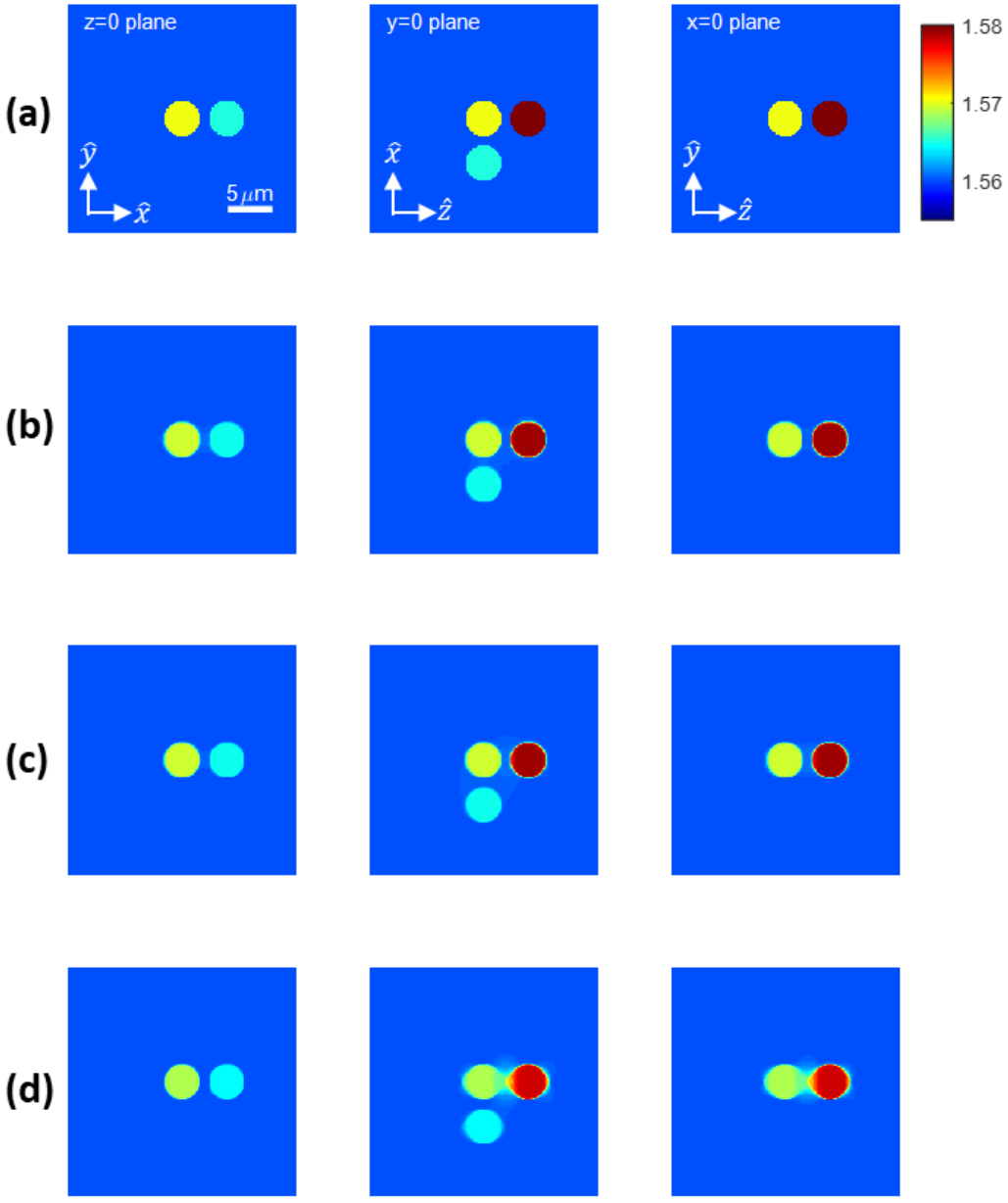

Figure 5.6: Row (a): RI distribution of the true object. Rows (b-d): Respective R-iODT reconstructions after 100 iterations using full angular span, θ_{max} = 53°, and θ_{max} = 35°.

In addition to affecting the overall resolution along the z-axis, the missing-angle problem also causes slower R-iODT convergence as θ_{max} is decreased. To show this effect, the RMSE of the RI reconstruction is plotted for each test in Figure 5.7, as a function of iteration number. The R-iODT algorithm was able to converge to the correct solution for both the 'full angle' test and the θ_{max}=53° test, as evidenced by similar reconstructions in Figure 5.6 (b) and (c), as well as similar RMSE after 100 iterations – though the latter converged slower. In the final test, however, the two spheres in the x = 0 plane failed to fully resolve from each other, presumably due to limited coverage of the LES, as shown in the bottom row of Figure 5.5.

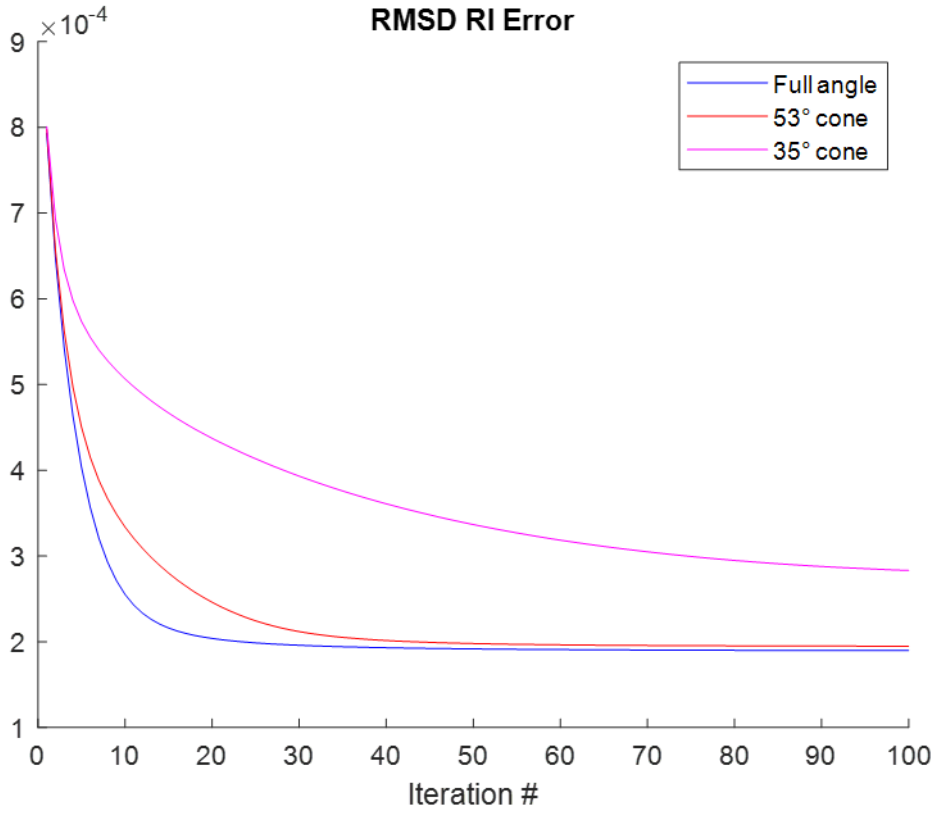

Figure 5.7: RMSE of the RI distribution for each R-iODT test.

5.2.2 Numerical performance of phase-based optimization in 3D

To evaluate the performance of ODT optimization using a phase-based fidelity criterion, the three tests from 5.2.1 are repeated using Algorithm 3.1 to reconstruct the RI. Unlike the R-iODT algorithm, a convex optimization algorithm does not attempt to reconstruct the object at each iteration, but rather gradually converges towards a solution. As in 5.2.1, a cold initialization is used, though Algorithm 3.1 is run for 100 iterations instead of 20 to give the algorithm time to converge. The reconstructions for the 3 optimization tests are shown in Figure 5.8, and a comparison the RMSE of the RI reconstruction at each iteration is shown in Figure 5.9.

For the first two tests, shown in rows (b) and (c) of Figure 5.8, the final reconstructions are mostly consistent with the respective tests from 5.2.1 in rows (b) and (c) of Figure 5.6. The final RMSE for these tests were near 2×10^{-4}, suggesting that both algorithms could find the "global minimum" corresponding to the correct reconstructive solution using either a full span of angles, and using a partial span of angles where $\theta_{max}=53°$ (at the cost of slower convergence).

Unlike the final test of 5.2.1, however, the $\theta_{max}=35°$ reconstruction for phase-based convex optimization converged to a local minimum with a larger RMSE than its R-iODT counterpart, where the two spheres in the $x = 0$ plane are failed to be differentiated as two objects. This implies that the R-iODT algorithm was able to either work past or avoid this local minimum due to its perturbative approach to reconstructing errors in the object.

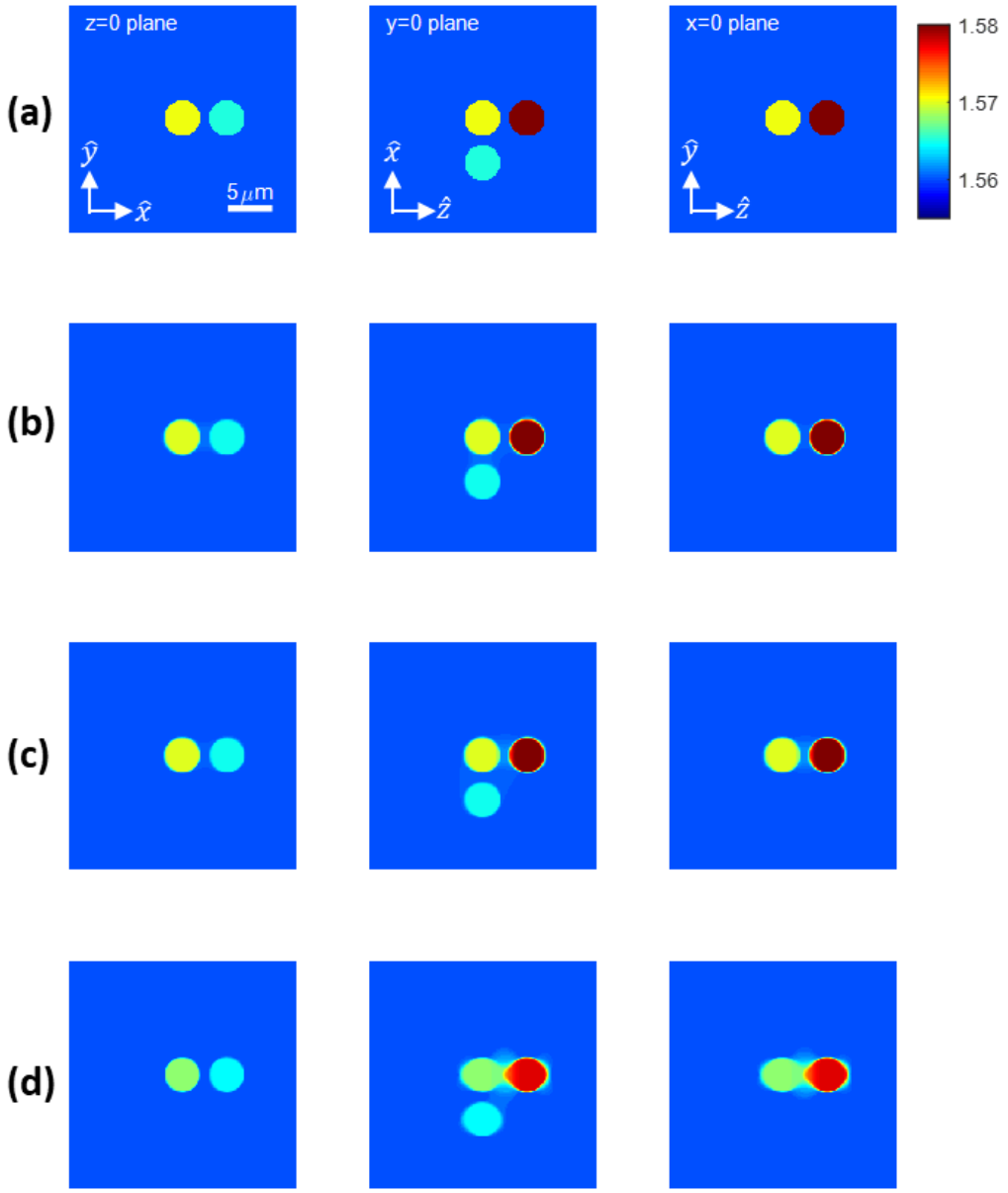

Figure 5.8: Row (a): RI distribution of the true object. Rows (b-d): Respective phase-based optimization reconstructions after 100 iterations using full angular span, θ_{max} = 53°, and θ_{max} = 35°.

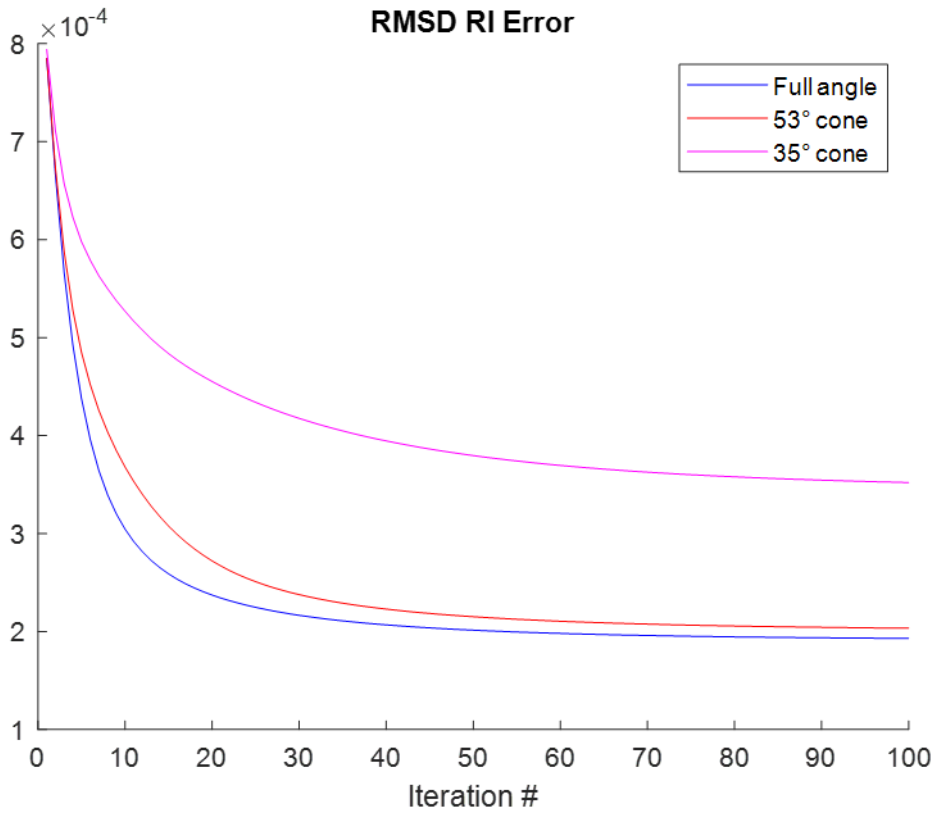

Figure 5.9: RMSE of the RI distribution for each phase-based optimization test.

5.3 ISC to ORC conversion

Although the results from 5.2.1 and 5.2.2 were done using data from ORC propagation models, data collected from the second setup is acquired using illumination scanning. Still, the size of the propagation volume required for 3D ISC forward/backwards propagation is considerably larger than for ORC, as shown in Figure 5.10 (a) and (b). This is because a larger transverse volume (at least along one transverse axis) is necessary to accommodate the ISC propagation in global coordinates, or else the diffracted signal will begin to "walk off" the boundaries of the simulation volume, as shown in Figure 5.10 (a). The larger computational volume for ISC propagation solvers

leads to longer computation times than for ORC models, and thereby lowering the time-efficiency of reconstructions.

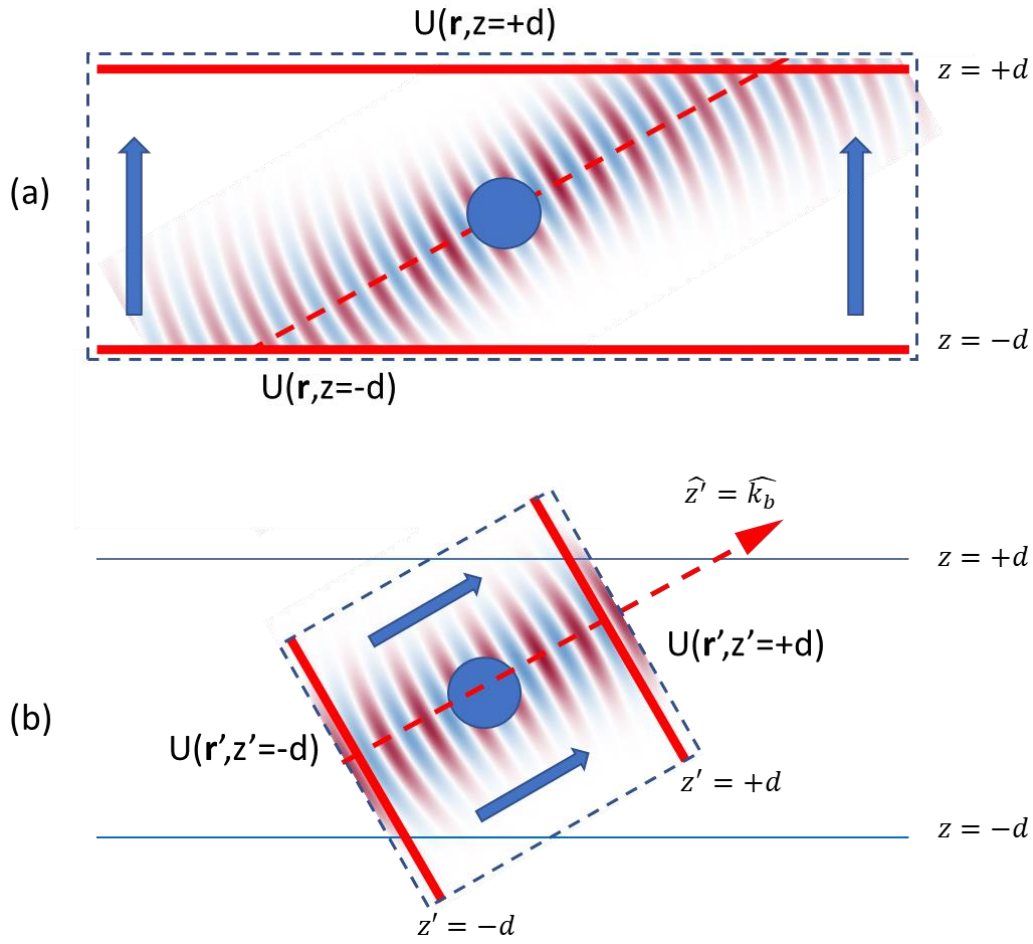

Figure 5.10: Propagation using (a) an ISC framework and (b) ORC framework. A dashed border indicates the approximate necessary boundaries of the simulation volume.

In addition to being potentially slower, ISC propagation may also be potentially less accurate. This is because fields that are propagated at oblique angles are not sampled along the axes of the grid's voxels, where they can be most densely sampled. Furthermore, for multi-slice propagation algorithms such as WA-BPM, the accumulated OPD from the object for each slice is no longer well modelled as a line-integrated phase along the z-direction over the width of the slice.

To work around these issues, I created a method that converts off-axis field data, measured in “global coordinates” from an ISC experiment (see Figure 5.10 (a)), into on-axis fields in “local coordinates” (see Figure 5.10 (b)) that are then compatible with our standard ODT algorithms that assume ORC measurements. By doing so, the required propagation volume is reduced, and the accuracy of the efficient WA-BPM solver is maintained. This three-step process, shown schematically in Figure 5.11, first refocuses a field measured at the plane z=d in global coordinates to a parallel plane at z = 0 in the background medium. Next, the field is propagated from the z = 0 plane to a rotated plane, z'= 0, in local coordinates. Lastly, a standard, on-axis propagation solver (e.g., angular spectrum method) is used to propagate the field in the background medium to the output boundary of the simulation volume, $z' = d$. Since the incident field is normally assumed to be a known planewave travelling along $\widehat{k_b}$, the incident field at the $z' = -d$ boundary is already immediately known.

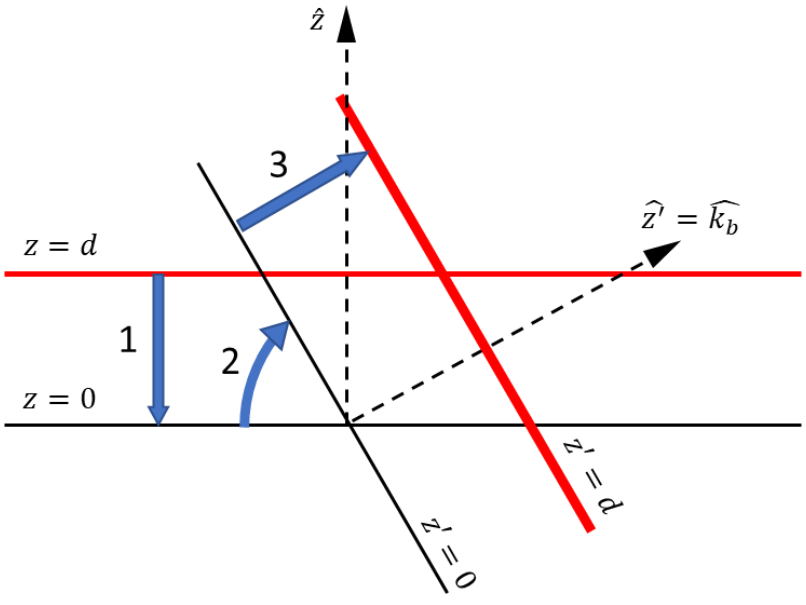

Figure 5.11: Schematic showing propagation steps for converting ISC field measured at $z = d$ plane to ORC field “measured” at $z' = d$ plane.

The measured ISC output field, described in global coordinates as $U(x, y, z = d)$, is refocused (in the background medium) to the z = 0 plane, such that the conversion from the z=0 plane in global coordinates to the $z' = 0$ plane in local coordinates is a simple rotation about their respective origin:

$$\begin{bmatrix} x \\ y \\ z \end{bmatrix} = \hat{R}_{\theta,\phi} \begin{bmatrix} x' \\ y' \\ z' \end{bmatrix}, \tag{5.4}$$

where $\widehat{M}_{\theta,\phi}$is the 3D rotational matrix between the two coordinate systems. The matrix $\hat{R}_{\theta,\phi}$ is orthogonal, and so:

$$\begin{bmatrix} x' \\ y' \\ z' \end{bmatrix} = \hat{R}^{T}_{\theta,\phi} \begin{bmatrix} x \\ y \\ z \end{bmatrix}. \tag{5.5}$$

Next, we follow the steps laid out in [59] for propagating scalar fields (or alternatively in [60] for vector fields) in the background medium from the plane at z=0 to a rotated plane at $z' = 0$. To show this, we start with a field sampled in local coordinates as:

$$U(x', y', z') = U\big(x(x', y', z'), y(x', y', z'), z(x', y', z')\big)$$

$$= \iint \mathrm{d}\nu_x \mathrm{d}\nu_y \; e^{j2\pi[\nu_x x(x', y', z') + \nu_y y(x', y', z') + \nu_z z(x', y', z')]} \widehat{U}\big(\nu_x, \nu_y; 0\big) \tag{5.6}$$

where $\widehat{U}\big(\nu_x, \nu_y\big)$ is the Fourier transform of the field at the plane z=0, $U(x, y, z = 0)$. We now express $\hat{R}_{\theta,\phi}$ from Equation (5.4) in terms of its elements:

$$\hat{R}_{\theta,\phi} = \begin{bmatrix} r_{11} & r_{12} & r_{13} \\ r_{21} & r_{22} & r_{23} \\ r_{31} & r_{32} & r_{33} \end{bmatrix}. \tag{5.7}$$

Equation (5.6) can now be rewritten as:

$$U(x',y',z') = \iint \mathrm{d}\nu_x \mathrm{d}\nu_y \, \widehat{U}(\nu_x,\nu_y) \exp\,(j2\pi[\nu_x(r_{11}x' + r_{12}y' + r_{13}z') + \nu_y(r_{21}x' + r_{22}y' + r_{23}z') + \nu_z(r_{31}x' + r_{32}y' + r_{33}z')]. \quad (5.8)$$

We also relate the spatial frequencies (ν_x,ν_y,ν_z) and (ν_x',ν_y',ν_z') by the rotation matrix:

$$\begin{bmatrix} \nu_x' \\ \nu_y' \\ \nu_z' \end{bmatrix} = \hat{R}_{\theta,\phi}^{T} \begin{bmatrix} \nu_x \\ \nu_y \\ \nu_z \end{bmatrix}. \quad (5.9)$$

Using this relation, Equation (5.8) is now rewritten as:

$$U(x',y',z') = \iint \mathrm{d}\nu_x \mathrm{d}\nu_y \, \widehat{U}(\nu_x,\nu_y) e^{j2\pi[\nu_x'x' + \nu_y'y' + \nu_z'z']}. \quad (5.10)$$

Next, we use a change of variables and express the field at the plane z'=0 as:

$$U(x',y',0) = \iint_C \mathrm{d}\nu_x \mathrm{d}\nu_y \left|\frac{\partial(\nu_x,\nu_y)}{\partial(\nu_x',\nu_y')}\right| \widehat{U}\left(\nu_x(\nu_x',\nu_y'),\nu_y(\nu_x',\nu_y')\right) e^{j2\pi[\nu_x'x' + \nu_y'y']}. \quad (5.11)$$

The domain of *C* covers frequencies where both ν_z and ν_z' are positive. As shown in [59], the Jacobian from Equation (5.11) is simply:

$$\left|\frac{\partial(\nu_x,\nu_y)}{\partial(\nu_x',\nu_y')}\right| = \frac{\nu_z(\nu_x',\nu_y')}{\nu_z'(\nu_x',\nu_y')}. \quad (5.12)$$

For numerical considerations, the Fourier transforms are handled using an FFT algorithm. Because $\widehat{U}(\nu_x,\nu_y)$ is sampled uniformly along ν_x, ν_y, interpolation is required to sample $\widehat{U}\left(\nu_x(\nu_x',\nu_y'),\nu_y(\nu_x',\nu_y')\right)$ onto a uniform grid of ν_x', ν_y', such that an IFFT algorithm can be used to obtain $U(x',y',0)$. The domain of *C* from Equation 5.11 is numerically enforced by applying a Boolean mask in frequency domain.

5.4 Experimental Results

To experimentally validate our 3D frameworks for R-iODT and phase-based optimization, as well the ISC to ORC conversion framework, the ISC experimental setup, shown in Figure 5.3 was used to collect 17 illumination angles within a cone of θ_{max}=35°. For each extracted field form the experiment, an ISC to ORC conversion was performed, as demonstrated in Figure 5.12. Then, I use Algorithm 3.1 to reconstruct the object.

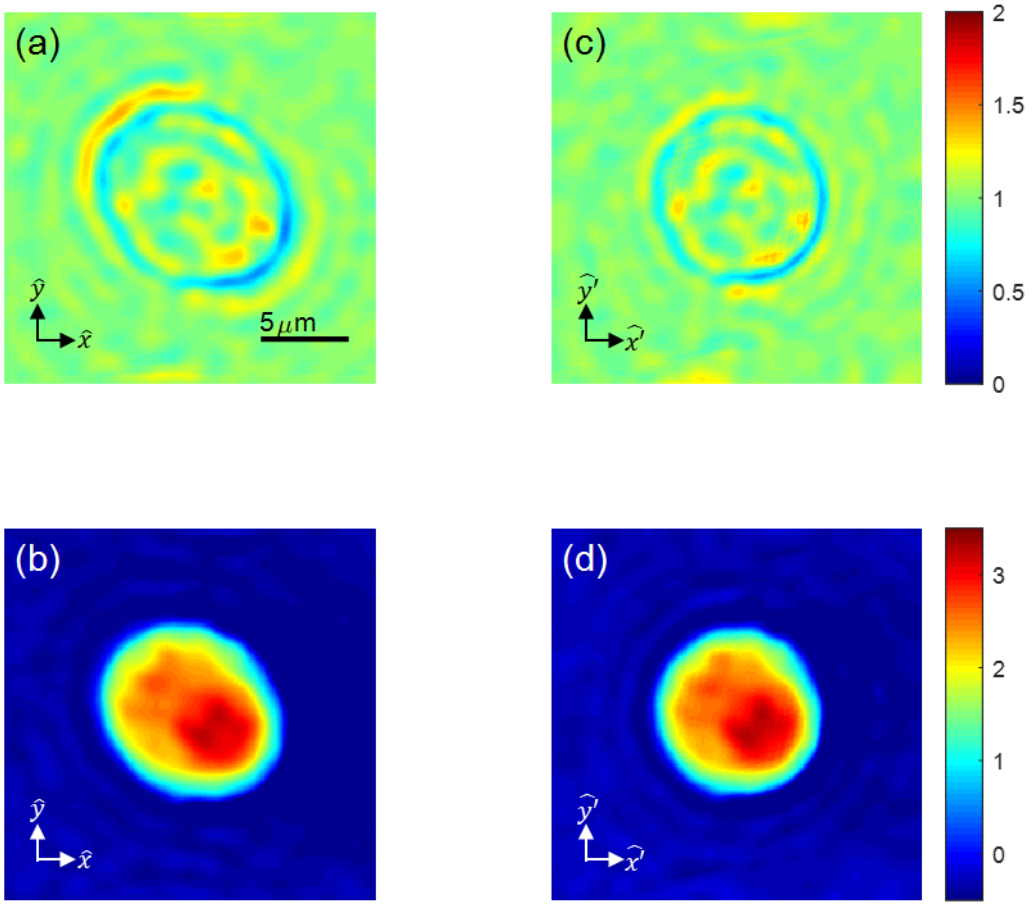

Figure 5.12: (a) and (b): Amplitude and phase, respectively, of a measured ISC field at the plane z = 0 μm in global coordinates. (c) and (d): Amplitude and phase, respectively, of the field after being converted to an ORC "measurement" at the plane $z' = 0$ μm in local coordinates. A bar is added in (a) to show scale.

The object to-be-imaged is taken from a slide of prepared polystyrene beads loaded with a fluorophore that excites and emits in the UV (Sphereotech Fluorescent UV Particle Slide). The average diameter of the spheres is 10.7μm, and the background medium is a fixative whose RI is assumed to be 1.571. To avoid the issue of the object strongly fluorescing, the object is illuminated at 532 nm.

As already implied by the phase of the field shown Figure 5.12, the reconstruction after 100 iterations of Algorithm 3.1 shows that the object tis not a simple polystyrene sphere, but rather a sphere with an asymmetric lobe facing the $+\hat{z}$ direction, shown below in Figure 5.13. A second feature, believed to be a coating is seen clearly as a ring of lower RI in the z=0μm plane (Figure 5.13 (a)) and likely surrounds the entire object. Due to lack of angular coverage, however, the full coating was unable to be reconstructed.

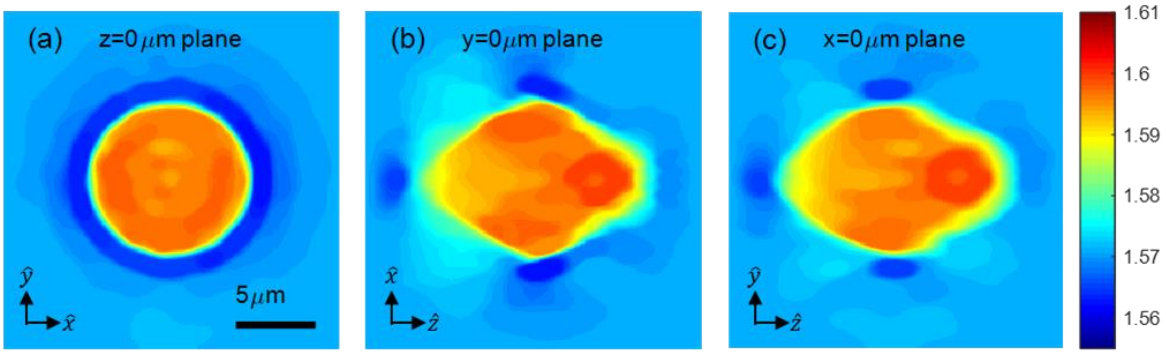

Figure 5.13: Experimental reconstruction of polystyrene bead.

The RMSE of the measured and simulated sinograms, shown in Figure 5.14, suggests that Algorithm 3.1 finished converging after 20 iterations. After this point, minor changes to the estimate of the RI distribution are guided largely by the regularization. Furthermore, unlike the simulated data used in our numerical ODT validations, data from the experiment likely contains

error caused by aberrations in the microscope, speckle from the laser, and small amounts of dust in the microscope's immersion oil. These sources of error vary between each angular measurement, which likely prevents the algorithm from converging further beyond the first 20 iterations. In the case of experimental data that is contaminated with artifacts that cannot easily be modelled, in addition to limited angular measurements, the choice of regularization likely plays a crucial role in the quality of reconstructions. Although our current choice for regularization is based on isotropic TV minimization, more advanced regularization choices exist and are used in the limited angle tomography community [61, 62, 63]. Still, because the measured fields themselves are contaminated with error that cannot be easily modelled, fields that propagated through the correct RI distribution of the sample would likely still differ from their respective fields that are measured in experiment, and so the sinogram's RMSE error should not be expected to converge completely to 0.

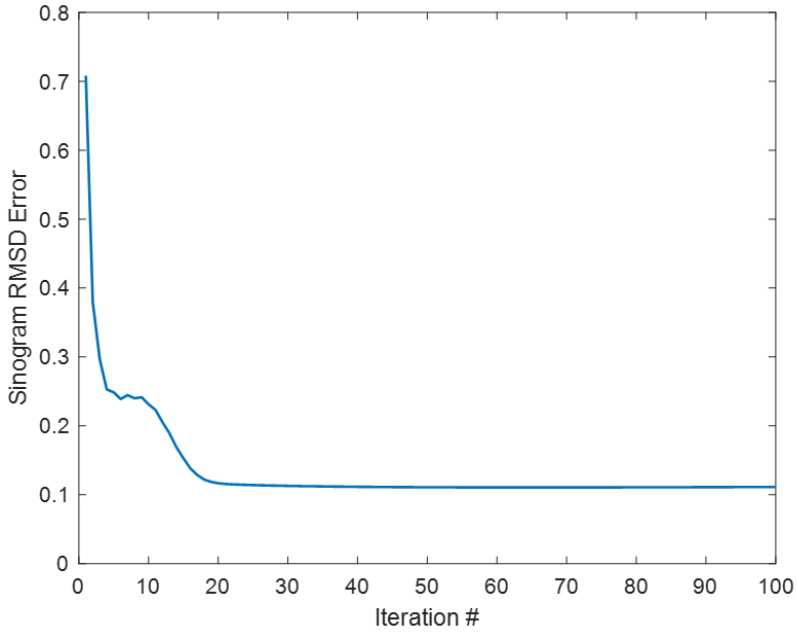

Figure 5.14: RMSE of the simulated output sinogram, using the best guess of the object's RI and the measured sinogram from the experiment.

CHAPTER 6: SPATIOTEMPORAL ODT

An alternative strategy for combating multiple-scattering in turbid media borrows from the principle of ballistic imaging (BI) [64, 65]. As shown below in Figure 6.1, the optical path delay for traversing a turbid object depends on the path taken through it (i.e., the scattering experienced). If a short pulse is sent through an absorbing object that is embedded in a turbid medium, photons arriving first at a detector (placed after the object) would have scattered least, while diffusely scattered photons would arrive last. By time-gating away the multiply-scattered light, a clear silhouette of the absorbing object can be seen on the detector.

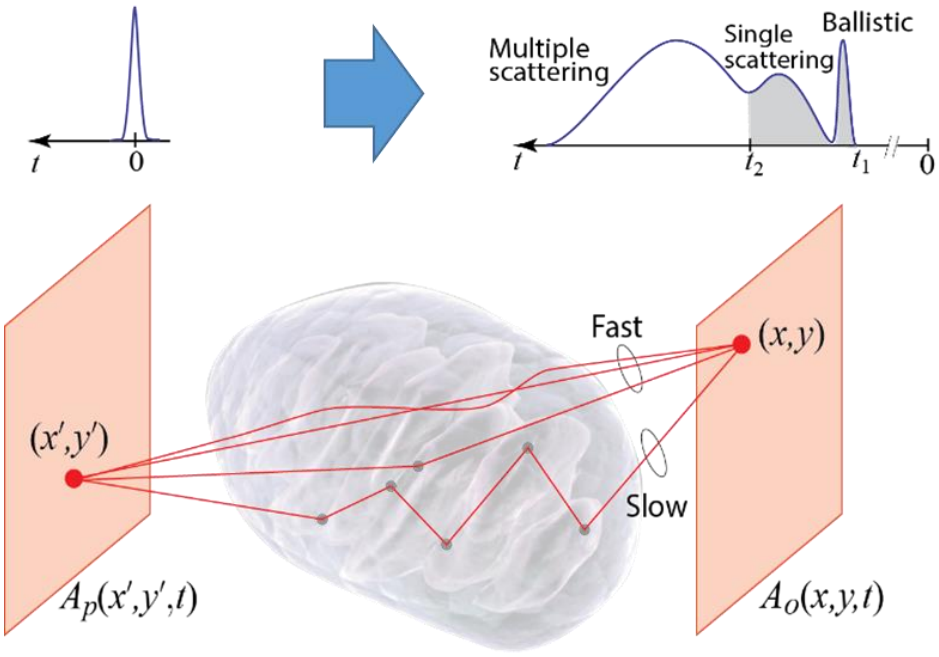

Figure 6.1: Schematic of OPDs for various forms of scattering.

Using the same principle from BI, we may use time-gating to reject higher-order scattering effects from the measured field on the detector, allowing standard ODT inversions to be used, even for objects in turbid media. To achieve this affect, we first illuminate the sample using a short,

plane-wave pulse, and a coherent detector integrates the time-gated response (see Figure 6.1). We call this technique spatiotemporal ODT (ST-ODT) [56].

6.1. Mathematical Formulation of ST-ODT

We now describe a mathematical foundation for ST-ODT. For a linear, shift-invariant system, we take an illuminating field U_i, assumed to be spatially uniform, and its corresponding diffracted field at the detection plane, U_{obj}, and relate them through an impulse response, h_{obj}, as follows:

$$U_{obj}(\vec{r};t) = \iint d^2\overrightarrow{r'}dt' h_{obj}\left(\vec{r};\overrightarrow{r'};t'\right)\cdot U_i(\,t-t'\,). \tag{6.1}$$

At the detection plane, the diffracted field U_{obj} is interfered with a delayed copy of the illumination, $U_i(t-\tau)$. For a slow detector that integrates over time, the following interferogram is sampled, at a fixed distance $r=(x, z=d)$, recorded as the following time average:

$$\begin{aligned} I(\vec{r};\tau) &= < U_i^2 > + < U_{obj}^2 > \; + 2\cdot Re\{< U_{obj}(\vec{r},t)U_i^*(t-\tau) >\} \\ &= < U_i^2 > + < U_{obj}^2 > \; + 2\cdot Re\{C(\vec{r};\tau)\}, \end{aligned} \tag{6.2}$$

where the correlation integral $C(r;\tau)$ is defined as the following time-average:

$$\begin{aligned} C(\vec{r};\tau) &\equiv < \iint d^2\overrightarrow{r'}dt' h_{obj}\left(\vec{r},\overrightarrow{r'};t'\right)U_i(t-t')\,U_i^*(t-\tau) >, \\ &= \iint d^2\overrightarrow{r'}dt' h_{obj}\left(\vec{r},\overrightarrow{r'};t'\right) < U_i(t-t')\,U_i^*(t-\tau) > \end{aligned} \tag{6.3}$$

By defining C_i as the autocorrelation of the illumination field, Equation (6.3) becomes:

$$C(\vec{r};\tau) = \iint d^2\vec{r}'dt' h_{obj}\left(\vec{r},\overrightarrow{r'};t'\right)C_i(\tau-t')\,. \tag{6.4}$$

In order to probe the time-dependence of h_{obj}, we use an illumination for which C_i behaves narrow, with respect to h_{obj}. Recalling that the autocorrelation is given as the time following time average:

$$C_i(\tau - t') \equiv \int_{-\infty}^{+\infty} dt\, U_i(t - t') \cdot U_i^*(t - \tau)\,, \tag{6.5}$$

whose width depends only on the spectral power density of the source. A narrow C_i can be obtained using either a temporally incoherent source (i.e., white-light), or a short pulse, such that:

$$C_i(\tau - t') \approx I_i \delta(\tau - t'). \tag{6.6}$$

At this limit, Equation (6.4) collapses to:

$$C(\vec{r};\tau) = \; I_i \int d^2\vec{r}\,' h_{obj}\left(\vec{r},\overrightarrow{r'};\tau\right). \tag{6.7}$$

6.2. Equivalence to CW ODT

We now compare the result from Equation (6.7) to a result obtained from Equation (6.1) for the case of a monochromatic ($\omega = \omega_o$) plane-wave source:

$$\mathrm{U_{obj}}(x;t) = |U_i| \int d^2\overrightarrow{r'} \int dt' h_{obj}(x,x';t') \cdot \mathrm{e}^{\mathrm{j}\omega_o(\mathrm{t}-\mathrm{t}')}\;, \tag{6.8}$$

which, in turn, is equal to:

$$= |U_i| e^{j\omega_o t} \int d^2\overrightarrow{r'} \int dt' h_{obj}\left(\vec{r},\overrightarrow{r'};t'\right) \cdot \mathrm{e}^{-\mathrm{j}\omega_o t'}$$

$$= \frac{|U_i|}{2\pi} e^{j\omega_o t} \int d^2\overrightarrow{r'}\, H_{obj}\left(\vec{r},\overrightarrow{r'};\omega_o\right). \tag{6.9}$$

We now show that the same information from Equation (5.9) is accessible from Equation (6.8), by numerically integrating Equation (6.7) in software domain as:

$$U_{obj}(\vec{r};t) \propto \int d\tau\, C(\vec{r};\tau) e^{i\omega_o(t-\tau)} = \frac{|U_i|^2}{2\pi} e^{j\omega_o t} \int d^2\overrightarrow{r'}\, H_{obj}\left(\vec{r},\overrightarrow{r'};\omega_o\right). \tag{6.10}$$

Using the approximation from Equation (6.6), we have now established an equivalence between the τ integrated correlation, $C(r;\ \tau)$, from Equation (6.10), and a corresponding CW diffracted field, shown in Equations (6.8) and (6.9). An important difference, however, between these two results is that the field obtained from Equation (6.10) is now accessible to time-gating. We now apply a time-gated integration between times T_1 and T_2, shown in Figure 6.1, and express the time-gated field, $U_{\text{obj,TG}}$, as the following numerically obtained integration:

$$U_{obj,TG}(\vec{r},t) \propto |U_i|^2 e^{j\omega_o t} \int d^2\overrightarrow{r'} \int_{T_1}^{T_2} d\tau\, h_{obj}\left(\vec{r},\overrightarrow{r'};\tau\right) \cdot \mathrm{e}^{-\mathrm{j}\omega_o \tau}. \tag{6.11}$$

The time-gated field is now used in standard, linear ODT inversions as a CW field, where multiple-scattering has been rejected, extending the efficacy of ODT inversions to turbid media.

6.3. Numerical Validation of ST-ODT

To validate ST-ODT [56], we used a numerical forward solver (FDTD) to propagate short pulses through various phantoms. Standard ODT (EDOF-FBPP) reconstructions were performed, using the time-gated field in Equation (6.11), for various choices of T_1 and T_2 in the time-gate (TG), in addition the CW field (no TG used). In the following three examples, an FDTD forward solver was used to measure a diffracted envelope from a 2D object, using a spatial grid size of $\lambda/20$, a background index of 1, λ = 1μm, and a temporally Gaussian, plane-wave pulse of 40 fs duration.

To demonstrate ST-ODT's ability to reconstruct objects embedded in turbid media, we tested the case of a disk, of diameter 10λ and 7% contrast, surrounded by 800 Mie-Rayleigh objects of randomly generated diameter (between λ/10 and λ/4) and position (Figure 6.2). We found that by time-gating, the diffuse Rayleigh background is screened from the reconstruction. This demonstrates that, for simulated turbid media, by multiple-scattering is able to be rejected by time-gating and improve reconstruction quality.

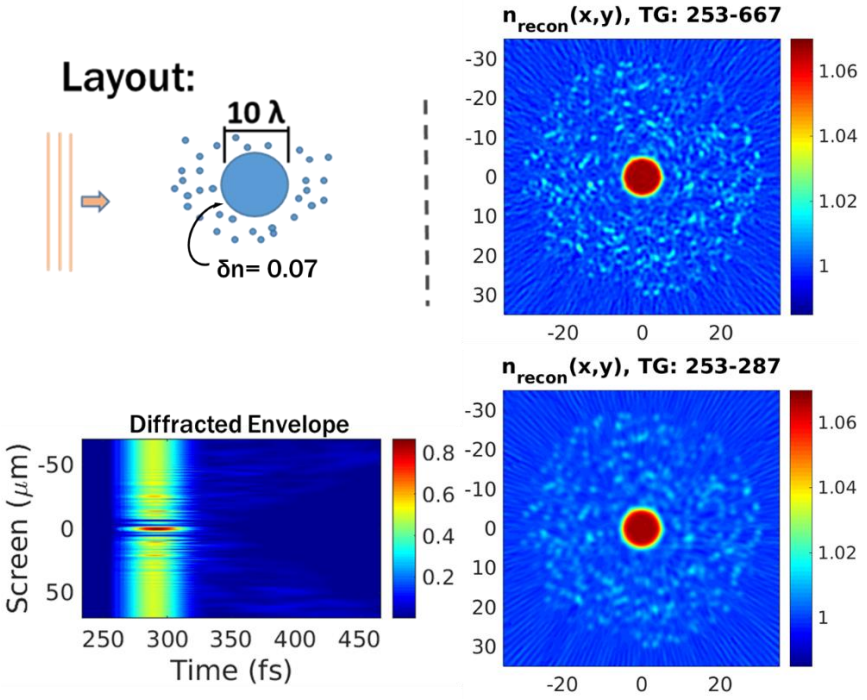

Figure 6.2: Clockwise from top left: Simulation layout, long TG reconstruction (CW), short TG reconstruction, and diffracted pulse envelope, measured vs. time on 1D detector.

In order to test ST-ODT's ability to reject multiple Mie-scattering (particle sizes larger than λ), 19 disks were placed in a 2-layer hexagon configuration (see Figure 6.3). Each disk (diameter 3λ, 9% contrast) is separated by 6λ. Phase vortices, caused by multiple scattering, caused total

reconstruction failure in the CW case. Using an extremely strict TG (T_1 and T_2 both before the peak arrival of pulse), the position and size of the 19 disks are successfully reconstructed.

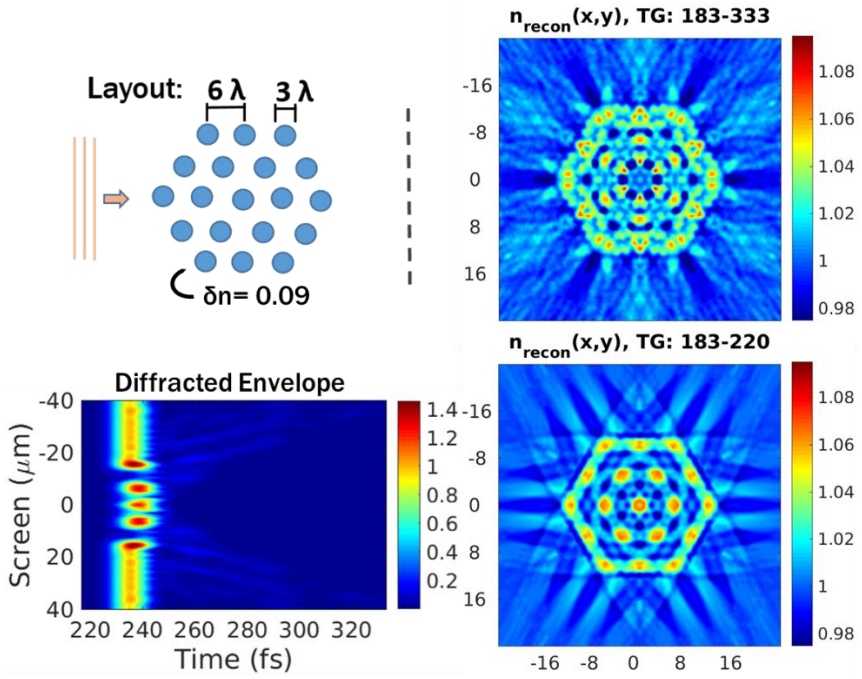

Figure 6.3: Clockwise from top left: Simulation layout, long TG reconstruction (CW), short TG reconstruction, and diffracted pulse envelope, measured vs. time on 1D detector.

In the first example, multiple-scattering was caused primarily by the presence of many Rayleigh objects (small particle diameter). Unlike Mie-scattering, Rayleigh-scattering has a dipolar scattering profile, and so the OPD of its multiple-scattering is larger, with respect to single scattering, due to more back-scattering and larger scattering angles. Mie-scattering, on the other hand, more strongly favors forward scattering. Strong multiple Mie scattering, therefore, has smaller OPD with respect to single-scattered light, while still breaking the linear relationship assumed by the Fourier diffraction theorem. For this reason, ST-ODT is most effective at screening multiple-scattering from *small* particle sizes ($< \lambda/4$).

To test this conclusion, we studied a phantom consisting of two Mie-scattering disks (diameter 10λ, contrast 7%), separated by 15λ. The medium is then peppered by 100 Rayleigh scatterers, similar to the first example. We found after time-gating, reconstruction noise caused by the pepper is screened, while artifact from non-linear Mie-scattering remain (compare reconstruction artifacts between disks in Figure 6.4 to those in the ODT reconstruction of Figure 3.1).

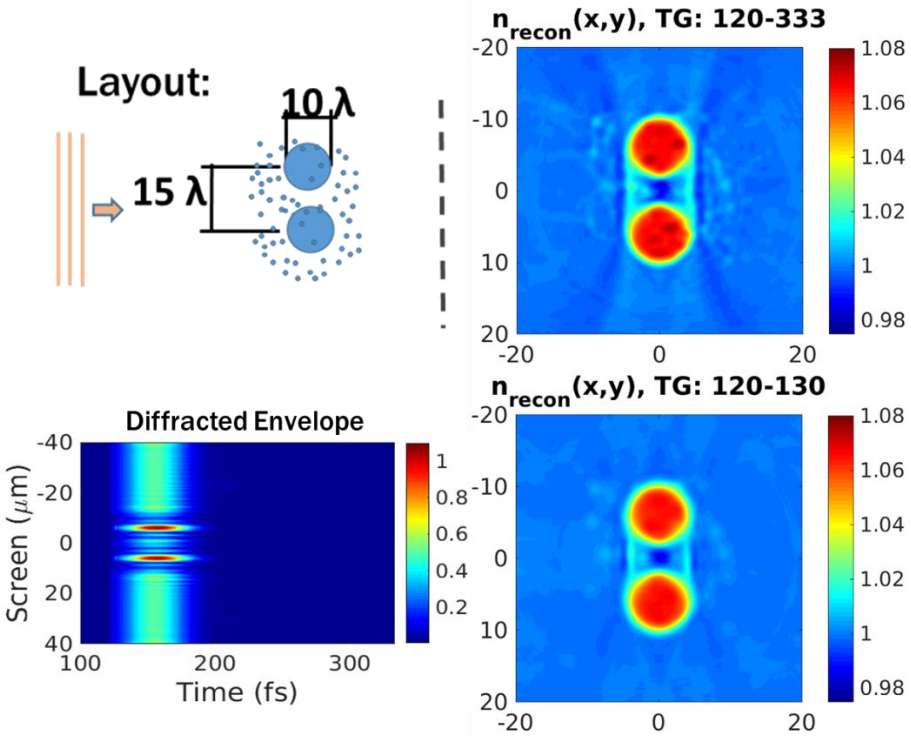

Figure 6.4: Clockwise from top left: Simulation layout, long TG reconstruction (CW), short TG reconstruction, and diffracted pulse envelope, measured vs. time on 1D detector.

6.4. Proposed Method: Time-Resolved Phase Unwrapping in Optical Tomography

While ST-ODT reconstructions are shown to effectively screen multiple-scattering from Rayleigh objects, we found Mie-scattering was difficult to discriminate against – especially in a practical experimental setting. Fortunately, the methods outlined in Chapters 3 and 4 are effective

for handling reconstruction nonlinearities caused by linear Mie-scattering. We are currently exploring the use of time-of-flight information to allow access to the unwrapped phase – which may be difficult when large amounts of scattering are present. By combining this information with iterative solvers (such as iODT, or the algorithm proposed earlier in Chapter 3), expansion to the IODT framework where the *temporal-distribution* of the field, measured on the detector, is used to know the OPD of a sample, before a CW component of the field is then used to reconstruct the object, using the correctly unwrapped phase distribution, thereby alleviating challenges posed by phase-unwrapping in highly scattering media. A preliminary demonstration of this effect was obtained using an optical fiber sample.

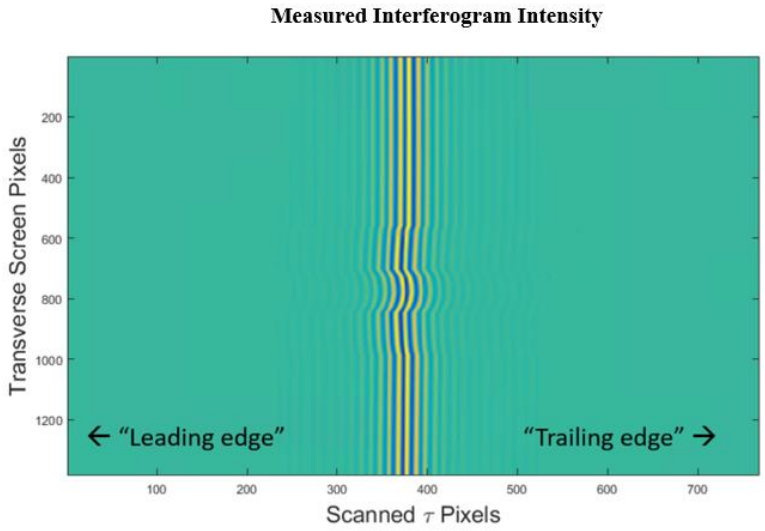

Figure 6.5: Raw interferogram of row of spatial pixels on a CCD detector, at the output of the IFA-100, using an optical fiber sample. Vertical pixels correspond to a row of spatial pixels on the camera, while horizontal pixels correspond to readings at varying differential delays

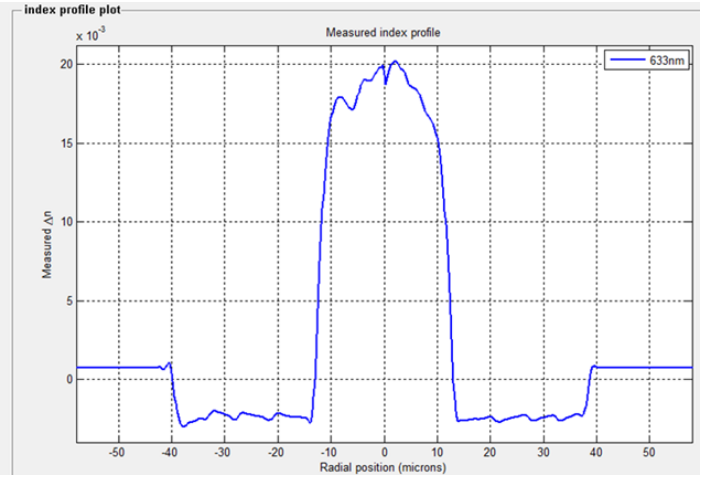

Figure 6.6: Estimated RI cross-section through center of fiber, which directly corresponds to the time-of-flight measurements observed in the temporal distribution shown in Figure 5.5. Pixels in the output temporal response, associated with light that has passed through regions of the fiber of negative RI, with respect to the background (in this case, the cladding) arrive before the "leading edge" of the background signal, while areas of positive RI, and positive OPD trail the background signal.

6.5. Proposed Method: Fourier-Transform ODT

Using the same derivation for Equation (6.7), one finds obtains a second application for measuring the τ-dependent impulse response: 3D Fourier-transform (FT) ODT. Instead of evaluating Equation (6.10) at a fixed frequency ω_o, we measure the CW diffracted field for every frequency ω by taking a Fourier transform of Equation (6.7):

$$U_{obj}(\vec{r};\omega) \propto \frac{1}{2\pi}\int d\tau\, C(\vec{r};\tau)e^{i\omega\tau} = |U_i|^2 \int d^2\overrightarrow{r'}\, H_{obj}\left(\vec{r},\overrightarrow{r'};\omega\right). \qquad (6.12)$$

We may then reconstruct the object function for each ω, using Algorithm 4.1, to obtain the 3D relative permittivity distribution of the object, with frequency. Secondly, we note that the derivations in sections 2.1 and 2.2 make no assumption that this distribution must be real. In this sense, one may use a combination of FT spectroscopy, and ODT to measure the hyperspectral RI and absorption distribution of a sample, in full 3D, at spectral resolution defined by the user. Furthermore, because FT-ODT and ST-ODT rely on the same information to perform

reconstructions, one may explore both applications simultaneously, using the same experimental setup. This technique is already used as a tool for index profiling of optical fibers, using CT reconstructions [66].

ODT and TPM reconstructions are traditionally done using, or assuming, monochromatic illumination. By frequency-sweeping the source (e.g., using a grating), however, and then successively reconstructing the complex RI of the sample at each illumination frequency, both techniques can be used as a tomographic imaging spectroscopy tool, whereby for each spatially resolved pixel (or voxel) in the reconstructed volume, a spectrum of the object's complex-valued RI is known, as a function of wavelength. The spectral and spatial information from the reconstruction can serve to identify materials, as well as provide contextual and functional information about the sample. Unlike imaging spectroscopy methods based solely on absorptive/reflective properties of a material, the ability to also record spectral information of the real part of a material's refractive index provides additional discriminating information of imaged materials, within the spectral window of a detector.

ODT, as a spectroscopic tool, has already been demonstrated in 2016 by Park et al. [67], by sweeping the frequency of the source; however, the paper discussed only the reconstruction of the real part of the RI distribution. Another approach, by Andrew Yablon (2010) [66], combined Fourier transform spectroscopy (FTS) with a CT inversion algorithm, to spatially resolve the real RI distribution of optical fibers, as a function of wavelength. In this paper, we combine FTS with iODT inversions, to reconstruct the complex RI of materials, as a function of wavelength. We call this technique Fourier-transform optical diffraction tomography (FT ODT). FT ODT is

experimentally validated using optical fiber samples, filled with some known liquid, using capillary action.

6.5.1. Experimental validation

For convenience, FT ODT is experimentally validated using hollow core and photonic crystal fiber (HCF and PCF, respectively) samples, assumed to be "2D" objects. The airholes in each sample are filled with absorptive solutions of fluorescent dye (Atto594), dissolved in DMSO at various concentrations. For both fiber designs, solutions of dye, at concentrations of 200 and 700 μm are used. A control sample was prepared, for both fiber designs, in which only DMSO is present. FT ODT is then used to tomographically reconstruct a cross-section of the fiber samples' complex RI, over several wavelengths between 480 and 900 nm. Consequently, a spectrum of the sample's complex RI is recorded for each spatial pixel (or voxel) in the reconstructed volume. Like other FTS techniques, the spectral resolution of FT ODT is inversely proportional to the scanned range of the interferometer's differential delay, while the spectral window of the instrument is typically limited by the detector's sensitivity. The spectral window of the Silicon detector used in this experiment (Imi Tech Mega-pixel Digital CCD Camera) allows for reconstructions between 480 and 900 nm.

We have designed a setup, shown in Figure 6.7, to measurer the interferogram in Equation (6.2), using a white-light source. Currently, a microscopic imaging system is being incorporated into the setup, in order to measure transmitted diffracted fields used in ST-ODT (and FT-ODT) reconstructions.

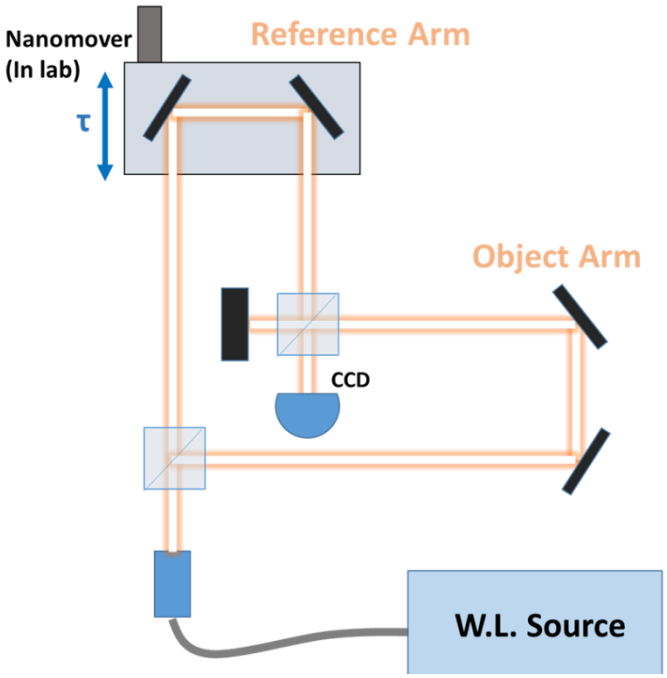

Figure 6.7: Diagram of ST-ODT experimental setup.

While the setup is being constructed, we have obtained experimental ODT data from an Interfiber Analysis IFA-100 instrument, shown below in Figure 6.8.

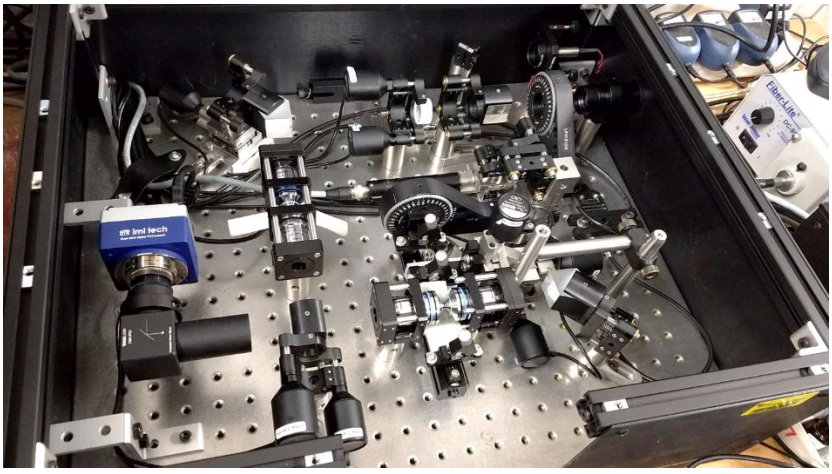

Figure 6.8: Interfiber Analysis IFA-100 fiber index profiler.

While the tool functions well as a tool for acquiring ODT (and IODT) experiments, the tool could not be physically be modified or adapted to accommodate greater delay range, or other magnifications. Moreover, the user is unable to modify software parameters during scans (e.g., noise averaging, sample rotation angular step size, etc.), preventing improvements to the overall quality of the data. Still, we are able to effectively demonstrate a "proof of concept" for FT-ODT.

For our first validation, we took a PCF fiber, whose cores were filled with a non-absorbing liquid, dimethylsulfoxide (DMSO). The cross-section of the fiber is shown in Figure 6.9, while three representative RI dispersion curves are plotted, taken from regions of interest (ROIs) within the reconstruction volume: the background medium, the glass gladding region, and the cores of the PCF. For each frequency, RI values of pixels in these ROIs are averaged together and plotted as points in the plots shown in Figure 6.10.

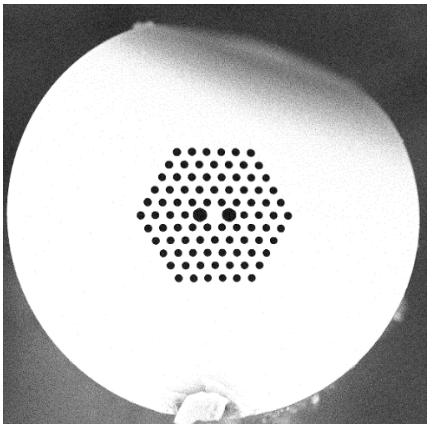

Figure 6.9: SEM of PCF cross-section. During the experiment, PCF cores were filled with DMSO liquid.

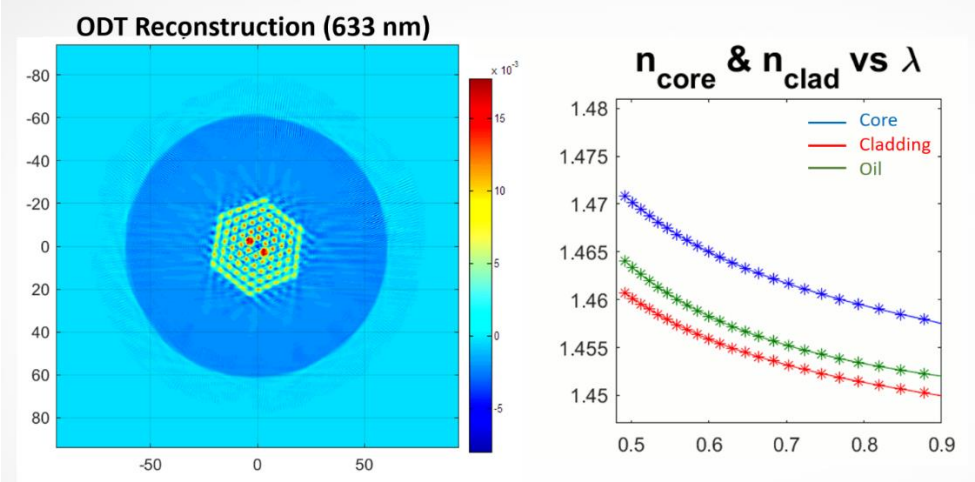

Figure 6.10: (Left) CW reconstruction of PCF at 633 nm. (right) Representative RI plots showing the spectral behavior of three ROI regions: fiber cores (filled with DMSO), glass fiber cladding, and background medium (RI matching oil).

For our second validation, we took an HCF (SEM shown in Figure 6.11), and filled it with DMSO, containing varying concentrations of dissolved fluorescent dye (Atto 594). The absorption spectra of the DMSO liquid, and 200 μM solution were independently measured using a spectrometer, as shown in Figure 6.12; however, because the 700μM concentration of the dye caused substantial attenuation that saturated the spectrometer and prevented accurate measurement.

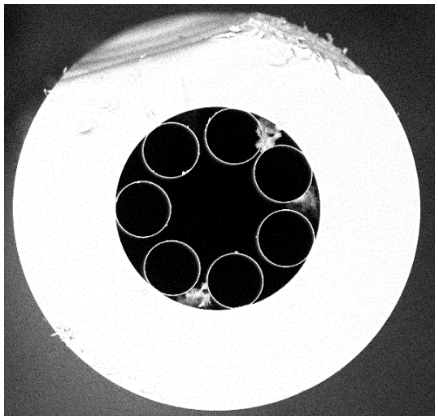

Figure 6.11: SEM image of HCF cross-section.

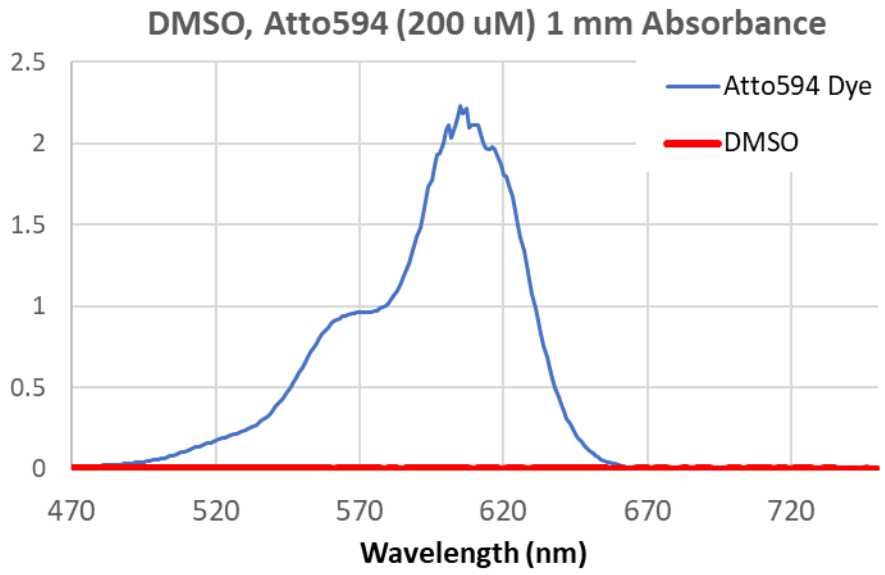

Figure 6.12: Measured absorption spectrum of DMSO/dye solution at 200 μM concentration, as well as for a pure DMSO (no dye present).

Since ODT reconstructions allow the reconstruction of both real and imaginary parts of the RI (i.e. n and κ), we were able to reconstruct a hyperspectral cube containing the spatial distribution of the complex-valued RI of the fiber, over a range of frequencies between 400 and 900 nm. We were successfully obtained a spatial distribution of the complex RI, as well as representative n and κ spectra, for various regions of the reconstruction volume. As shown in Figure 6.13, we not only show that κ of the dye (found only in the liquid core region) is larger at the expected absorption feature near 615 nm, while the spectral distribution of the RI in the liquid core exhibits a kink in the real part of the RI that is associated with the Kramers–Kronig relationship. As the Beer-Lambert law suggests, the absorption coefficient of the liquid should vary linearly with the concentration of the absorbing dye in the DMSO material. As we see in Figure 6.13, the size of the peak values of κ seems to scale linearly with concentration, which follows this expectation.

We hope to further demonstrate these relationships using more samples and concentrations in the future.

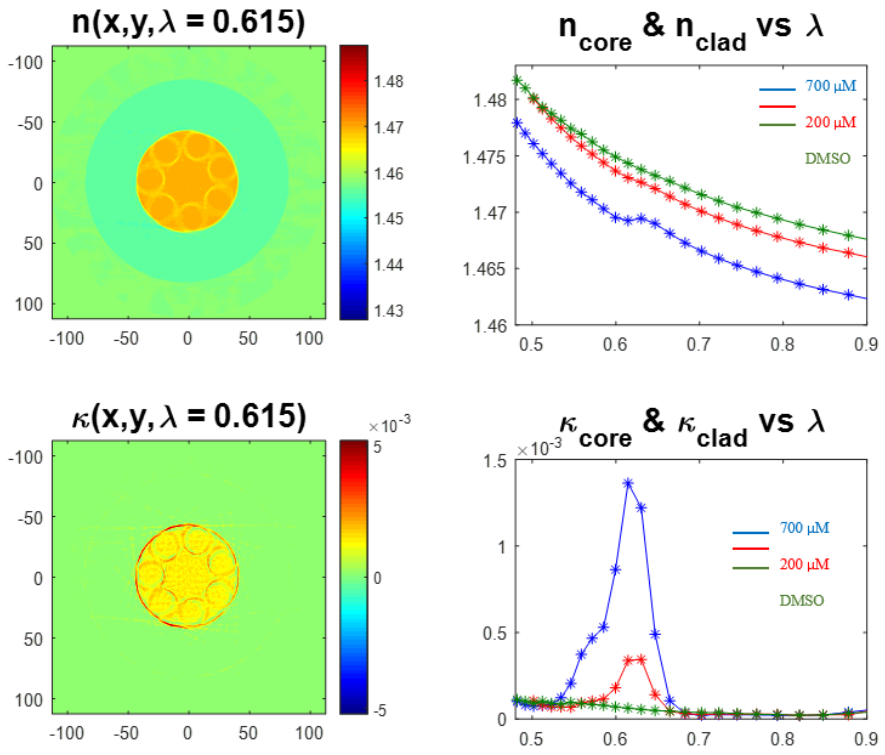

Figure 6.13: (Top and bottom left) Spatial reconstructions of n and κ, respectively, at 615 nm. (Top and bottom right) Respective plots of the core region for n and κ, for 200 and 700 μM concentrations of dye, as well as for pure DMSO.

6.5.2 FTS measurements with updated setup

Currently, the ISC ODT setup is used to perform CW reconstructions. By placing a Michelson interferometer *before* the microscope tower shown in Figure 5.3, however, the illumination can be modulated such that the microscope can be converted into a Fourier-transform spectral phase imaging system, as shown in Figure 6.14.

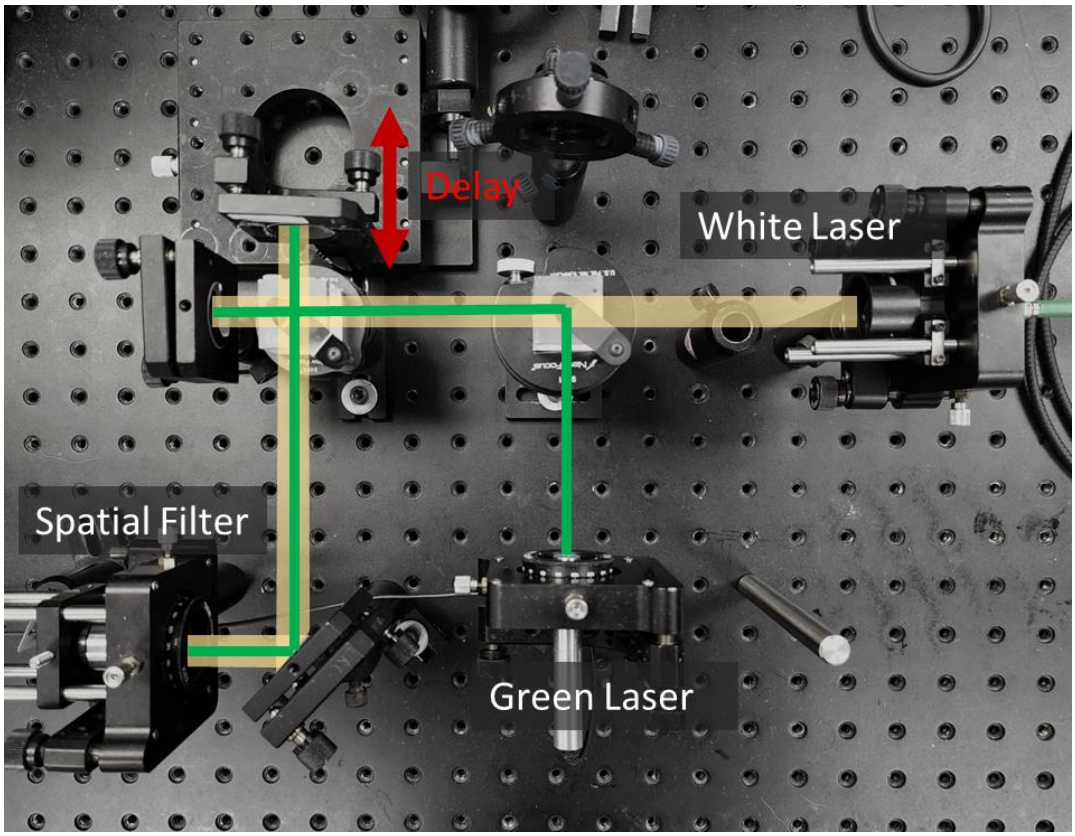

Figure 6.14: Michelson interferometer for FTS measurements preceding ODT setup in Figure 5.3.

Although the ISC setup has yet to be used to reconstruct a sample's RI at each frequency (as experimentally performed before on the IFA-100), the Michelson itself allows FTS measurements to practically arbitrary spectral resolution – up to theoretically sub-Angstrom, as allowed by the span of the Michelson's differential delay arm. In practice, the spectral resolution can be selected based on the needs of the current sample. For example, if the refractive-index varies somewhat slowly throughout the visible spectrum, less spectral resolution is necessary. On the other hand, if a Mid-infrared camera were used to look at the spectrum of a polymer sample, a much higher spectral resolution would be necessitated, as the absorption spectrum (and RI by extension) contains much more features.

A preliminary FTS test has been performed using the Michelson attachment to the microscope to measure the spectra of a 532 nm (green) laser source, a white-light supercontinuum source, the superposition of both sources, and lastly the spectrum of a supercontinuum source passed through a 10 nm bandpass filter at 650 nm. The differential delay was scanned over a 40μm range for this experiment, corresponding to a spectral resolution of approximately 6nm. The results, shown in Figure 6.15 show the laser's spectrum to be a "delta-function" at 564 THz (or 532 nm), while the supercontinuum appears to be a broad peak across the visible spectrum. Although the true spectrum of the supercontinuum spans a much larger bandwidth, the observed spectrum is bottlenecked by the spectral sensitivity of the detector (i.e., camera). As expected, the spectrum when both lasers are used simultaneously is a linear superposition of their respective spectra. Finally, a test was performed where the combined illumination was passed through a 10nm bandpass filter at 650 nm, yielding a narrow spectral peak corresponding to the filter's transmission spectrum. In reality, the spectrum of the laser in the first column of 6.15 is much narrower than the transmission spectrum of the bandpass filter (shown in the fourth column). To show this, higher spectral resolution would be needed (done by spanning a wider range of differential delay in the Michelson in Figure 6.14).

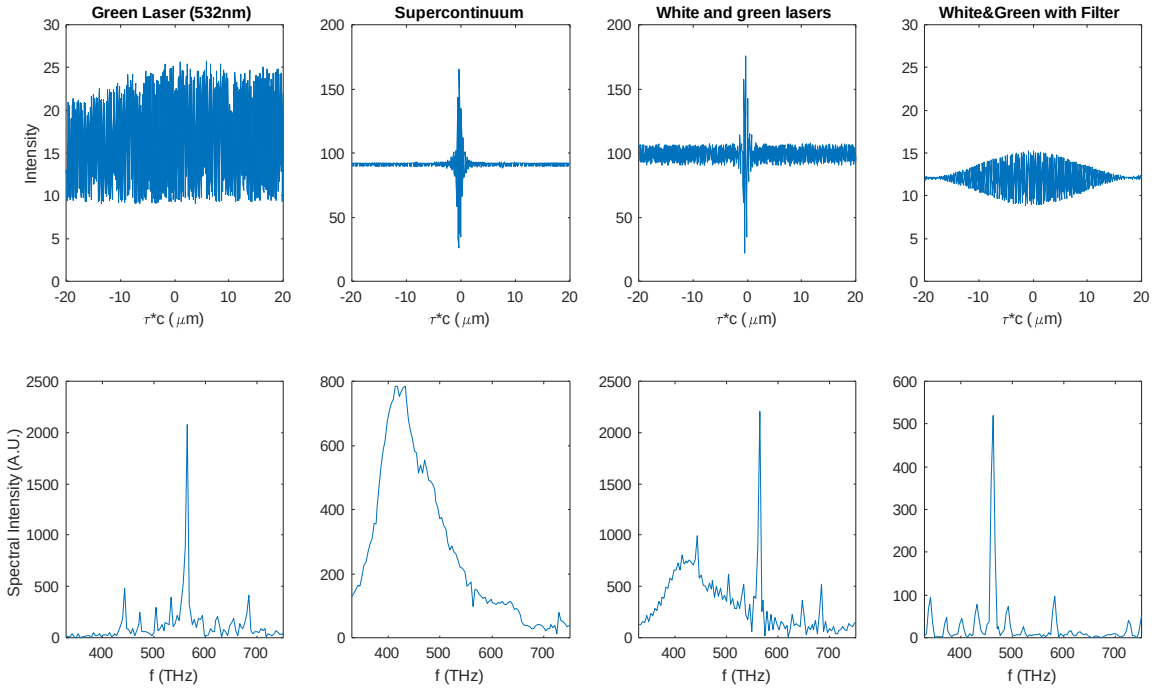

Figure 6.15: Holographic measurements and respective spectra using different illumination sources.

Because 3D ODT reconstructions are somewhat resource intensive, the process of performing FT-ODT measurements for 3D objects relies on (1) obtaining an ODT reconstruction at a single frequency, and then (2) using that reconstruction as an initial guess for the reconstructed RI at a neighboring frequency. This process is repeated until a reconstruction is obtained for each desired frequency in the spectrum. By doing so, we remove unnecessary iterations spent on reconstructing the overall shape of the object, but rather only update the value of the RI at each region of the object. In the future, a constraint may be developed that enforces knowledge that the shape of the object cannot change significantly with illumination wavelength, but rather only values within the shape. This is because the object is stationary and unaltered between all illumination frequencies.

CHAPTER 6: CONCLUSION

Optical diffraction tomography is a powerful tool for quantitative 3-dimensional refractive index imaging. While linear inversions are popular, their validity is somewhat limited to simple, weakly-scattering phase objects. To reconstruct more complicated objects, or objects with larger OPD, iterative perturbative and optimization-based approaches have been developed. This dissertation has introduced techniques that expand the reconstructive efficacy of ODT using iterative and regularized optimization tools. Additionally, the utility of ODT as a quantitative phase imaging method has been expanded to include spectral imaging.

I have demonstrated the shortcomings of field-based optimization in ODT, as the relationship between the object's distribution and the phase of its diffracted field is surjective, but not injective. This allows multiple reconstruction distributions to exist that yield highly similar diffracted output fields to the ones measured, causing convex optimization methods to become trapped in deep local minima if the algorithms are not initialized sufficiently close to the global minimum. I introduced a new method that uses convex optimization to instead minimize a fidelity criterion based on unwrapped output phase, allowing the algorithm to approach the correct solution.

Because iterative ODT (iODT) seeks to fully reconstruct an object at each iteration, it is typically more efficient than optimization methods at obtaining a solution; however, the Rytov-based algorithm is susceptible to artifacts caused by phase singularities. I introduced a second method that combined TV regularization – used in our optimization methods – with the efficient perturbative framework of iODT, allowing both efficient and accurate reconstructions of the refractive index.

I have designed and built a new ODT experimental setup that uses illumination scanning to obtain ODT data. In order to use the new algorithms for reconstruction based on data taken with the setup, I expanded the ODT frameworks from 2D to 3D, and validated each numerically and experimentally. To increase the numerical performance of reconstruction, I created a method that converts ISC data from the experiment into ORC data, that can be propagated in smaller simulation volumes with efficient solvers such as WA-BPM.

Lastly, I have demonstrated the utility of using temporally incoherent illumination in ODT applications. Because multiply-scattered light arrives later than the ballistic and weakly-scattered signal, I have shown that temporally incoherent illumination can be used to discriminate against the multiply-scattered signal and reject its associated artifacts that appear in linear ODT reconstructions. I have demonstrated an alternative application of using Fourier-transform spectroscopy on the temporally-incoherent signal to separate the measured white-light hologram data into many CW holographic components. Because ODT models typically assume CW illumination, ODT data at each CW illumination frequency component can be used to reconstruct the object's refractive index at that frequency. ODT reconstructions are performed at every frequency in the measured bandwidth of the source. Thus, a 3D distribution of the object's complex-valued refractive index can be obtained, and for every voxel in the distribution, the spectral dependence of the refractive index can be estimated. This allows ODT to be used as a powerful characterization technique for analyzing the linear optical properties of materials.

The experimental setup I built will serve as a platform for performing Fourier-transform ODT measurements at a much greater spectral resolution than obtained using the IFA-100 instrument. To help this process, I have recently explored the efficiency and utility of various on

and off-axis propagation frameworks for ISC and ORC ODT reconstructions to allow efficient estimation of large spatio-spectral datasets. Such study should be invaluable for processing large datasets on standard desktop computers. I intend to conduct future studies of the use of temporally incoherent illumination to allow time-of-flight measurements for validating ST-ODT. Another area of exploration in future research may be the integration of spatially incoherent illumination with ODT models in order to reject higher orders of scattering from measured data, while preserving the spatial resolution allowed by ODT measurements.

LIST OF REFERENCES

[1] "Optical Imaging," National Institute of Biomedical Imaging and Bioengineering, 17 July 2018. [Online]. Available: https://www.nibib.nih.gov/science-education/science-topics/optical-imaging. [Accessed 8 June 2022].

[2] M. J. Sanderson, I. Smith, I. Parker and M. D. Bootman, "Fluorescence Microscopy," *Cold Spring Harbor protocols,* vol. 10, 2014.

[3] K. Licha, "Contrast Agents for Optical Imaging," in *Contrast Agents II. Topics in Current Chemistry,* Springer, 2002.

[4] M. C. Pierce, D. J. Javier and R. Richards-Kortum, "Optical contrast agents and imaging systems for detection and diagnosis of cancer," *International Journal of Cancer,* vol. 123, no. 9, pp. 1979-1990, 2008.

[5] J. V. Frangioni, "In vivo near-infrared fluorescence imaging," *Current Opinion in Chemical Biology,* vol. 7, no. 5, pp. 626-634, 2003.

[6] J. Rao, A. Dragulescu-Andrasi and H. Yao, "Fluorescence imaging in vivo: recent advances," *Current Opinion in Biotechnology,* vol. 18, no. 1, pp. 17-25, 2007.

[7] M. Trusiak, M. Cywinska, V. Mico, J. A. Picazo-Bueno, C. Zuo, P. Zdankowski and K. Patorski, "Variational Hilbert quantitative phase imaging," *Scientific Reports,* vol. 10, no. 13955, 2020.

[8] Y. K. Park, C. Depeursinge and G. Popescu, "Quantitative phase imaging in biomedicine," *Nature Photonics,* vol. 12, pp. 578-589, 2018.

[9] G. Popescu, Quantitative Phase Imaging of Cells and Tissues, New York: McGraw-Hill, 2011.

[10] S. K. Debnath and Y. K. Park, "Real-time quantitative phase imaging with a spatial phase-shifting algorithm," *Optics Letters*, vol. 36, no. 23, pp. 4677-4679, 2011.

[11] L. Tian, X. Li, K. Ramchandran and L. Waller, "Multiplexed coded illumination for Fourier Ptychography with an LED array microscope," *Biomedical Optics Express*, vol. 5, no. 7, pp. 2376-2389, 2014.

[12] W. Choi, C. Fang-Yen, K. Badizadegan, K. Oh, S. Lue, R. R. Dasari and M. S. Fiel, "Tomographic phase microscopy," *Nature Methods*, vol. 4, no. 9, pp. 717-719, 2007.

[13] A. Kus, M. Dudek, B. Kemper, M. Kujawinska and A. Vollmer, "Tomographic phase microscopy of living three-dimensional cell cultures," *Journal of Biomedical Optics*, vol. 19, no. 4, 2014.

[14] D. Jin, R. Zhou, Z. Yaqoob and P. T. C. So, "Tomographic phase microscopy: principles and applications in bioimaging [Invited]," *Journal of the Optical Society of America B*, vol. 34, no. 5, pp. B64-B77, 2017.

[15] T. M. Buzug, "Computed Tomography," in *Springer Handbook of Medical Technology*, Springer, 2011, pp. 311-342.

[16] B. E. Saleh, Introduction to subsurface imaging, Cambridge: Cambridge University Press, 2011.

[17] D. Huang, E. A. Swanson, C. P. Lin, J. S. Schuman, W. G. Stinson, W. Chang, M. R. Hee, T. Flotte, K. Gregory, C. A. Puliafito and J. G. Fujimoto, "Optical coherence tomography," *Science*, vol. 254, no. 5035, pp. 1178-1181, 1991.

[18] D. A. Boas, D. H. Brooks, E. L. Miller, C. A. DiMarzio, M. Kilmer, R. J. Gaudette and Q. Zhang, "Imaging the body with diffuse optical tomography," *IEEE Signal Processing Magazine*, vol. 18, no. 6, pp. 57-75, 2001.

[19] M. Born and E. Wolf, Principles of Optics, 7th Ed., Cambridge: Cambridge University Press, 1999.

[20] Y. Sung, W. Choi, C. Fang-Yen, K. Badizadegan, R. R. Dasari and M. S. Feld, "Optical diffraction tomography for high resolution live cell imaging," *Opt. Express*, vol. 17, pp. 266-277, 2009.

[21] P. Muller, "Optical diffraction tomography for single cells," Biotechnology Center (Dresden University of Technology), Dresden, 2016.

[22] S. Fan, S. Smith-Dryden, J. Zhao, S. Gausmann, A. Schulzgen, G. Li and B. E. A. Saleh, "Optical fiber refractive index profiling by iterative optical diffraction tomography," *Journal of Lightwave Technology*, vol. 36, no. 24, pp. 5754-5763, 2018.

[23] M. Born, "Quantenmechanik der Stoßvorgänge," *Z. Physik*, vol. 38, pp. 803-827, 1926.

[24] B. Chen and J. J. Stamnes, "Validity of diffraction tomography based on the first Born and the first Rytov approximations," *Appl. Opt.*, vol. 37, pp. 2996-3006, 1998.

[25] P. Muller, M. Schurmann and J. Guck, "The Theory of Diffraction Tomography," 2016.

[26] K. Watanabe, Integral Transform Techniques for Green's Function, Switzerland: Springer International Publishing, 2015.

[27] A. Erdelyi, Tables of Integral Transforms, Vol 1, London: McGraw-Hill Book Company, Inc., 1954.

[28] A. J. Devaney, "A filtered backpropagation algorithm for diffraction tomography," *Ultrasonic Imaging,* vol. 4, no. 4, pp. 336-350, 1982.

[29] J. Kostencka, T. Kozacki, M. Dudek and M. Kujawinska, "Noise suppressed optical diffraction tomography with autofocus correction," *Opt. Express,* vol. 22, pp. 5731-5745, 2014.

[30] J. Kostencka and T. Kozacki, "Computational and experimental study on accuracy of off-axis reconstructions in optical diffraction tomography," *OPTICE,* vol. 54, 2015.

[31] U. S. Kamilov, I. N. Papadopoulos, M. H. Shoreh, A. Goy, C. Vonesch, M. Unser and D. Psaltis, "Optical tomographic image reconstruction based on beam propagation and sparse regularization," *IEEE Transactions on Computational IMaging,* vol. 2, no. 1, pp. 59-70, 2016.

[32] H. Harada, D. J. N. Wall, T. Takenaka and M. Tanaka, "Conjugate gradient method applied to inverse scattering problem," *IEEE Transactions on Antennas and Propagation,* vol. 43, no. 8, pp. 784-792, 1995.

[33] S. Smith-Dryden, S. Fan, B. E. A. Saleh and G. Li, "Optical diffraction tomography by use of optimization and phase-based fidelity criterion," *IEEE Journal of Selected Topics in Quantum Electronics*, vol. 27, no. 4, pp. 1-9, 2021.

[34] W. Gorski and W. Osten, "Tomographic imaging of photonic crystal fibers," *Opt. Lett.*, vol. 32, pp. 1977-1979, 2007.

[35] E. Wolf, "Three-dimensional structure determination of semi-transparent objects from holographic data," *Optics Communications*, vol. 1, no. 4, pp. 153-156, 1969.

[36] S. Shin, D. Kim, K. Kim and Y. Park, "Super-resolution three-dimensional fluorescence and optical diffraction tomography of live cells using structured illumination generated by a digital micromirror device," *Sci. Rep.*, vol. 8, no. 9183, 2018.

[37] A. J. Devaney, "Inverse-scattering theory within the Rytov approximation," *Opt. Lett.*, vol. 6, no. 8, pp. 374-376, 1981.

[38] W. C. Chew and Y. M. Wang, "Reconstruction of two-dimensional permittivity distribution using the distorted Born iterative method," *IEEE Transactions on Medical Imaging*, vol. 9, no. 2, pp. 218-225, 1990.

[39] L. Li, W. Zhang and F. Li, "Tomographic reconstruction using the distorted Rytov iterative method with phaseless data," *IEEE Geoscience and Remote Sensing Letters*, vol. 5, no. 3, pp. 479-483, 2008.

[40] S. Fan, S. Smith-Dryden, G. Li and B. Saleh, "Reconstructing complex refractive-index of multiply-scattering media by use of iterative optical diffraction tomography," *Opt. Express,* vol. 28, pp. 6846-6858, 2020.

[41] H.-Y. Liu, D. Liu, H. Mansour, P. Boufounos, L. Waller and U. Kamilov, "SEAGLE: Sparisity-driven image reconstruction under multiple scattering," *IEEE Transactions on Computational Imaging,* vol. 4, no. 1, pp. 73-86, 2017.

[42] E. Soubies, T.-A. Pham and M. Unser, "Efficient inversion of multiple-scattering model for optical diffraction tomography," *Opt. Express,* vol. 25, no. 18, pp. 21786-21800, 2017.

[43] E. Mudry, P. Chaumet, K. Belkebir and A. Sentenac, "Electromagnetic wave imaging of three-dimensional targets using a hybrid iterative inversion method," *Inverse Problems,* vol. 28, no. 6, p. 065007, 2012.

[44] Y. Sung and R. R. Dasari, "Deterministic regularization of three-dimensional optical diffraction tomography," *Journal of the Optical Society of America a,* vol. 28, no. 8, pp. 1554-1561, 2011.

[45] K. Kawano and T. Kitoh, Introduction to Optical Waveguide Analysis: Solving Maxwell's Equations and the Schrödinger Equation, New York: John Wiley and Sons, Inc., 2001.

[46] D. C. Ghiglia and L. A. Romero, "Minimum Lp-norm two-dimensional phase unwrapping," *Journal of the Optical Society of America A,* vol. 13, no. 10, pp. 1999-2013, 1996.

[47] J. W. Goodman, Introduction to Fourier Optics, 3rd ed., Englewood: Roberts and Company Publishers, 2005.

[48] S. Fan, S. Smith-Dryden, G. Li and B. E. A. Saleh, "Optimization-based optical diffraction tomography using iODT initialization," *Journal of the Optical Society of America A,* vol. 38, no. 7, pp. 947-953, 2021.

[49] L. Tian, J. C. Petruccelli and G. Barbastathis, "Transport of intensity imaging with TV regularization and nonlinear diffusion denoising," *Imaging and Applied Optics Technical Papers, OSA Technical Digest,* 2012.

[50] S. J. LaRoque, E. Y. Sidky and X. Pan, "Accurate image reconstruction from few-view and limited-angle data in diffraction tomography," *J. Opt. Soc. Am. A. Opt. Image Sci. Vis.,* vol. 27, no. 7, pp. 1772-1782, 2010.

[51] A. Beck and M. Teboulle, "Fast Gradient-Based Algorithms for Constrained Total Variation Image Denoising and Deblurring Problems," *IEEE Transactions on Image Processing,* vol. 18, no. 11, pp. 2419-2434, 2009.

[52] K. Lee, K. Kim, G. Kim, S. Shin and Y. Park, "Time-multiplexed structured illumination using a DMD for optical diffraction tomography," *Opt. Lett.,* vol. 42, no. 5, pp. 999-1002, 2017.

[53] W. Krauze, A. Kus and M. Kujawinska, "Limited-angle hybrid optical diffraction tomography system with total-variation-minimization-based reconstruction," *Opt. Eng,* vol. 54, no. 5, 2015.

[54] A. Taflove and S. C. Hagness, Computational Electrodynamics: The Finite-Difference Time-Domain Method, Third Edition 3rd Ed., Artech House, 2005.

[55] D. C. Ghiglia and M. D. Pritt, Two-Dimensional Phase Unwrapping: Theory, Algorithms, and Software, Wiley, 1998.

[56] S. Smith-Dryden, S. Fan, G. Li and B. E. A. Saleh, "Time-gated optical diffraction tomography," in *Frontiers in Optics 2017*, Washington, D.C., 2017.

[57] J. Behal, "Quantitative phase imaging in common-path cross-referenced holographic microscopy using double-exposure method," *Scientific Reports*, vol. 9, no. 9801, 2019.

[58] G. G. Levin, G. N. Vishnyakov, V. L. Minaev, M. I. Latushko, V. V. Pickalov, V. K. Belyakov, E. P. Sukhenko and A. V. Demyanenko, "Shearing interference microscopy for tomography of living cells," in *Advanced Microscopy Techniques IV; and Neurophotonics II*, Munich, 2015.

[59] T. Tommasi and B. Bianco, "Frequency analysis of light diffraction between rotated planes," *Optics Letters*, vol. 17, no. 8, pp. 556-558, 1992.

[60] S. Zhang, D. Asoubar, C. Hellmann and F. Wyrowski, "Propagation of electromagnetic fields between non-parallel planes: a fully vectorial formulation and an efficient implementation," *Applied Optics*, vol. 55, no. 3, pp. 529-538, 2016.

[61] Z. Chen, X. Jin, L. Li and G. Wang, "A limited-angle CT reconstruction method based on anisotropic TV minimization," *Physics in Medicine and Biology*, vol. 58, no. 7, 2013.

[62] J. Frikel, "Sparse regularization in limited angle tomography," *Applied and Computational Harmonic Analysis,* vol. 34, no. 1, pp. 117-141, 2013.

[63] A. H. Delaney and Y. Bresler, "Globally convergent edge-preserving regularizaed reconstruction: an application to limited-angle tomography," *IEEE Transactions on Image Processing,* vol. 7, no. 2, pp. 204-221, 1998.

[64] L. Wang, P. P. Ho, C. Liu, G. Zhang and R. R. Alfano, "Ballistic 2-D Imaging Through Scattering Walls Using an Ultrafast Optical Kerr Gate," *Science,* vol. 253, no. 5021, pp. 769-771, 1991.

[65] A. Bassi, D. Brida, C. D'Andrea, G. Valentini, S. Silvestri and G. Cerullo, "Time-gated optical projection tomography," *Opt. Lett.,* vol. 35, no. 16, pp. 2732-2734, 2010.

[66] A. D. Yablon, "Multi-wavelength optical fiber refractive index profiling by spatially resolved Fourier transform spectroscopy," *Journal of Lightwave Technology,* vol. 28, no. 4, pp. 360-364, 2010.

[67] J. Jung, K. Kim, J. Yoon and Y. Park, "Hyperspectral optical diffraction tomography," *Opt. Express,* vol. 24, no. 3, pp. 2006-2012, 2016.